Review

Polyoxometalate-based porphyrinic metal-organic frameworks as heterogeneous catalysts

Arash Ebrahimi [b,*], Lukáš Krivosudský [c], Alexey Cherevan [a,*], Dominik Eder [a]

[a] Institute of Materials Chemistry, Technische Universität Wien, 1060 Vienna, Austria
[b] Department of Inorganic Chemistry, Faculty of Natural Sciences, Comenius University in Bratislava, Mlynská dolina, Ilkovičova 6, 842 15 Bratislava, Slovakia
[c] Comenius University in Bratislava, Faculty of Pharmacy, Department of Chemical Theory of Drugs, SK-83232, Slovakia

ARTICLE INFO

ABSTRACT

The ever-increasing appearance of inorganic–organic hybrid materials incorporating organic metalloporphyrins (MPs) and inorganic polyoxometalates (POMs) – separately, two groups of effective molecular catalysts – which combine to form the ground-breaking class of metal–organic frameworks (MOFs), has allowed this class to participate in numerous kinds of chemical reactions and mimic the activity of heterogeneous bio-, photo- and electrocatalysts. Recent results have shown that the integration of POMs and MPs in a porous structure not only maintains the characteristic functionalities of both components, but can also generate novel and unparalleled features including augmented stabilities, remarkable selectivity, improvable porosity, and novel and more favorable topologies. Furthermore, the immobilization of these component species (POMs and MPs) within a unified framework can prevent their catalytic deactivation, which mostly arises from suicidal self-oxidation of porphyrin moieties. It has also been established that the introduction of POMs – owing to their broad range of size, structure, and highly negative charge distribution throughout the cluster – can further expand their structural diversity and greatly influence the stability and catalytic performance of porous porphyrinic MOFs. What is more, the incorporation of POMs inside the pores or their use as secondary building units (SBUs) within the framework can give rise to an increase in their original reusability, perpetuity, and adsorption ability. Moreover, their incorporation can also boost the transfer of electrons (e.g., photoexcited charge carriers) through the network. Therefore, POM-based porphyrinic MOFs (porphyrinic POMMOFs) are materials that can

simultaneously take advantage of the combined uniqueness of the individual traits of POMs, porphyrins and MOFs, which display rich redox photochemistry, biomimetic ability, and porosity, respectively.

This review aims to represent the latest progress in porous porphyrinic POMMOFs, encompassing their categorization, fabrication and exploitation in the catalysis field. To the best of our knowledge, hitherto no specific attempt has been made to cover this topic, and our review would be the first systematic scrutiny of these porous materials. Last but not least, the POMs that have been templated to synthesize porphyrinic POMMOFs are still mostly limited to a few types of POMs. Moreover, the porphyrin linkers which were used to create such MOFs have also been confined to only a few kinds. Thus, we suggest that other POMs ((iso-) heteropolyoxometalates) and porphyrin-based linkers could be explored, with an eye to creating new state-of-the-art porphyrinic POM-MOFs. In the short term, it is anticipated that this review will encourage scientists to substantially extend the frontiers of knowledge about these systems, not only in the area of catalysis, but also in such versatile and underexplored domains as magnetism, gas sorption, sensing, biomedicine, and electrochemical and photo-catalytic utilizations. For these reasons, we strongly believe that this comprehensive review will not only provide a better overview of the subject, but also open up promising directions of research and stimulate scientific interest and enthusiastic curiosity. It will also pave the way to generating important new ideas for the future of the synthesis and applications of these invaluable types of MOFs.

1. Introduction

A superb and peerless group crystalline inorganic materials, poly-oxometalates (POMs) are a vast class of anionic metal oxide clusters, and are principally composed of the first-row d-block transition metal-oxido complexes (groups 5 and 6) at their highest oxidation states ($(+IV, +V,$ and $+ VI)$ (particularly $V^{IV,V}$, $Mo^{V,VI}$ and W^{VI}, less commonly Nb^V and Ta^V). These clusters' charge density distribution and suitable ratio of charge-to-ionic radius (i) lead to inhibition of unlimited polymerization, and (ii) enable the formation of π-bonds to the O^{2-} ligands. In addition, the formation of ordered and individual metal–oxygen polyhedra sharing corner- and edged- (infrequently faced-) coordination space extends their structures from tetragonal to pentagonal bipyramidal [1–5]. As a result, due to the great combination of vigorous metal-oxido bonding and coordination flexibility – which then leads to their capability for regulated polymerization – these systems also possess structural versatility with regards to partial replacement by other metal ions, creating several different kinds of POMs including Anderson, Lindqvist, Strandberg, Keggin, Preyssler, Waugh, Well-Dawson, Finke, Weakley

and Silverton (Scheme 1) [6–8]. POMs also display unrivaled chemical and physical exclusivities, and a stunning ability to generate large-scale structures ranging from the nano to the micro scale [9,10]. Generally speaking, POMs can simultaneously serve as Lewis acids and bases under a range of catalysis reaction conditions, in which high-valence unoc-cupied d-orbitals of metal centers easily grab electrons while the surface polyoxoanions' (POAs) numerous O ions donate electrons mildly [11]. Their strong capability to capture and liberate electrons, readily avail-able surface, versatile structures, solubility, and acidity, as well as their general redox flexibility, which is vital for catalytic applications, make them prominent catalysts for numerous hetero- and homogeneous organic/inorganic reactions [12,13].

Thanks to their highly flexible pore shape, extremely rigid frame-work, multiple topologies, diverse architectures and highly adjustable structure, metal–organic frameworks (MOFs) are a significant subclass of porous inorganic–organic compounds, and one whose numerous members are basically self-assembled from metal ions and/or metal oxo clusters connected through polydentate organic linkers/ligands. They have attracted significant interest owing to their potential utilization
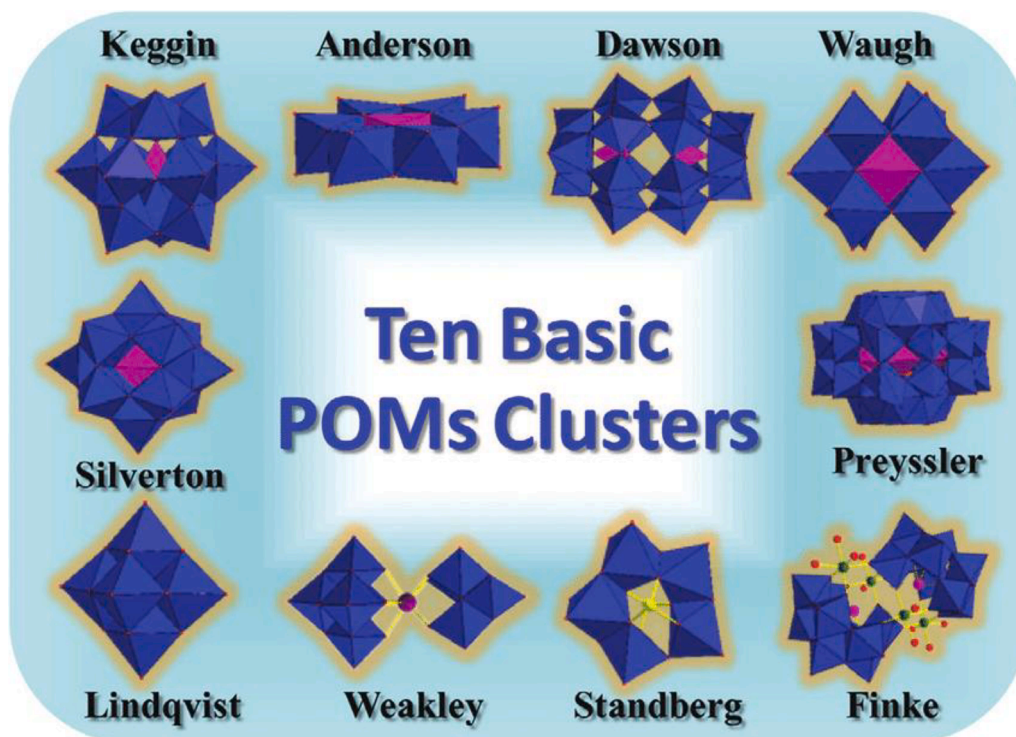
Scheme 1. Ten fundamental structural topologies of POMs. Reproduced with permission from Ref [4]. Copyright 2019 Elsevier.
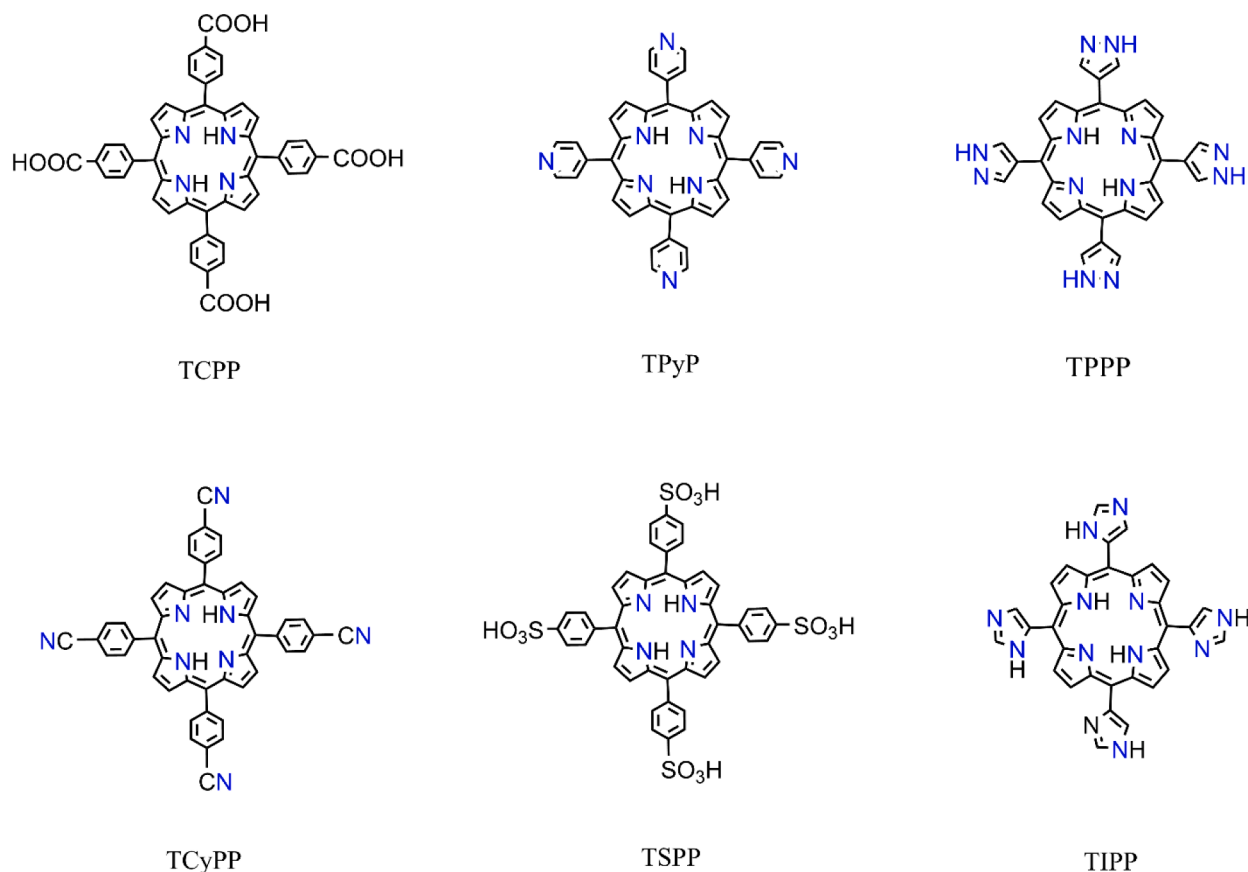
Scheme 2. The most commonly used porphyrin linkers for the porphyrinic MOFs synthesis. TCPP = 5,10,15,20-tetrakis(4-carboxyphenyl)porphyrin; TPyP = 5,10,15,20-tetrakis(4-pyridyl)porphyrin; TPPP = 5,10,15,20-tetrakis(4-(1H-pyrazol-4-yl)phenyl)porphyrin; TCyPP = 5,10,15,20-tetrakis(4-cyanophenyl)porphyrin; TSPP = 5,10,15,20-tetrakis(4-sulfonato-phenyl)porphyrin; TIPP = 5,10,15,20-tetrakis(4-(imidazol-1-yl)phenyl)porphyrin.

prospects in the areas of catalysis [14], gas storage/separation [15], (photo-) catalysis [16], drug delivery [17], biomedicine [18], and electrochemistry [19], among others.

The systematic construction of new MOFs intended for a particular purpose begins with the judicious selection of a specific linker with appropriate length and symmetry. Highly symmetrical aromatic linkers such as porphyrins, with a planar macrocycle core (D$_{4h}$ symmetry) as a basic synthon, may be utilized to form the important subclass of porphyrinic MOFs [20–23]. The most common and broadly used porphyrin-based linkers, which have produced a significant number of porphyrinic MOFs, are shown in Scheme 2.

Porphyrin exhibits certain desirable properties: a fairly robust geometry and great thermal durability, while having an architecturally rigid structure with peripherally pendant functionalities (α-, β-environs) that can be easily adjusted [24]. In addition to this, metallization at porphyrin center forms metalloporphyrin (MP) complexes which play important roles in nature for a variety of biological purposes, being found in hemoglobin, chlorophyll a, methylcobalamine (Vitamin B12), cofactor F340, and numerous enzyme families, including myoglobins, peroxidases and cytochromes [25,26]. Porphyrin thus has a reputation as a structure which can help facilitate a vast number of processes, so it is naturally interesting to study what it can do when employed as linker in an innovative group of functional materials (Scheme 3).

In this respect, using MPs in the preparation of MOFs has yielded important results in materials chemistry due to the mimicking function of MPs as catalytically active sites in manifold biological reactions [27–30]. Because of their distinctive planar π-aromatic system, they possess notable photophysical and electrochemical traits that can be tuned by circumferential functional groups and centrally-coordinated metal ions. These properties allow the use of MPs to form porous

frameworks and molecular cages of a favorable size for the desired applications [18,31].

The highly impressive subclass of porphyrinic MOFs has clearly shown that the inclusion of MPs in porous coordination frameworks allows for not only versatile functionalities, but also enhanced accessibility to various species and substrates while preserving the porosity of the building blocks. It furthermore stabilizes the porphyrin units and could also lead to new peripheral functionalities and novel features being connected to the porphyrins. Such properties therefore increase the potential for finding highly efficient heterogeneous catalysts for many organic transformation reactions [32–34].

In homogeneous catalysis, the main disadvantages of MPs and POMs as molecular catalysts are their small surface areas, made worse by their low solubility. However, a better solubility in polar solvents, combined with difficulties in separation and the reduced catalytic activity which arises from self-aggregation, would make them more or less unrecoverable from the other reaction components. To resolve these drawbacks, immobilization/incorporation of POMs and MPs into a rigid network such as eminent MOFs could be an important strategy to enable them to act as heterogeneous catalysts – a strategy that has appeared in the last few decades [35].

To address such a challenge, merging the POMs and MPs into porous MOFs could not only simultaneously enhance stability, avoid destructive oxidation of porphyrins, and improve the reusability, small surface areas and electron transfer of POMs, but also form a unified porous MOF network which shows great promise due to combining all of the previously-mentioned properties in one structure alone [36–40].

There are many examples of POM insertion helping to enhance the stability (thermal, chemical and structural) and heterogeneous catalytic activity of MOFs, as well as boosting the recoverability of POMs. To
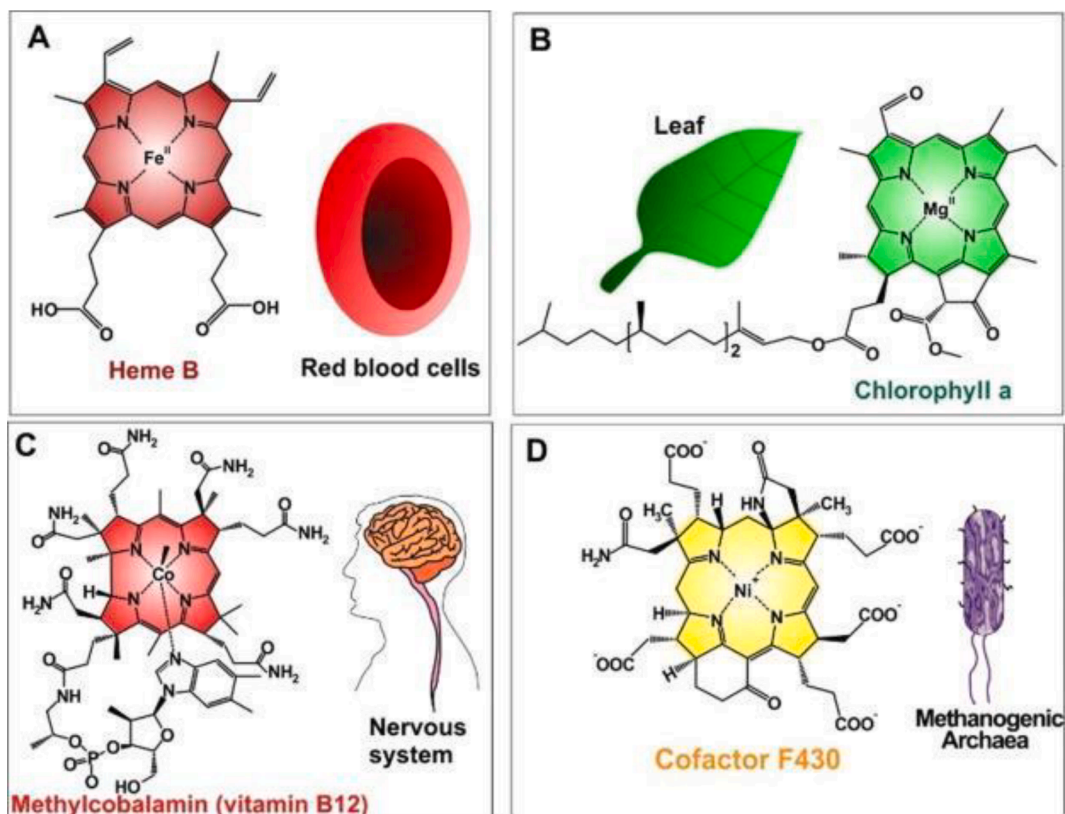
Scheme 3. Naturally well-known MPs. (a) iron(II)-porphyrin "Heme B in RBCs", an oxygen carrier; (b) magnesium(II)-porphyrin "chlorophyll a", required to provide energy to the plant by photosynthesis; (c) cobalt(II)-porphyrin "methylcobalamin (vitamin B12)", necessary for supporting the functioning of the nervous system; (d) nickel(II)-porphyrin "Cofactor F430", which catalyzes methanogenesis in methanogenic archaea). Reproduced with permission from Ref [25]. Copyright 2019 Elsevier.
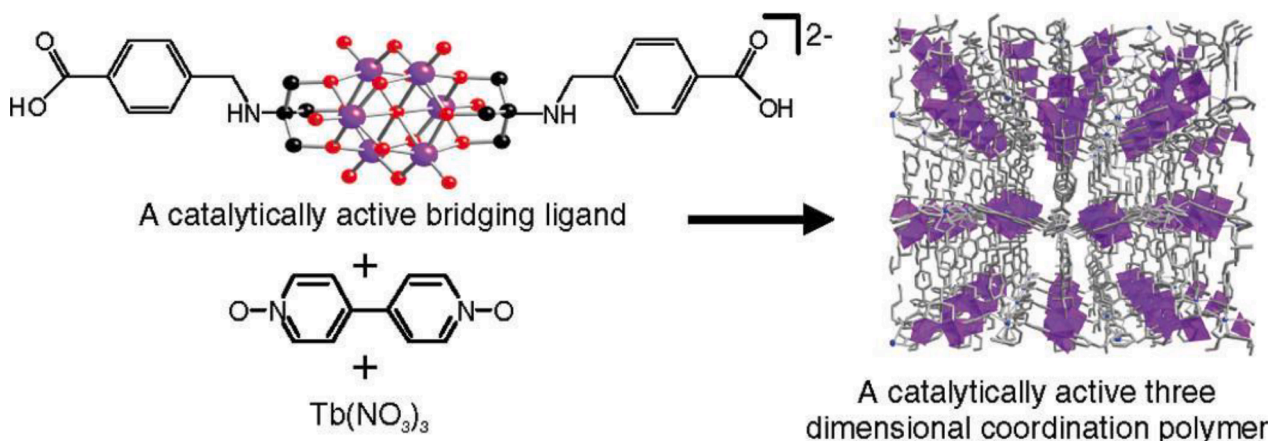
Scheme 4. Illustration of POMOF [Tb(bpdo)$_2$][V$_6$O$_{13}$(trn)$_2$]·1.5DMF·3.0EG synthesis process. Reproduced with permission from Ref [41]. Copyright 2007 American Chemical Society.

name a few, a 3D 2-fold interpenetrated POMOF was obtained by Hill *et al.* (2007) [41]. The as-formed POMOF [Tb(bpdo)$_2$][V$_6$O$_{13}$(trn)$_2$]· 1.5DMF·3.0EG was first isolated from the reaction of the Lindqvist-type POM [TBA]$_3$[H$_3$V$_{10}$O$_{28}$] with H$_4$trn (4-[[[2-Hydroxy-1,1-bis(hydrox-ymethyl)ethyl]amino]methyl] benzoic acid), which then subsequently reacted with Tb^{3+} and bpdo (4,4′-Bipyridine-N,N′-dioxide) ligand by a step-by-step strategy (Scheme 4). The fabricated POMOF was used as a heterogeneous oxidation catalyst to oxidize tetrahydrothiophene under O$_2$/air environment. Furthermore, the POMOF structure was stable under harsh constant turnover conditions.

POMOFs with improved thermal stability, electrocatalytic ability

and robust architectural resistance were created when another Lindqvist-type POM [TBA]$_2$[V$_6$O$_{13}$(tri)$_2$]·2CH$_3$CN (H$_3$tri, tris (hydroxymethyl)-4-picoline) was reacted with CuI or AgNO$_3$ to prepare the two systems [TBA]$_3$Cu[V$_6$O$_{13}$(tri)$_2$]$_2$·2DEF and [TBA]Ag [V$_6$O$_{13}$(tri)$_2$], respectively. More importantly, the illustration in Scheme 5 shows that the former POMOF crystallized as a 3D 6-fold inter-penetrated network with diamond topology, whilst the latter POMOF forms a non-interpenetrated 3D network with 1D hexagonal channels [42].

A new 3D two-fold interpenetrated POM@MOF, {[Ag$_2$(trz)$_2$] [Ag$_{24}$(trz)$_{18}$][PMo$_{12}$O$_{40}$]$_2$}, was manufactured by the reaction of
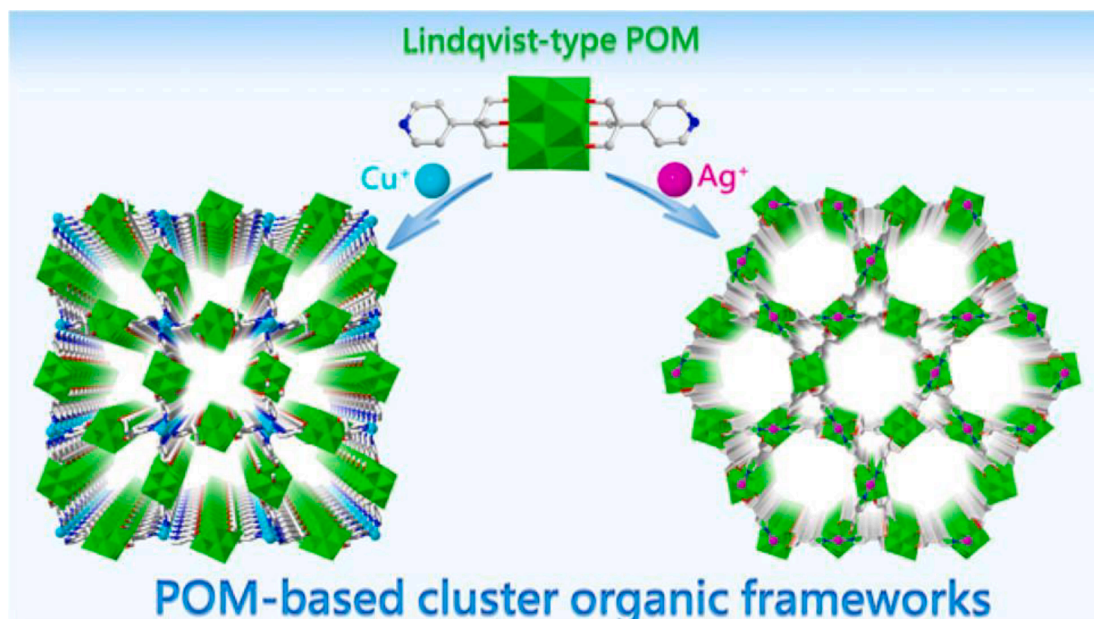
Scheme 5. The structures of two different POMOFs. Right [TBA]$_3$Cu[V$_6$O$_{13}$(tri)$_2$]$_2$·2DEF and left [TBA]Ag[V$_6$O$_{13}$(tri)$_2$]. Reproduced with permission from Ref [42]. Copyright 2018 American Chemical Society.
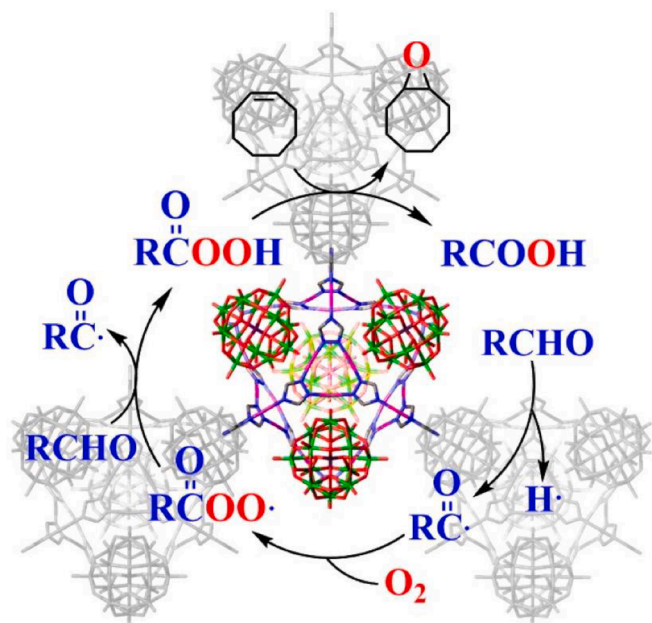
Scheme 6. The framework and proposed mechanism for epoxidation of olefines over POM@MOF, {[Ag$_2$(trz)$_2$][Ag$_{24}$(trz)$_{18}$][PMo$_{12}$O$_{40}$]$_2$}. Reproduced with permission from Ref [132]. Copyright 2019 MDPI.

CH$_3$COOAg and trz (1,2,4-Triazole) with H$_3$PMo$_{12}$O$_{40}$ under hydrothermal conditions (2019) [132]. It showed highly efficient catalytic activity and selectivity for the aerobic epoxidation of alkenes, as well as great structural durability, which was enhanced by various interactions involving π···π stacking, Ag-Ag and electrostatic interactions (Scheme 6).

Scheme 7 represents the reactions of tr$_2$ad (1,3-Bis(1,2,4-triazol-4-yl) adamantine), Cu(OAc)$_2$·H$_2$O and (NH$_4$)$_6$Mo$_7$O$_{24}$·4H$_2$O over a range of reactant concentrations and ratios, as carried out by Lysenko *et al* (2014). They obtained three-layered POM-based MOFs (POMMOFs), including the POM@MOFs ([Cu$_2^{II}$(tr$_2$ad)$_4$](Mo$_8$O$_{26}$) and the two POMOFs [Cu$_4^{II}$(μ$_4$-O)(tr$_2$ad)$_2$(MoO$_4$)$_3$]·7·.5H$_2$O, and [Cu$_2^I$(tr$_2$ad)$_2$]

(Mo$_2$O$_7$)·H$_2$O [43]. The POMMOFs manifested substantial chemical/ thermal stability, and showed a remarkable ability to catalyze the oxidation of benzyl alcohol and epoxidized *cis*-cyclooctene as heterogeneous catalysts.

In this account, we summarize information on the state-of-the-art fabrication approaches and provide a comprehensive picture of multifunctional POM-based porphyrinic MOFs (porphyrinic POMMOFs) and their applications in the field of heterogeneous catalysis. Our broad survey of porphyrinic POMMOFs indicates that, similarly to the majority of coordination compounds and porous architectures, the conformation and topology of the porous framework depend strongly on the nature and arrangement of the connections between the porphyrin fragments and the other components of the MOF. From the catalytic point of view, the consolidation of MPs and secondary functional sites/POMs promotes both the catalytic capability and stability of the porous porphyrinic frameworks when compared with their homogeneous counterparts. On the other side of the coin, the potent acidity, distinctive electron redox and physical traits and photoactivity of POMs, together with the tunable pore size and high surface areas of MOFs, result in their combinations being remarkable heterogeneous catalysts able to catalyze multiple organic reactions. Accordingly, in this work we attempt to provide an overview of research into the synthetic procedures that were developed for porphyrinic POMMOFs in order to employ them as valuable heterogeneous catalysts. For the first time, we have thus attempted to examine the recent development of synthetic strategies for, and exceptional practical catalytic abilities of, porphyrinic POMMOFs, with POMs either encapsulated inside the porphyrinic MOF pores, or consolidated as secondary building units (SBUs) into the porphyrinic MOF architecture.

2. Classification and fabrication procedures of POMMOFs

2.1. Main categories of POMMOFs

There are four basic types of POMMOFs materials, where the first three taxonomies are single-crystals (I = a + b + c;) and the last one is POM-loaded MOF materials (II) (see Scheme 8). The first class (I; single-crystals) of these materials includes the sub-classes (a) direct attachment of POM units to d/f-block metal ions which are coordinated to multidentate organic linkers – here the POM acts as a secondary building unit
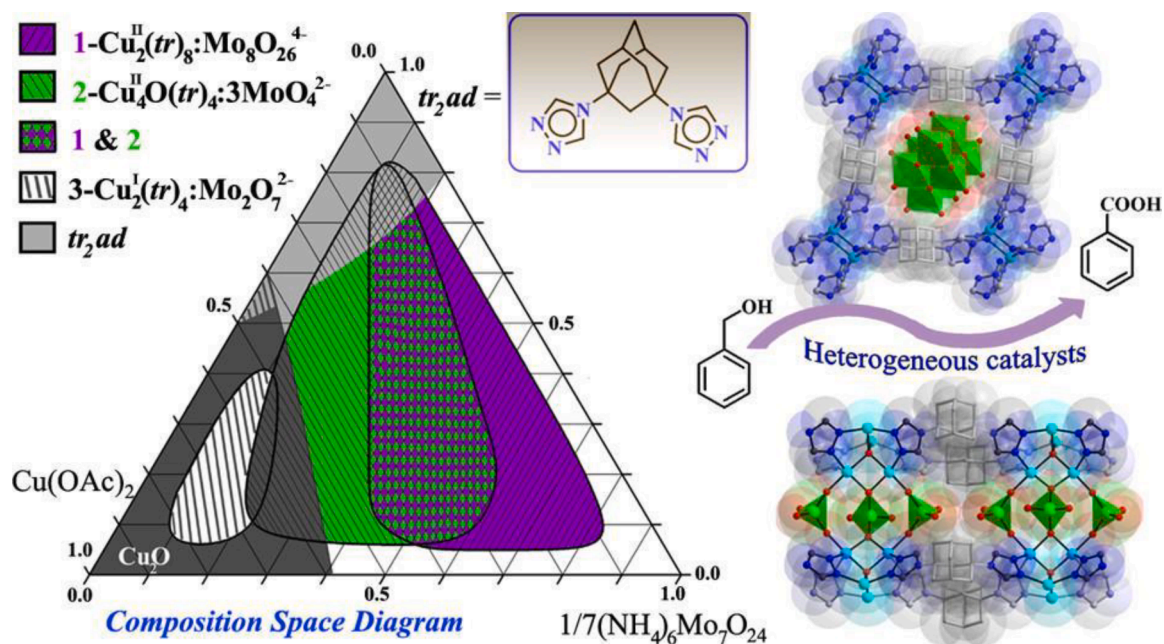
Scheme 7. The reaction conditions (left) and the structural framework of and heterogeneous reaction catalyzed by POM@MOF $[Cu_2^{II}(tr_2ad)_4](Mo_8O_{26})$ (top right), and the two POMOFs $[Cu_4^{II}(\mu_4\text{-}O)(tr_2ad)_2(MoO_4)_3]\cdot7\cdot.5H_2O$ and $[Cu_2^{I}(tr_2ad)_2](Mo_2O_7)\cdot H_2O$ (bottom right). Reproduced with permission from Ref [43]. Copyright 2014 American Chemical Society.
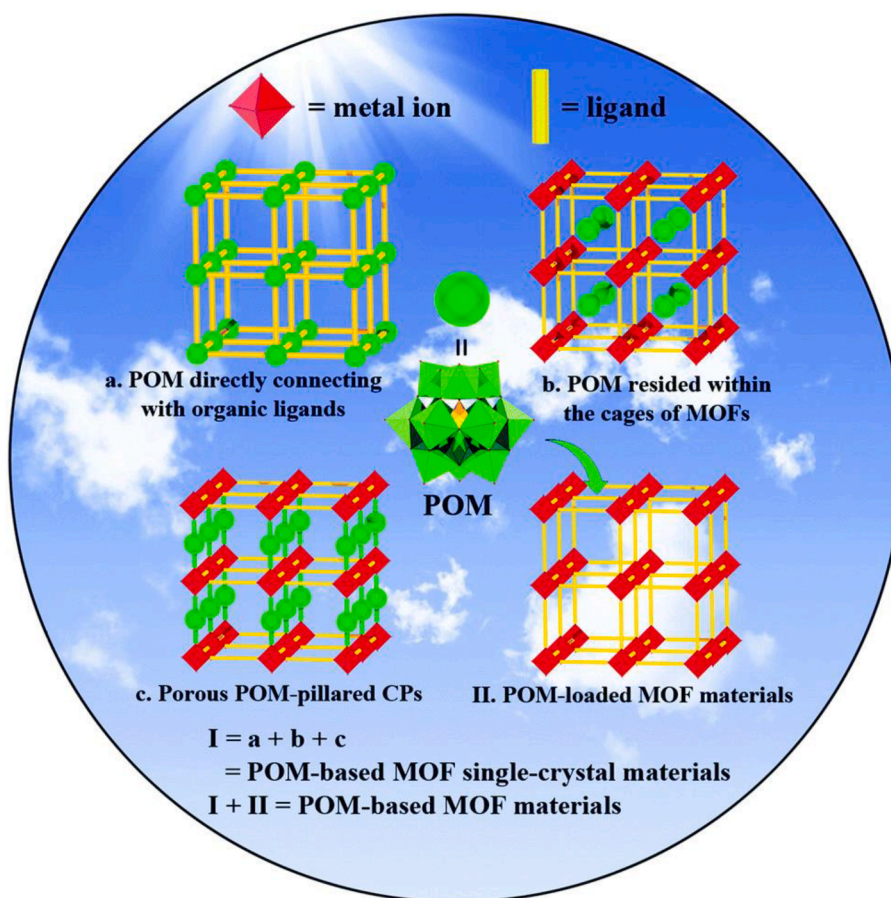
Scheme 8. Schematic illustration of four types of POMMOF materials. I (a + b + c) = POMMOF single-crystal materials, and II = POM-loaded materials; I + II = POMMOF materials. Reproduced with permission from Ref [10]. Copyright 2021 Royal Society of Chemistry.
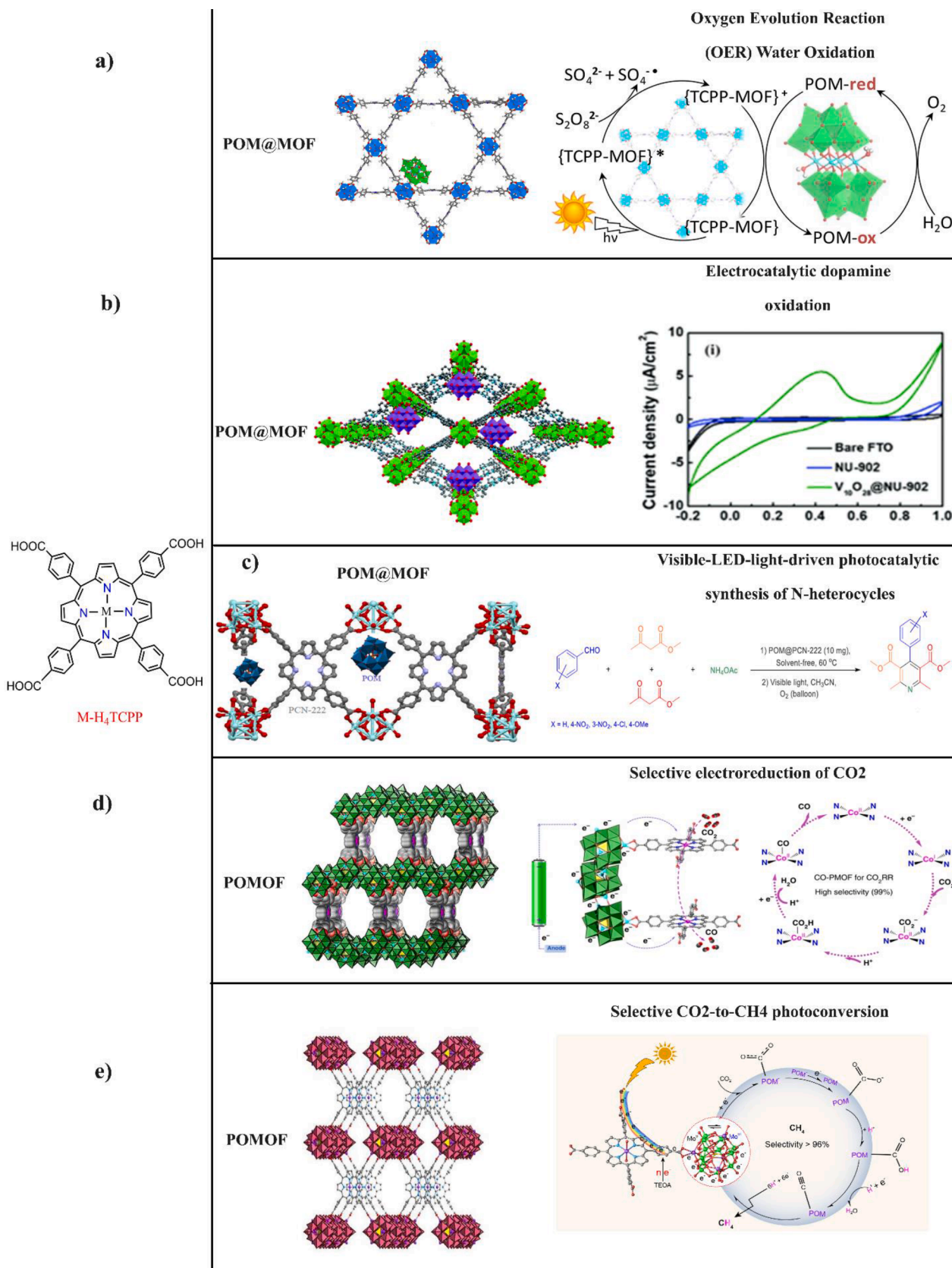
Scheme 9. The M−H₄TCPP linker utilized for the synthesis of porphyrinic POMMOFs, together with the various catalytic utilizations for such MOFs. (a) POM@MOF used for OER, (b) POM@MOF employed for electrocatalytic oxidation of DA, (c) POM@MOF exploited for photocatalytic production of N-heterocycles (pyridine-isolated organic compounds), (d) POMOF used for electrochemical reduction of CO_2, and (d) POMOF used for photocatalytic conversion of CO_2 to CH_4. Reproduced with permission from Refs [150,170,194,202,209]. Copyright 2019, 2020, 2022, 2018 and 2020, American Chemical Society, Royal Society of chemistry, Elsevier, Springer Nature and Oxford Academic, respectively. M−H₄TCPP = metal-5,10,15,20-tetrakis(4-carboxyphenyl)porphyrin.
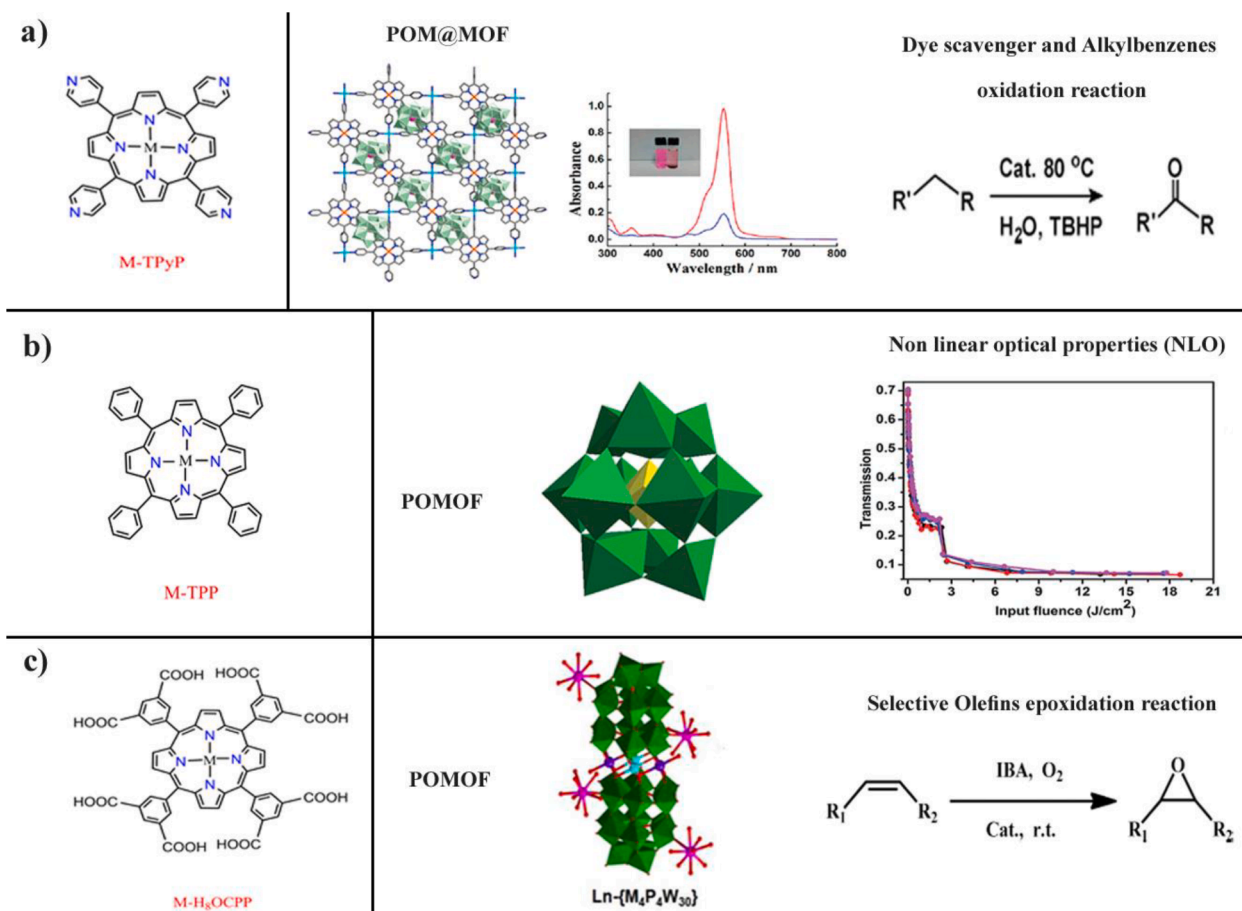
Scheme 10. The other three frequent MP ligands (M−TPyP, M−TPP and M−H$_8$OCPP) used for the fabrication of porphyrinic POMMOFs, together with notable catalytic utilizations of the resulting MOFs. (a) a POM@MOF utilized for dye capture and alkylbenzene oxidation catalyst, (b) a POMOF used for NLO properties, and (c) a POMOF used as an olefine epoxidation catalyst. Reproduced with permission from Refs [124,138,179]. Copyright 2012, 2014 and 2016, American Chemical Society, Royal Society of Chemistry and American Chemical Society, respectively. M−TPyP = metal-5,10,15,20-tetrakis(4-pyridyl)porphyrin; M−TPP = metal-5,10,15,20-tetrakis(phenyl)porphyrin; M−H$_8$OCPP = metal-5,10,15,20-tetrakis(3,5-biscarboxylphenyl)porphyrin.

(SBU) in the MOF; (b) encapsulation of anionic or modified POMs in the MOF voids (pores), driven by electrostatic forces, hydrogen bonds and/ or chemical bonding – here the POM can be used to modify and improve the framework and its properties; (c) porous pillared inorganic–organic POM-based materials – here both metal ions and POM species act as SBUs. The second group, POM-loaded MOF materials (II), are fabricated by the post-synthetic modification (PSM) method – in this case the POMs can be seen as an extra-framework adsorbate. They can be obtained by three processes: (i) MOF synthesis in the presence of POM, (ii) POM synthesis inside MOF cages, and (iii) MOF impregnation in POM solution. These two groups (I + II) together constitute the POMMOF class of materials. From the perspective of this review, categories a and b from group (I) (depending on their crystal structures) and the non-crystalline frameworks of group (II) are the most important types of porphyrinic POMMOFs synthesized so far. Frameworks in which POMs are either (1) a part of the structure, directly linked to the organic ligands (often denoted as porphyrinic POMOFs), or (2) confined inside the MOF pores (often denoted as porphyrinic POM@MOFs), can both be generally classified as POMMOFs [10,44].

2.2. Synthetic methods of POMMOFs

From the synthetic point of view, the POMMOF materials which have substantially proved their catalytically active capability in several reactions [45–49], are frequently obtained via encapsulation, *in situ* hydro-/solvothermal, mechanochemical, grafting, coprecipitation, PSM, dispersion, impregnation and so on [50–55]. Synthetic conditions and post-synthetic environments exert a significant influence on the target compounds with respect to their crystallinity, structures, deficiencies, dimensions, and acidity, as well as the position of the POM in these hybrid frameworks [56–60].

It should be stated that by far the most applicable route, the conventional hydro-/solvothermal method, is an efficacious way to prepare POMMOFs. Elevated temperature and pressure increase the solubility of the main reaction components (a POM and a MP) [10,37,38,61–63]. In addition, the increased ionization and diminished solvent viscosity under such reaction conditions allow better dissolution and facilitate the diffusion of organic components specifically [64]. Furthermore, according to the results published to date, pure POMs crystallize from and dissolve in aqueous solution readily [2,36]. Conversely, obtaining and dissolving organic ligands and crystalline POM-hybrid structures in aqueous media is more complicated due to their poor solubilities. Accordingly, the hydro-/solvo-thermal procedure has become the dominant method by which the majority of the reported crystalline POMMOFs have been prepared [65–72]. In contrast, for other methods, such as self-assembly or "one-pot" strategies (also known as conventional aqueous solution), reaction conditions such as pH, temperature, ratios, solvent, and particularly POM type can adversely affect the final product [44,73,74].

Generally, mixing POMMOF constituents – metal ions, POM and organic spacers *in situ* or postsynthetically – will unavoidably result in competing processes involving the various components, commonly

Table 1
Summarized information on the synthesis of porphyrinic POMMOFs and their utilizations.

	MOF	Porphyrin	POM	Synthetic Procedure	Application	Refs
Porphyrinic POMOFs	$[H_2TPP]_{1.5}[SW_{11}VO_{40}].5CH_3CN \cdot 4H_2O$; $[H_2TPP]_2[SW_{10}V_2O_{40}].4CH_3CN \cdot 3H_2O$; and $[H_2TPP][SW_{12}O40] \cdot 4H_2O$	TPP	$[SW_{12-n}V_nO_{40}]^{(2+n)-}$	*In situ**	NLO traits	[124]
	$[\{Gd_4Co_2(Co_4P_4W_{30})_2\}(Mn\text{-}OCPP)]$	Mn-H$_8$OCPP	$\{Gd_4M_6P_4W_{30}\}(M = Mn$ and $Co)$	*In situ*	O_2 activation	[138]
	$[PMo_8^VMo_{14}^{VI}O_{35}(OH)_5Zn_4]_2[MTCPP][2H_2O][1.5TBAOH]$ (M = Fe, Co, Ni, Zn)	M−TCPP	Zn-ε-Keggin	*In situ*	Electrochemical CO$_2$RR	[150]
	$([PMo_8^VMo_4^{VI}O_{35}(OH)_5Zn_4]_2[Fe^{III}\text{-}TCPP\text{-}Cl] \cdot Guest$; and $[PMo_8^VMo_4^{VI}O_{35}(OH)_5Zn_4]_2[M^{II}\text{-}TCPP][H_2O] \cdot Guest$; M = Zn, Ni, Cu, Co, and Mn)	M−TCPP	Zn-ε-Keggin	*In situ*	CO$_2$ PCR and ECR	[156]
	TM-POMOFs (TM = Fe, Co, Ni, Cu, Zn, Ru, Rh, Pd, Os, Ir, Pt)	M−TAPP	$[Mo_6]^{2e/2H}$	Simulation	DFT-derived calculation of ectrochemical CO$_2$ reduction	[169]
	NNU-13 and NNU-14	Zn-TCPP	Zn-ε-Keggin	*In situ*	Photoreduction of CO$_2$	[170]
	$\{[Cd\text{-}(DMF)_2Mn^{III}(DMF)_2TPyP](PW_{12}O_{40})\} \cdot 2DMF \cdot 5H_2O$	TPyP	$H_3PW_{12}O_{40}$	Step-by-step**	Dye capture and alkylbenzenes oxidation	[179]
Porphyrinic POM@MOFs	$P_2W_{18}Co_4@MOF\text{-}545$	TCPP	$P_2W_{18}Co_4$	Impregnation	Water oxidation	[193]
	$P_2W_{18}Co_4@MOF\text{-}545@ITO$	TCPP	$P_2W_{18}Co_4$	Impregnation and deposition	OER	[194]
	$V_{10}O_{28}@NU\text{-}902$	TCPP	$Na_6V_{10}O_{28}$	Impregnation	Dopamine oxidation	[202]
	$H_3PW_{12}O_{40}@PCN\text{-}222$	TCPP	$H_3PW_{12}O_{40}$	Impregnation	N-heterocycle derivatives formation	[209]
	H-POM@PCN-222(M) (M = Co, Fe, Mn, Ni)	TCPP	$Co^{III}Co^{II}(H_2O)W_{11}O_{39}$	PSM	Electrochemical CO$_2$RR	[155]

* In this context *in situ* means the self-assembly of POM precursors or metal ion salts with organic linkers upon hydro-/solvo-thermal conditions, also denoted as the "one-pot" method.

** Step-by-step indicates the preparation of pre-synthesized metal/ligand-modified-POMs to further interconnect with MOF linkers to form POMMOFs.

TPyP = 5,10,15,20-tetrakis(4-pyridyl)porphyrin; TCPP = 5,10,15,20-tetrakis(4-carboxyphenyl)porphyrin; TPP = 5,10,15,20-tetrakis(phenyl)porphyrin; Mn-H$_8$OCPP = Mn-5,10,15,20-tetrakis(3,5-biscarboxylphenyl)porphyrin; TAPP = 5,10,15,20-tetrakis(4-aminophenyl)porphyrin; OER = oxygen evolution reaction; PSM = post-synthetic method; NLO = nonlinear optical; CO$_2$RR = CO$_2$ reduction reaction; PCR = photocatalytic reduction; ECR = electrocatalytic reduction.
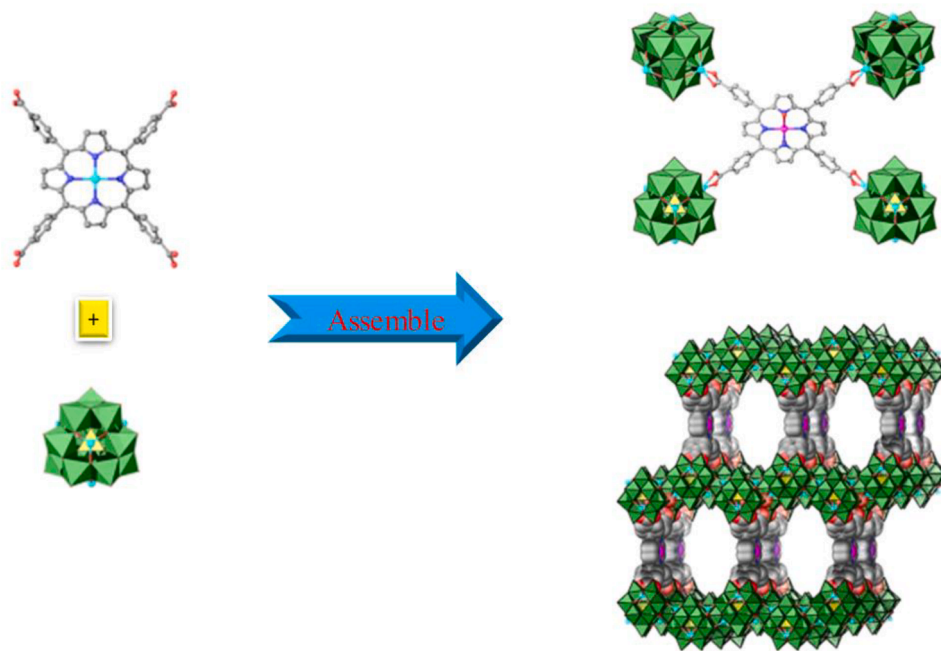
Scheme 11. Overall illustration of synthetic procedure of porphyrinic POMOFs being formed through primary approach (metal-attached POMs bound to MOF linkers). Reproduced with permission from Ref [150]. Copyright 2018 Springer Nature.

yielding the pure POM or MOF itself [75–77]. In contrast to the abundant accounts of POMs or MOFs, the reports of crystalline POMMOFs are exceptionally limited in both number and variety [78–80]. Furthermore, the preparation of nanocrystals of POMMOF is very arduous, and announcements of nano-scale POMMOF compounds have been very infrequent [81–85]. However, nanosized MOFs could potentially open

up new possibilities and areas of application. This would possibly encourage researchers to manufacture more nano-POMMOF networks, giving rise to the design and fabrication of notable POMMOF nano-compounds with various dimensions and configurations tailored for use in miscellaneous heterogenous catalysis.

The POM templates used in construction of these MOF materials are
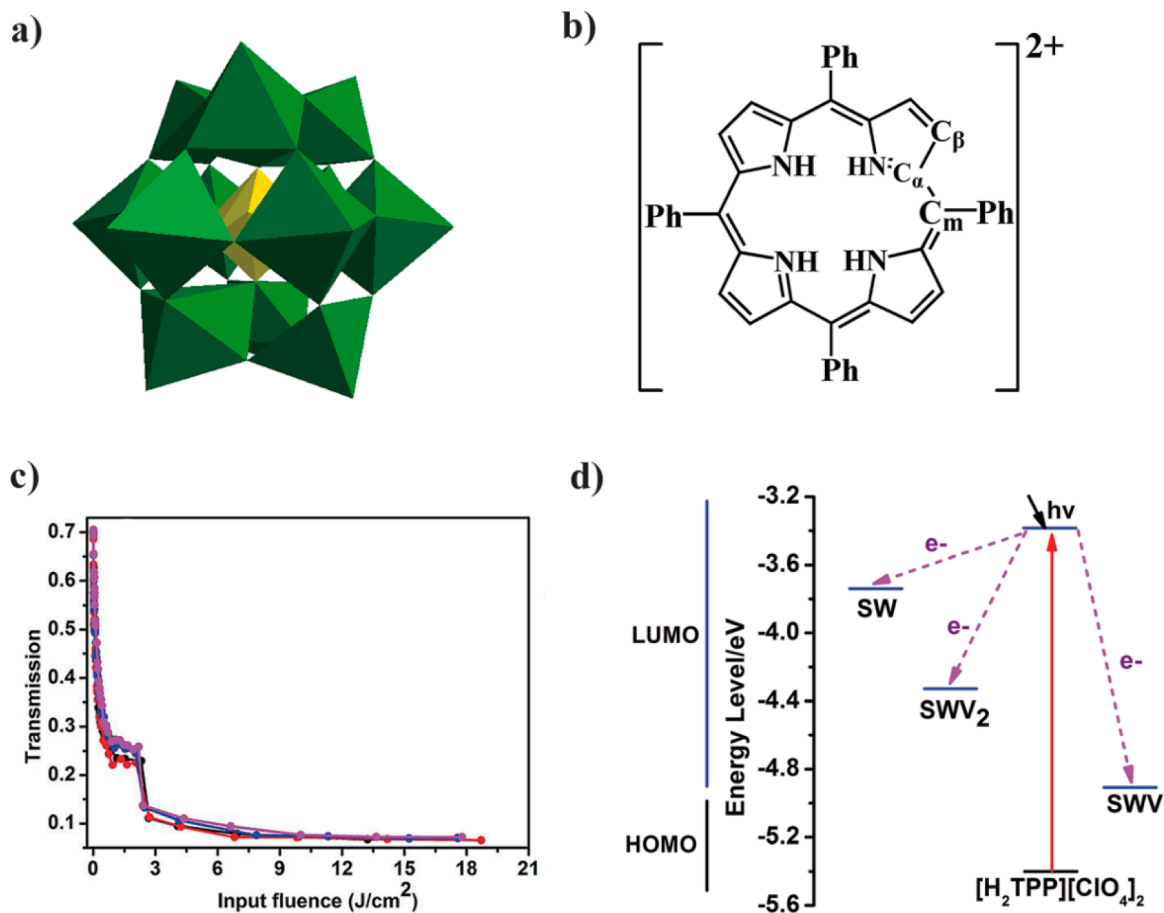
Fig. 1. (a) the polyhedral view of POM $[SW_{12-n}V_nO_{40}]^{(2+n)-}$ substituted by vanadium, (W/VO_6 octahedra, green; SO_4 tetrahedron, yellow) (b) porphyrin cation $[H_2TPP]^{2+}$, (c) measurements of the NLO transitions of the three compounds, black (1), red (2) blue (3) and pink ($[H_2TPP][ClO_4]_2$) in DMF at λ = 532 nm, and (d) diagram of the charge-transfer process of $[H_2TPP][ClO_4]_2$. LUMO levels are given in blue and the HOMO level in black. Reproduced with permission from Ref [124]. Copyright 2014 Royal Society of Chemistry. (For interpretation of the references to color in this figure legend, the reader is referred to the web version of this article.)
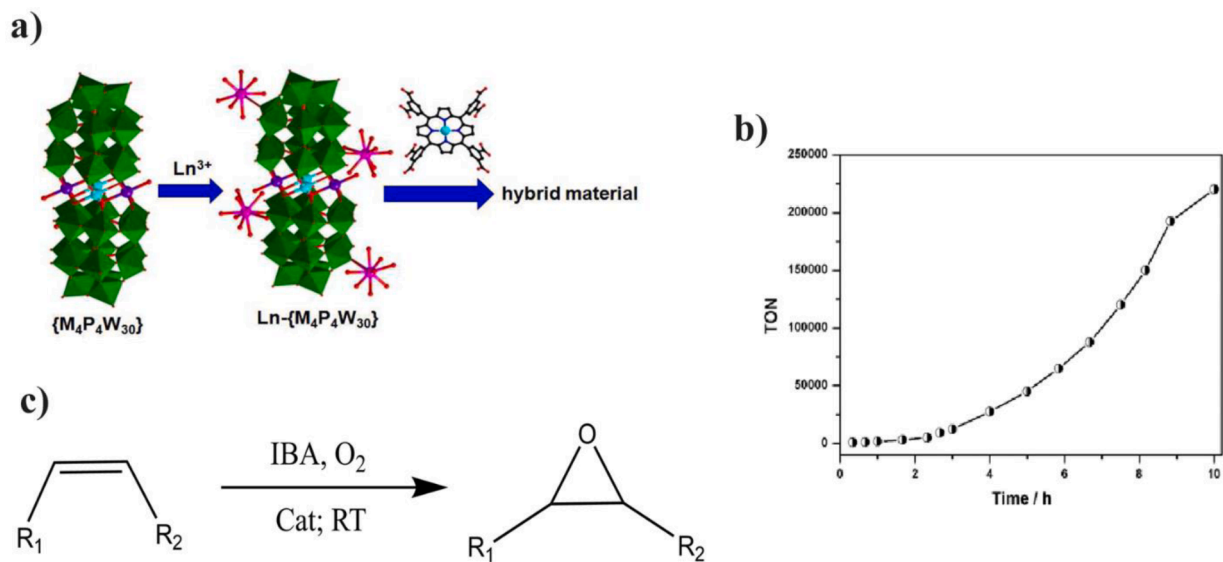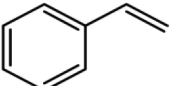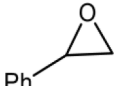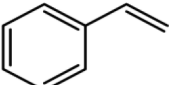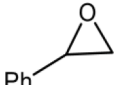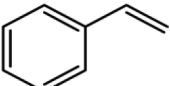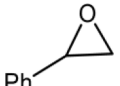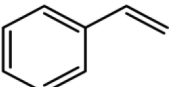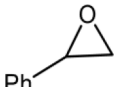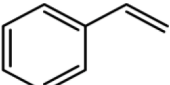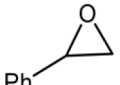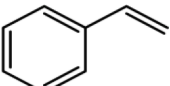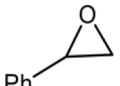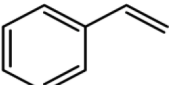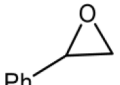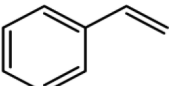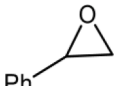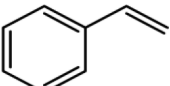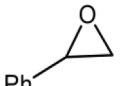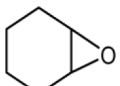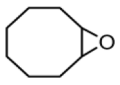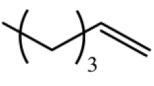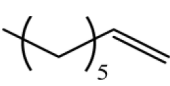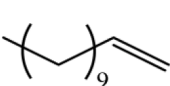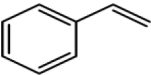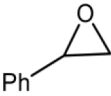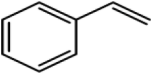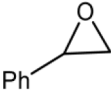
Fig. 2. (a) Schematic representation of the two-step procedure of porphyrinic POMOF fabrication, (b) TON plot of styrene epoxidation versus reaction time and (c) the olefin epoxidation reaction catalyzed by metalloporphyrin-POM material; IBA = isobutyraldehyde. Reproduced with permission from Ref [138]. Copyright 2016 American Chemical Society.

Table 2

Selective Olefin epoxidation performed over an as-synthesized POMOF and its precursors [138][a].

Entry	Substrate	Product	Catalyst	Conversion (%)[b]	Selectivity (%)[c]
1			**4**	**>99**	**94**
2			Mn-H$_8$OCPP	5	84
3			Co$_4$P$_4$W$_{30}$	59	94
4			Gd$_4$Co$_6$P$_4$W$_{30}$	63	92
5			Co$_4$P$_4$W$_{30}$/ Mn-H$_8$OCPP	49	86
6			Mn-Me$_8$OCPP	94	73
7			MnCo-1	8	72
8			MnMn-1	13	61
9			CoCo-1	94	62
10			4	85	>99
11			4	95	93
12			4	90	>99
13			4	44	>99
14			4	35	>99
15			4	26	>99

Table 2 (*continued*)

Entry	Substrate	Product	Catalyst	Conversion (%)[b]	Selectivity (%)[c]
16		Ph—epoxide	4	97	92[d]
17		Ph—epoxide	–	5	67
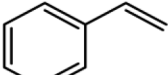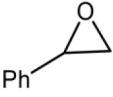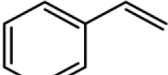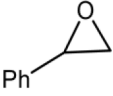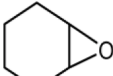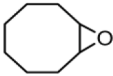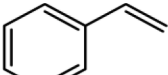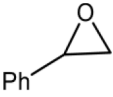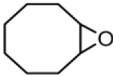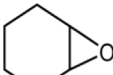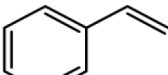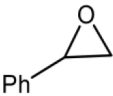
[a] Catalyst 1 (0.0002 mmol, based on the metalloporphyrin unit), substrate (0.1 mmol), and IBA (0.4 mmol) in 1 mL of CH_2Cl_2 were mixed over an O_2 atmosphere at RT for 2 h.

[b] Conversion % and [c] selectivity % were specified by GC–MS on a SE-54 column.

[d] The sixth catalytic cycle.

Table 3

Comparison of selective olefin epoxidation performed by formerly-described POMMOFs.

Entry	Substrate	Product	Catalyst	Conversion (%)	Selectivity (%)	Refs
1		Ph—epoxide	4	>99	94	[138]
2		Ph—epoxide	CoPMA@UiO-bpy	80	59	[142]
3		epoxide	PW12/MIL-101	67	83	[143]
4		epoxide	NENU-MV-1a	95	86	[144]
5		epoxide	PMo$_{11}$Co@UiO-66	68	>99	[145]
6		Ph—epoxide	[{Cu(en)$_2$}$_3${TeW$_6$O$_{24}$}]	90	60	[146]
7		epoxide	[Cu$_4^I$(3atrz)$_4$][PMo$_{10}^{VI}$Mo^{V}O$_{40}$]	82	>99	[147]
8		epoxide	{[Ag$_2$(trz)$_2$] [Ag$_{24}$(trz)$_{18}$]}[PMo$_{12}$O$_{40}$]$_2$	96	84	[148]
9		Ph—epoxide	{[PMo$_9$V$_5$O$_{42}$][Cu$_2$(2,2'-bpy)$_2$(C$_2$O$_4$)]}[Cu(2,2'-bpy)$_2$(H$_2$O)](Cu(2,2'-bpy)$_2$(Cl)]·3H$_2$O	98	79.1	[149]

predominately Keggin, Anderson and decavanadate anions (especially for porphyrinic POMMOFs), although other hetero- or iso-polyoxometalate clusters have sporadically been employed [10,57,86,87–90].

The most common MP ligands which have been used to obtain porous porphyrinic POMMOFs were predominately M−H$_4$TCPP, M−TPyP, M−TPP and M−H$_8$OCPP. These are shown together with various heterogenous catalytic applications reported for them in Scheme 9 and 10. Similarly, to other porphyrinic MOFs, the framework structure depends heavily on reaction media, the porphyrin's peripheral functionalities, metal nodes and so on [91].

Other parameters, such as the size match between POM anions and MOF pores, should also be considered. In consequence, designing and synthesizing novel MOFs in which suitable POM units and organic linkers combine to form well-size-matched MOFs is of course a very challenging task [37,44,54,92–94]. The manufacture of POMMOFs still requires very demanding work in terms of fabrication chemistry.

As a result of all of this, POMMOFs that can be prepared using multiple methods often display a dependence of catalytic exclusivities and activity on the method of preparation [95–99]. We hold that the future of MOF technology will involve a lot more investigation into the synthesis of POMMOFs and their catalytic utilizations.
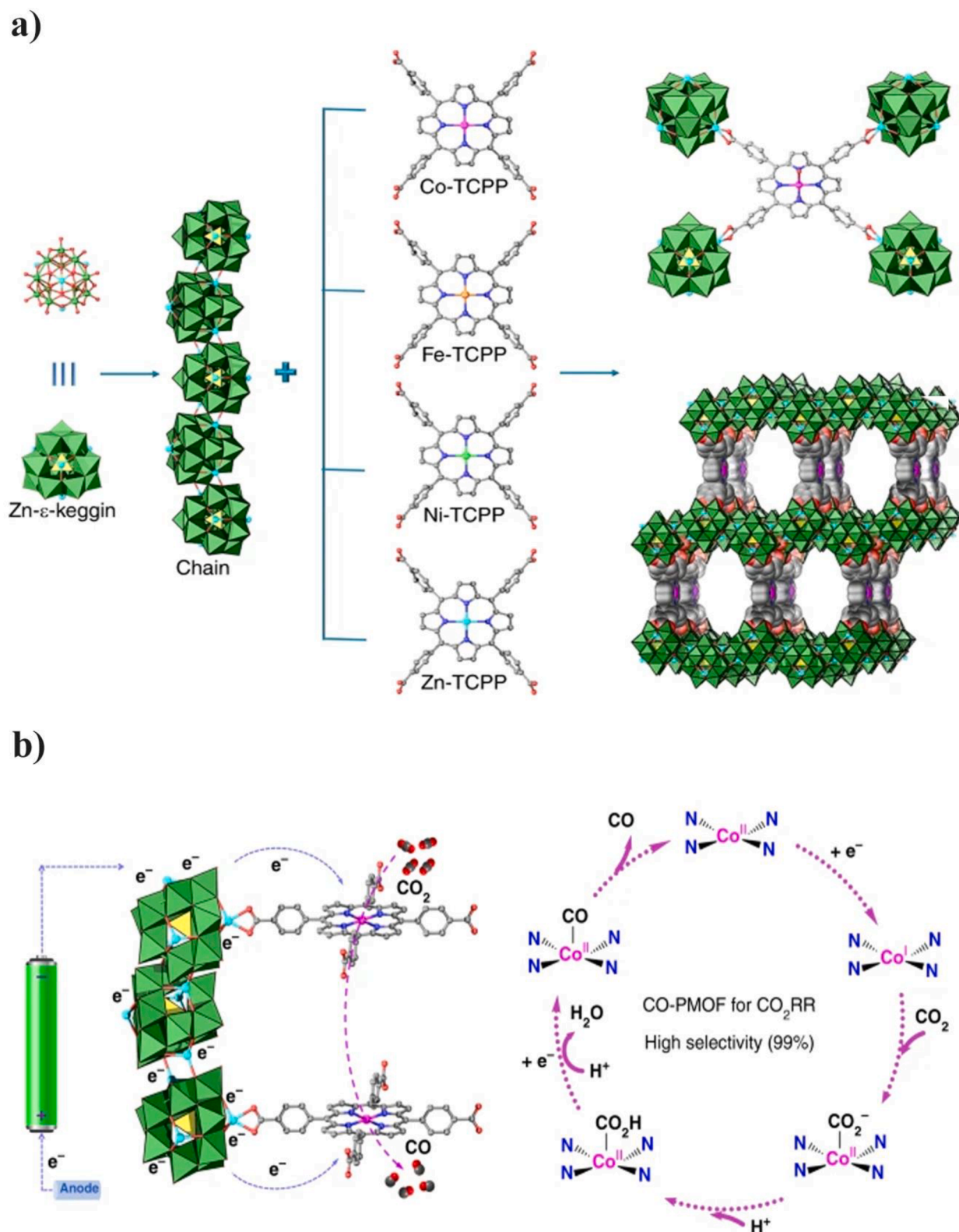
Fig. 3. (a) Three-dimensional illustration of M−POMOFs formed by zigzag-shaped POM strings linked to the M−TCPP linkers and (b) schematic sketch of suggested mechanism of CO₂ reduction on the best-performing electrocatalyst, Co-POMOF. Reproduced with permission from Ref [150]. Copyright 2018 Springer Nature.
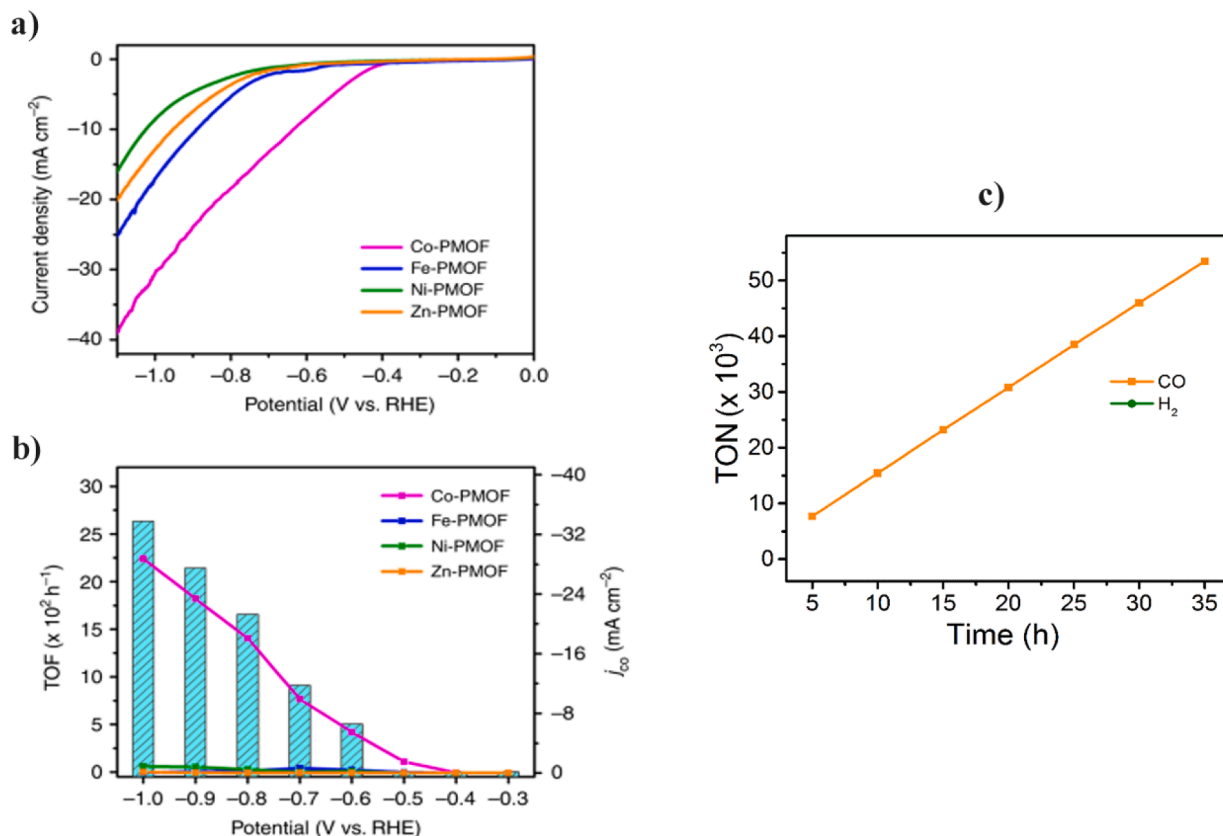
Fig. 4. (a) LSV diagram, and (b) plots of partial current density of CO and relative TOFs of a variety of POMOFs used in electrocatalytic reduction of CO_2. (c) CO TON diagram of Co-POMOF versus time. Reproduced with permission from Ref [150]. Copyright 2018 Springer Nature.

3. Porphyrinic POMMOFs

3.1. Catalytic sufficiency and advantages of porhyrinic POMMOFs

3.1.1. Catalytic performances of porphyrinic POMMOFs

With regards to the catalytic activities of the porphyrinic POMMOFs, these kinds of MOF materials have recently captured growing attention in view of their inherent exploitations in numerous organic reactions [6,100–105]. As fundamental features, they incorporate distinct single-crystal frameworks, impressive surface areas, well-ordered and adjustable pores, a great density of catalytically active sites [106–109]. In addition, the strong Lewis acidity and reciprocal redox transmission properties of the POM segments in porphyrinic POMMOFs have made them promising catalysts in electron transfer reactions, which are used in multiple organic transformations and acid/base and oxidation catalysis [10,45,110–115].

As a newly-emerged class of crystalline porous inorganic–organic materials, porphyrinic POMMOFs have proven to be useful and effective substances in a variety of fields of application, including catalysis [116], light harvesting [117], gas sorption/separation [15], and electrochemical [19] and biomimetic [118] or biomedical applications [18]. Furthermore, the integration of artificially-fabricated variants on natural heme units (porphyrin metal complexes) into the framework leads to formation of porous POMMOFs which are both highly stable and extremely active as regards heterogeneous catalysis, with fascinating shape- and/or size-selective traits [19,32,119].

Heretofore, the preparation of stable porphyrinic POMMOF materials with appropriate cavity sizes has expanded the future possibilities of POMMOFs as heterogenous catalysts. Furthermore, diverse POMs and MPs (or other porphyrinic MOFs) with varied properties can be employed to prepare variable porphyrinic POMMOFs. Upcoming POMMOFs are being developed not only for a variety of applications in

heterogeneous organic catalysis [44], but also for other areas of application, like magnetism [120], drug delivery [121], gas storage/separation [122], proton conduction [123], etc., in which they are expected to become useful in the near future.

3.1.2. Advantages of porphyrinic POMMOFs

Up to now, a few examples of both types of porphyrinic POMMOFs (porphyrinic POM@MOFs and porphyrinic POMOFs) have been discussed. However, heterogeneous porphyrinic POMMOFs catalysts have many advantages: (i) the tunable hydrophobic-hydrophilic pores of MOFs and their increased high surface areas encourage the diffusion of the reactants and products, and permit the substrates to expose catalytically-active sites to the reactants effectively; (ii) appropriate cavity configuration and pore shape and size facilitate the dissemination of POM in order to obtain POMMOFs crystals with high quality and large sizes; (iii) the structure-directing property of POMs means using them as building blocks or deploying them as guest molecules to load the voids can result in formation of highly rigid and durable MOFs with regulated structures, (iv) porphyrin organic linkers synthesized to meet specific catalytic needs can greatly influence the selectivity and efficiency of the catalyzed reaction, and (v) although the rigidity and integrity of the POM are maintained after inclusion, its redox and acid-base properties are subsumed into those of the MOF as a whole [36–38]. Accordingly, porphyrinic POMMOFs have resulted in frameworks that simultaneously feature the unparalleled properties of all the pure components – POM, MP and MOF – including their catalytic properties, biomimetic properties, porosity and high thermal/chemical stability [39,40].

As mentioned earlier, the porphyrinic POMMOFs overviewed in this report are classified as porphyrinic POMOFs (type a in Scheme 8) and porphyrinic POM@MOFs (type b in Scheme 8). Both the MP and the POM combine with each other synergistically to enhance the catalytic activity of porphyrinic frameworks. POMMOFs of both types will be
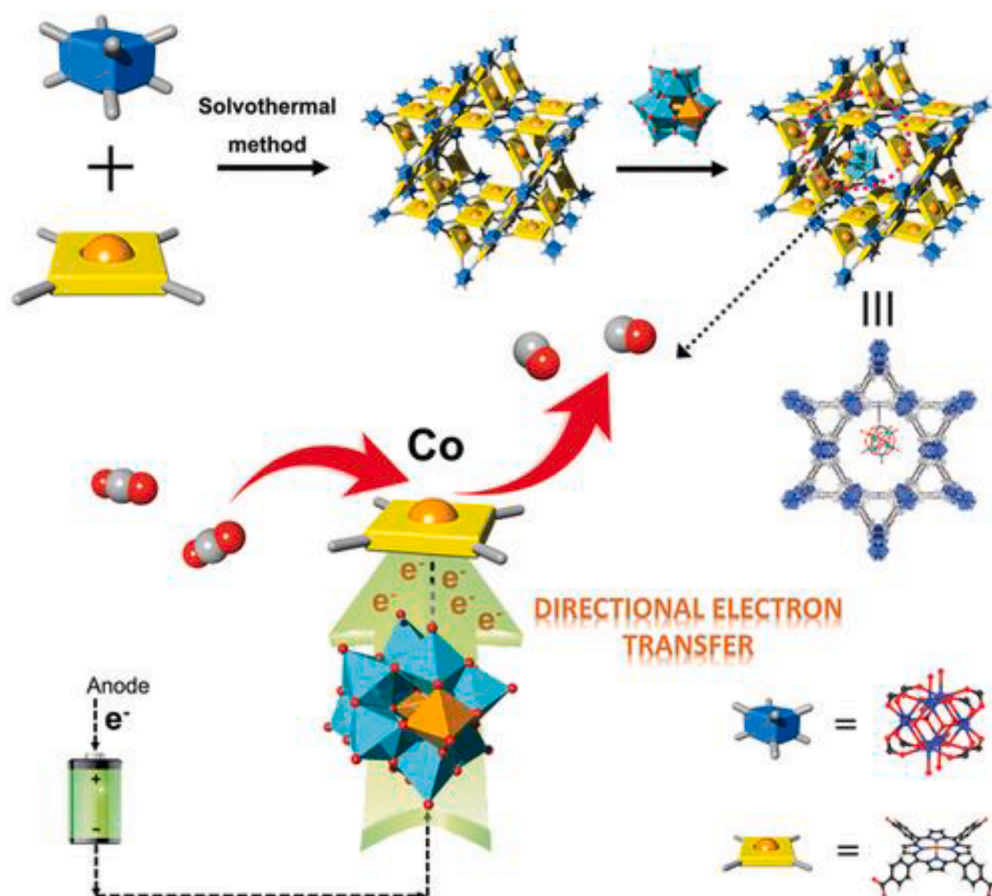
Fig. 5. Graphical demonstration of the fabrication procedure of Keggin-type POM encapsulated in PCN-222(Co) pores as an example (above), and scheme of suggested electron transmission through POM@PCN-222(Co) for CO_2 electrochemical reduction (bottom). Blue box: Zr-based second building unit, yellow square: TCPP linker, yellow ball: Co metal center. Reproduced with permission from Ref [155]. Copyright 2021 Wiley-VCH. (For interpretation of the references to color in this figure legend, the reader is referred to the web version of this article.)

discussed in detail according to their catalytic uses, ordered structures and the chronology of the MOF synthesis. Table 1 summarizes recent development related to the synthesis and heterogeneous catalytic exploitation of porphyrinic POMMOFs.

3.2. Formation and catalytic utilizations of porphyrinic POMOFs (type a)

Step-by-step processes are known for manufacturing porphyrinic POMOFs; there are two possibilities to implement this method [10]: (i) attaching metal ions/clusters to POM precursors to form metal-anchored POMs (metal-modified POMs), which can then be employed as pre-fabricated SBUs to interconnect with a secondary auxiliary linker and/or metal ion/cluster; (ii) ligand-modified POMs are formed by assemblage of pertinent organic ligands and POM precursors (POM-hybrids), and then further bind to metal ions/clusters. Thus, both approaches result in POMOFs. Until now, majority of the synthesized porphyrinic POMOFs have only been made via first method which is illustrated in Scheme 11. However, POMs are oxygen-abundant anionic frameworks and due to the powerful terminal M=O bonds, it is challenging to attach POMs directly to the organic ligands [36,44]. It is only under very specific conditions that the superficial bridging and terminal O atoms of POM-hybrids can be functionalized with metal ions/clusters and/or organic ligands, as a result of which there are few instances of this category of porphyrinic POMMOFs fabricated by means of second process.

3.2.1. Nonlinear optical (NLO) properties of porphyrinic POMOFs

Potential nonlinear optical (NLO) materials containing POM-porphyrin systems, in which porphyrin electrons are connected to POM acceptors, are a promising strategy for increasing the transfer of photogenerated electrons from POMs to other components of the system, and for boosting the responsivity of porphyrin to laser irradiation. Intrigued by these characteristics, three novel supramolecular inorganic–organic hybrid materials – $[H_2TPP]_{1.5}[SW_{11}VO_{40}].5CH_3CN \cdot 4H_2O$ **1** (SWV_1), $[H_2TPP]_2[SW_{10}V_2O_{40}].4CH_3CN \cdot 3H_2O$ **2** (SWV_2), and $[H_2TPP][SW_{12}O_{40}] \cdot 4H_2O$ **3** (SW), comprising vanadium-modified Keggin-type anion $[SW_{12-n}V_nO_{40}]^{(2+n)-}$ (n = 0–2) (Fig. 1a) and $[H_2TPP]^{2+}$ cation (Fig. 1b) – were synthesized to study their third-order NLO properties using an Nd:YAG laser [124]. The results were that, in terms of NLO performance and reduction potential, compound **2** was inferior to **1** but superior to **3** (SWV_1 > SWV_2 > SW). The key factor in improving their NLO effect is the degree of vanadium substitution, which affects the degree of charge transfer from porphyrin to POM on excitation by laser irradiation.

There is a remarkable decrease in transmission efficiency, from 70, 24.1 and 23.0 to 27.2 %, ongoing from compound **1**, **2** and **3** to $[H_2TPP][ClO_4]_2$ with input influence at 0.88 J cm^{2-}. From Fig. 1c, albeit the transmission kept approximately constant at 0.88–2.15 J cm^{2-}, it decreased drastically with increase in input influence above 2.15 J cm^{2-} and once again remained almost constant at T = 7 %. This may be attributed to nonlinear reserved saturated absorption (RSA) and reflection trigged by π-electrons which are delocalized over the entire porphyrin (for input influence lower than 2.15 J cm^{2-}). With respect to the input influence more than 2.15 J cm^{2-}, the main reason for transmission decrease may stem from outcome of thermal impact on the NLO traits [125]. It can be seen that porphyrin-POM materials have the
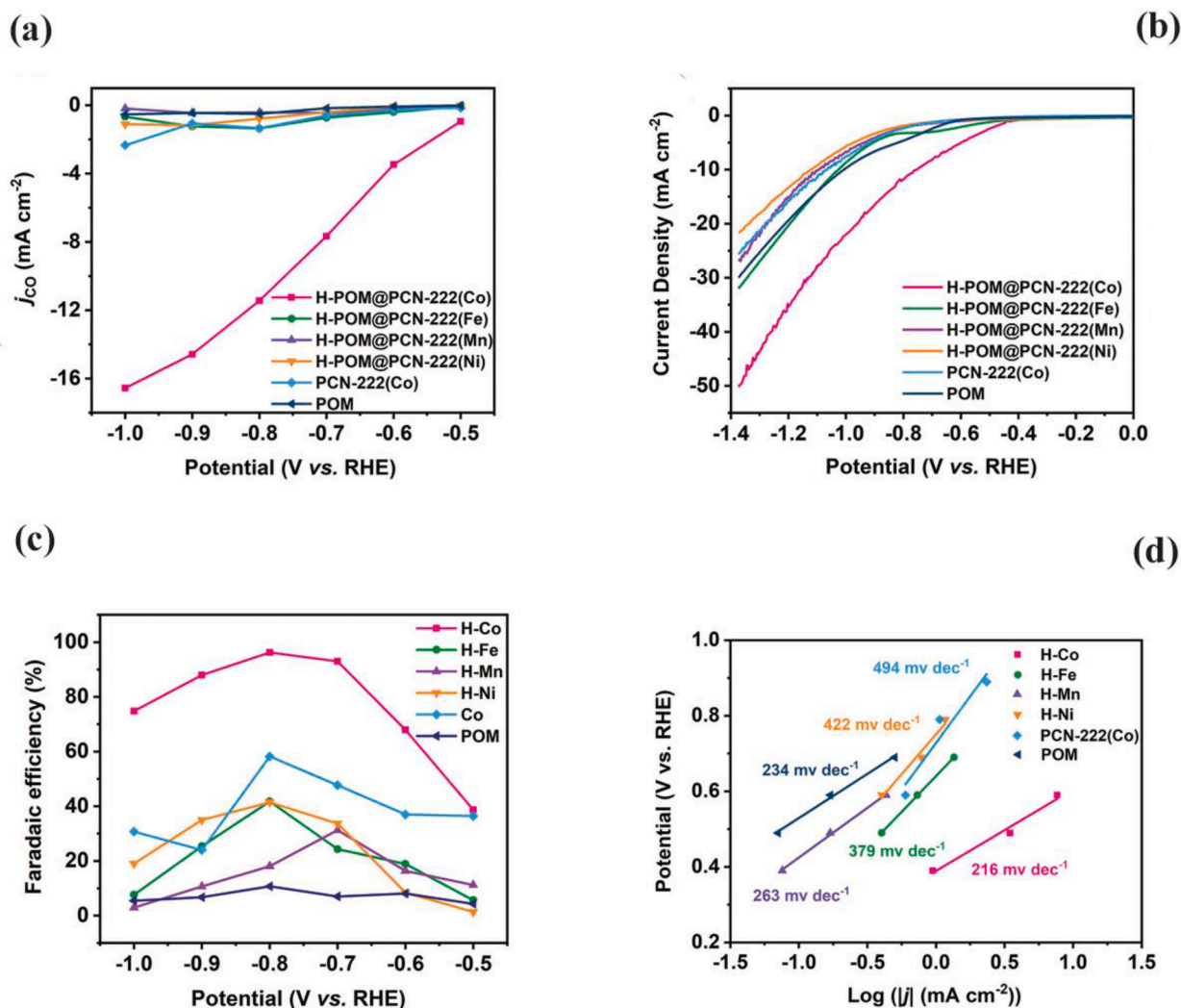
Fig. 6. Electrochemical CO_2RR efficiency of H-POM@PCN-222(M) (M = Co, Fe, Mn and Ni), PCN-222(Co), and POM. a) current density of CO at various potentials; b) LSV plots; c) Faradaic proficiencies of CO with several metals employed in the MOF over a range of potentials; and d) Tafel diagrams. Reproduced with permission from Ref [155]. Copyright 2021 Wiley-VCH.

potential ability to significantly weaken laser rays at high intensities, whilst displaying considerable transmittance of light at lower intensity. More importantly, it is evident that since the lowest unoccupied states of $[H_2TPP][ClO_4]_2$ are higher than those of POM, the electrons excited from porphyrin can relocate to POM when subjected to laser irradiation, leading to the improvement of the NLO properties of the POMOFs compared to the parent porphyrin (Fig. 1d). In the meantime, the comparison regarding the LUMO (lowest unoccupied molecular orbital) levels of $[H_2TPP][ClO_4]_2$ and that of POMs, ΔE ($[H_2TPP][ClO_4]_2$-POM), exhibited the descending trend in a series of ΔE ($[H_2TPP]$ $[ClO_4]_2$-SWV_1) > ΔE ($[H_2TPP][ClO_4]_2$-SWV_2) > ΔE ($[H_2TPP]$ $[ClO_4]_2$-SW). In this respect, despite the vanadium introduction could lower the LUMO levels of POMs, the number of V atoms does not uniformly affect the LUMO levels, which were assumed as the prime factor to improve the NLO response in these POM-porphyrin hybrids. Whereas it was measured that the γ (second hyperpolarizability) values declined over the following trend: composite **1** (7.05×10^{-29} esu) > composite **2** (6.59×10^{-29} esu) > composite **3** (6.29×10^{-29} esu), the performances for the OL (optical limiting; limiting threshold) showed a decrease sequence as follows: composite **3** (0.54 J cm^{2-}) > composite **2** (0.37 J cm^{2-}) > composite **1** (0.28 J cm^{2-}). In consequence, it was observed that the γ values and OL performances were directly and inversely proportional to ΔE ($[H_2TPP][ClO_4]_2$-POM), respectively; demonstrating that

the POM-porphyrin systems are potentially applicable OL/NLO compounds according to the information acquired by nonlinear RSA and refraction.

Nonetheless, the nonlinear efficiency of MOF materials has hardly been studied [126,127]. As the MOF structure contains large and adjustable pores, different types of composites could be merged into networks to improve the NLO performance. POMs are a stable and cost-effective instance of inorganic clusters that may be viewed as perfect electron acceptors for excitation from organic moieties, principally because of the metal ions with high oxidation states. This present examination is intended to represent valuable information on the characteristic architectural correlations in porphyrinic POMMOF hybrids that provide reason to study them as potential innovative NLO constituents with superior hyperpolarizability. Due to the metal clusters' (POMs') own dπ-pπ electron conductance and conjugated dπ-dπ delocalization, the POMs themselves have notable NLO properties [128,129]. If the MLCT (metal to ligand charge transfer) and LMCT (ligand to metal charge transfer) characteristics of MOF units are introduced, the NLO properties of POMs are enhanced [130,131]. The delocalized π-electrons can promote NLO properties themselves; however, other ways to improve these properties in POMs have also been investigated [132,133]. POMs and the porphyrin-metal ion connections which cause the formation of the MOF structure play an important role

Table 4

Comparison of data reported for MOF-based materials for electrochemical reduction of CO_2.

MOFs	Electrolyte & pH	E (V vs. SHE)	Chief product	FE (%)	j_{co} (mA/cm^2)	TOF (h^{-1})	Refs
Co-POMOF	**0.5 M KHCO$_3$**	**−0.8 V (vs. RHE)**	**CO**	**98.7**	**−18.08**	**1656**	[134]
H-POM@PCN-222(Co)	**0.5 M KHCO$_3$**	**−1.0 V (vs. RHE)**	**CO**	**96.2**	**−16.56**	**481.38**	[155]
Co-POMOF	**0.5 M KHCO$_3$**	**−1.2 V (vs. RHE)**	**CO**	**>99**	**29.2**	**488**	[156]
CoCp$_2$@MOF-545-Co	0.5 M KHCO$_3$	−0.9 V (vs. RHE)	CO	97	−25.63	777	[157]
[Al$_2$(OH)$_2$TCPP-Co]	0.5 M KCO$_3$	−0.7 V (vs. RHE)	CO	76	−5.9	200	[158]
Fe-MOF-525	1 M TBAPF$_6$ in CH$_3$CN	−1.3 V (vs. RHE)	CO	60	5.9	469	[159]
Ni SAs/N-C	0.5 M KHCO$_3$	−1.0 V (vs. RHE)	CO	70.3	7.37	5273	[160]
Re-SURMOF	0.1 M TBAOH in CH3CN	−0.9 V (vs. RHE)	CO	92.9	4.8	690	[161]
ZIF-8	0.5 M NaCl	−1.8 V (vs. SCE)	CO	65	1.8	–	[162]
CR-MOF	0.5 M KHCO$_3$	−1.2 V (vs. RHE)	HCOOH	30	~10	–	[163]
NNU-15 (Co-MOF)	0.5 M KHCO$_3$	−1.1 V (vs. RHE)	CO	99.2	32.2	–	[164]
PCN-222(Fe)	0.5 M KHCO$_3$	−1.2 V (vs. RHE)	CO	91	~34	64	[165]
Zn-ReSURMOF	0.1 M TBAH/CH$_3$CN	−1.6 V (vs. NHE)	CO	93	2.5	–	[166]
Cu-BTC	0.5 M KHCO$_3$	−1.2 V (vs. SHE)	Oxalic acid	51	15–20	–	[167]
Cu@NU-1000	0.1 M NaClO$_4$	−0.82 V (vs. RHE)	HCOO$^-$	28	1.2		[168]

together in the nonlinear traits of POMMOFs due to the delocalization of porphyrin π-electrons onto the POM units [3,134–137].

3.2.2. Metalloporphyrin-POM supramolecular material to activate molecular oxygen

A step-by-step association protocol was introduced in order to avoid unwanted random connections between functionalized MPs, POMs and highly oxophilic f-block inorganic nodes (lanthanide ions). Firstly, the procedure involves connecting the metal ions to the POMs to produce metal-modified POMs. These were then allowed to bind to carboxylate-substituted MPs, giving rise to porous organic/inorganic hybrid systems which could be used as heterogenous catalysts for O$_2$ activation in an epoxidation reaction (Fig. 2a) [138].

Under moderate conditions, the synthesized [{Gd$_4$Co$_2$(Co$_4$P$_4$W$_{30}$)$_2$} (Mn-OCPP)] (**4**) showed excellent ability to epoxidize olefins, with turnover number (TON) of 220,000 and turnover frequency (TOF) of 22000 h^{-1} after 10 h, without losing its catalytic efficiency in consecutive cycles (Fig. 2b and 2c). The results gathered in Table 2 also confirmed that the catalytic efficiency (conversion of > 99 %) of the as-produced MOF **4** (entry 1) were superior to those of Mn-H$_8$OCPP (entry 2), {Co$_4$P$_4$W$_{30}$} (entry 3) and {Gd$_4$Co$_6$P$_4$W$_{30}$} (entry 4), which individually were 5, 59 and 63 %, respectively. For the epoxidation of styrene to styrene oxide, these results show that the combination of POMs and MPs (entry 5; 49 %) can boost catalytic efficiency to give extraordinarily high yields. It is noteworthy that the styrene substrate was completely oxidized with good epoxide selectivity (94 %) in about two hours at a catalyst concentration of 0.2 mol% (entry 1). In terms of product selectivity, the heterogeneous catalytic performance of MOF **4** exceeded those of its constituent species, Mn-H$_8$OCPP (84 %), {Co$_4$P$_4$W$_{30}$} (94 %), and {Gd$_4$Co$_6$P$_4$W$_{30}$} (92 %) (entry 2–4, respectively). In the catalytic epoxidation procedure, the selectivity of hybrid catalyst **4** also outstripped the basic combination of Mn-H$_8$OCPP and {Co$_4$P$_4$W$_{30}$} (entry 5; 86 %). Since the porphyrin Mn^{III} sites are inaccessible to substrate molecules due to the functionalized carboxylate groups on Mn-H$_8$OCPP, esterified metalloporphyrin (Mn-Me$_8$OCPP) was utilized in place of Mn-H$_8$OCPP under otherwise equivalent circumstances. The catalytic quality of homogeneous Mn-Me$_8$OCPP is likewise

less than those of **4**, as indicated in entry 6. In order to compare the catalytic efficiencies, a number of control catalysts based on {M$_4$P$_4$W$_{30}$} (M = Co^{II}, Mn^{II}) and M'-OCPP (M' = Co^{II}, Mn^{III}) connected by Gd^{III} ions were also synthesized (referred to as MM'-1). Additionally, these findings suggest that none of the other arbitrary mixtures or the basic precursors can equalize the great epoxidation competence of **4**. As shown in Table 2, the catalytic abilities of **4**, and the huge increase therein compared to its precursors (Mn-OCPP and {Co$_4$P$_4$W$_{30}$}), could be correlated with the cooperative effect of the active sites on the pore surface, and with other adjustments to the microenvironment, within catalyst **4** (entries 7–9).

Under the same circumstances, MOF **4** were also able to epoxidize a variety of other alkenes. The conversions progressively drop as substrate sizes increase (Table 2, entries 10–15). Although the electronic effect and steric constraint may also have an impact on the catalytic results, this is a characteristic feature of porous heterogeneous catalysts because chemical transformations require the presence of the substrate molecules to get a better access to the active sites in the cavities so as to yield highly efficient catalytic capabilities.

Table 3 compares the results for epoxidation of a variety of olefins, catalyzed by miscellaneous POMMOFs. The results show that the catalyst labelled **4** within this work, successfully built by photosensitive constituent (Mn-H$_8$OCPP) and strong reducing component (Gd$_4$M$_6$P$_4$W$_{30}$; M = Mn^{II}, Co^{II}, for the multielectron relocation) displayed the highest catalytic performance of all, with > 99 % conversion and high selectivity (94 %). These data also show a mismatch between the supreme epoxidation activity of **4** and the lesser catalytic effect shown by its individual components and by similar systems. The catalytic efficiency of porphyrinic POMOF **4** also greatly exceeded those documented for homogeneous molecular catalysts like POMs, MPs (Table 2), and other POMMOFs for epoxidization of olefins (Table 3) [139,140].

Former investigations exposed that the catalytic oxidation of styrene commences with O$_2$/t-BuOOH (radical mechanism), which could result in multiple by-products over various reaction pathways, extremely dependent on the catalyst and reaction circumstances (Table 3; entries 3, 4 and 8). As for the other previous POMMOF catalyst (Table 3; entries 2,
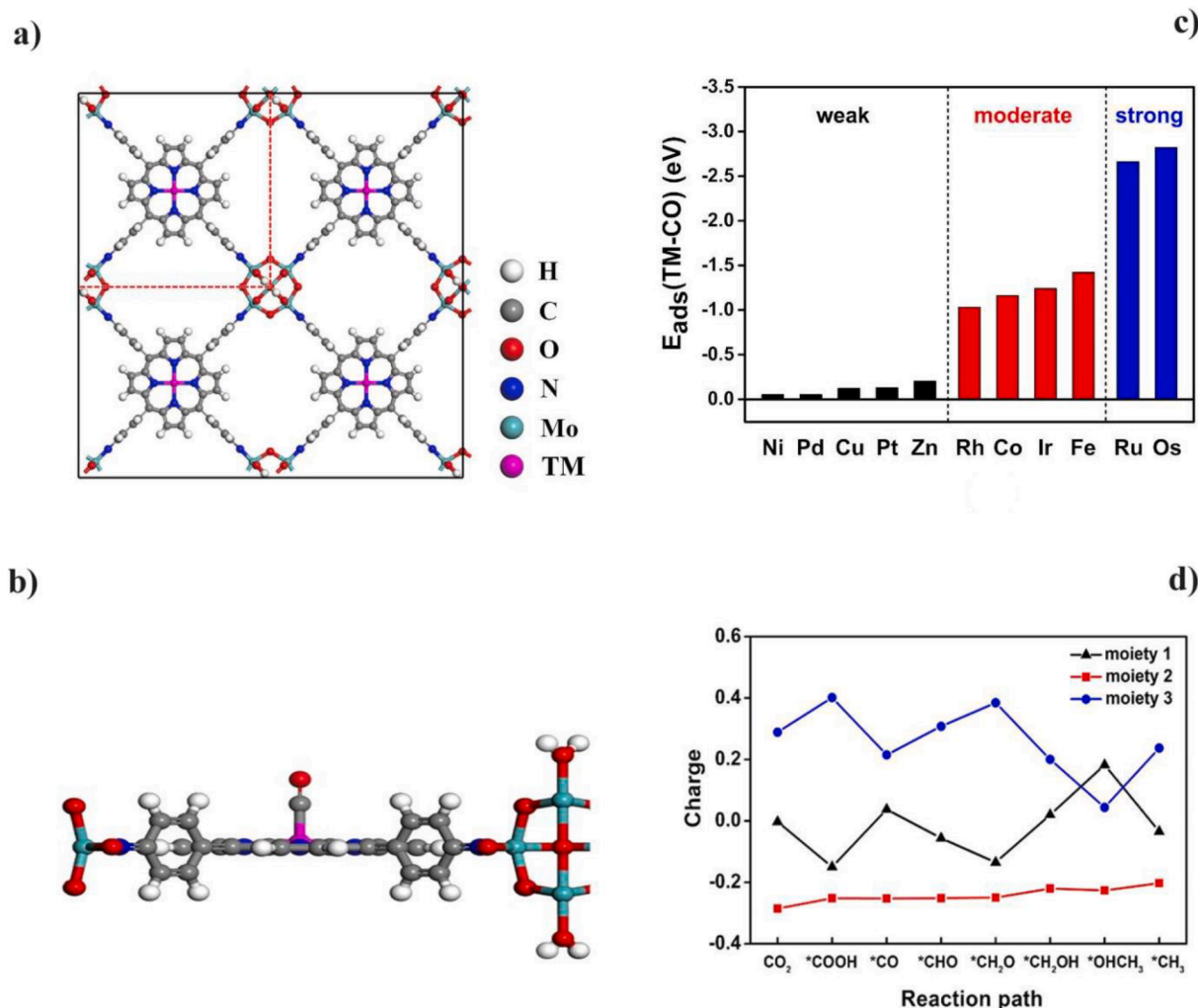
Fig. 7. (a) A general depiction of the DFT-optimized TM-POMOF structure (TM = Fe, Co, Ni, Cu, Zn, Ru, Rh, Pd, Os, Ir, Pt) in a 2 × 2 supercell; the red-dashed line indicates the primitive unit cell. (b) The adsorption potential of the TM-POMOFs. (c) The CO-TM-POMOF aggregate and the manner of bonding of CO. (d) Charge population analyses of the adsorbed intermediate on Co-POMOF, using the Hirshfeld charge of the three species 1 (adsorbed $C_xO_yH_z$), 2 (Co-N$_4$ unit) and 3 (Co-POMOF substrate). Reproduced with permission from Ref [169]. Copyright 2020 Royal Society of Chemistry. (For interpretation of the references to color in this figure legend, the reader is referred to the web version of this article.)

6 and 9), it was announced that the undesirable benzaldehyde was the frequently chief product, whilst the selectivity toward epoxide was comparatively lower. In the current case, porphyrinic POMOF **4** revealed very excellent selectivity toward styrene oxide (94 %). Notwithstanding, the selectivity of catalyst **4** was rather lower compared to entries 5 and 7 (both > 99), its conversion has yielded the highest amongst entire aforesaid reactions. Seemingly, the synergic collaboration of POM (Gd$_4$M$_6$P$_4$W$_{30}$) and metalloporphyrin complex (Mn-OCPP) in the **4** framework appears to perform a quite positive harmonious conjunction in regulating the chemical POM clusters' microenvironment when integrated into the structure of **4**. Accordingly, it leads to the establishment of highly effective active sites to epoxidize styrene.

These catalysts lack both high epoxidation capabilities and selectivity. It has been proven that the epoxidation reaction is initiated when MPs or POMs react with IBA (isobutyraldehyde) generating super-active acyl radicals. The reaction then proceeds through dioxygen activation to produce acylperoxy radicals which then epoxidize the olefins. From the point of view of this mechanism, catalyst **4** and its constituent moieties function synergistically to initiate and maintain the propagation of the radical chain reaction [138,141]. Then, a structural self-assembly approach that brings forward the strong reducing agent (POM) into porphyrinic MOF catalyst is very important to promote the procreation

of super-active acyl radicals being coupled with dioxygen activation. Additionally, the functions of active species were also evidently identified within the identical construction and their cooperative coupling efficacies were investigated in diverse catalytic reactions.

3.2.3. Selective CO$_2$ reduction via POM-Porphyrinic MOF electrocatalyst

If a POMOF contains POMs with low-valent metal ions that form electron-rich motifs capable of transferring electrons to MPs, this is advantageous for electron motility. Such systems have proven to be promising candidates for converting CO$_2$ to CO electrocatalytically. A series of identical state-of-the-art M−POMOFs [PMo$_8^V$Mo$^{VI}_{14}$O$_{35}$(OH)$_5$Zn$_4$]$_2$[MTCPP][2H$_2$O][1.5TBAOH] (M = Fe, Co, Ni, and Zn), in which (M−TCPP) is connected through Zn-ε-Keggin clusters, were obtained by the *in situ* hydrothermal method. They were thereupon examined for their ability in serving as the operative electrocatalytic element for CO$_2$ reduction (Fig. 3a) [150].

As a proof-of-concept, by comparison, the linear sweep voltammetry (LSV) (Fig. 4a) of the Co-POMOF showed far higher initial potential (-0.35 V) than that of Fe-POMOF, Ni-POMOFs and Zn-POMOFs (-0.53, −0.58 and 0.60 V, respectively). Co-POMOF displayed a minor overpotential (0.24 V) and the corresponding equilibrium potential was calculated −0.11 V for CO$_2$/CO when Co-POMOF was employed. The

Fig. 8. The graphical PDOS charts of (a) Fe-POMOF, (b) Co-POMOF, (c) Rh-POMOF and (d) Ir-POMOFs. Reproduced with permission from Ref [169]. Copyright 2020 Royal Society of Chemistry.

relatively higher total current density at -1.1 V (38.9 mA cm^{-2} of Co-POMOF) surpassed that of Fe-POMOF (25.1 mA cm^{-2}), Ni-POMOFs (20.02 mA cm^{-2}) and Zn-POMOFs (16 mA cm^{-2}), which demonstrates that Co-POMOFs is the best reductant of them all for purposes of catalyzing the reaction. Moreover, the value of the partial current density of CO for Co-POMOF (at -0.8 V) was 18.08 mA cm^{-2}. This value was 30 times as high as that obtained for Fe-POMOF (0.27 mA cm^{-2}), Ni-POMOFs (0.47 mA cm^{-2}) and Zn-POMOFs (0.02 mA cm^{-2}) (Fig. 4b). At the corresponding optimized potential (-0.8 V), the Co-POMOF gave the TOF with the high value of 1656 h^{-1} and a TON of 7693 in only 5 h, and its TON exceeded 53,000 after 35 h (Fig. 4c).

To further investigate the probable mechanism by which the reduction of CO_2 to CO on Co-POMOFs is accomplished, experimental and theoretical measurements were carried out (Fig. 3b). Initially, the Zn-ε-Keggin clusters grab an electron from the anode, which proceeds to emigrate to Co-porphyrin (in which as a result the Co(II) center is reduced to Co(I)). The Co(I) then reacts with CO_2 to produce the intermediate [Co(II)*COOH] by combining with proton-electron transmission. Next, Co(II)*COOH changes to Co(II)*CO. Eventually, the CO detaches from the catalyst surface and the process begins again.

During the last few years, many attempts have been made to use MOF materials, in conjunction with a variety of electrode materials, to develop more efficacious homo- or heterogeneous catalysts for the electrocatalytic reduction of CO_2 [39,60,151–154]. Amongst them,

POMMOFs have rarely been used for electrochemical CO_2 reduction reaction (CO$_2$RR). In 2021, Sun *et al.* announced a group of mixed-valence POMMOFs produced via PSM [155]. As shown in Fig. 5 (on the top), the formation process of POM@PCN-222(Co) is demonstrated as an instance. Architecturally, PCN- 222(Co) and PCN-222(Fe) are isoreticular. The two prominent channel dimensions of PCN-222(Co), which are spacious enough to embed a Keggin-POM with size of 10 Å, were obtained 16 and 36 Å, respectively. The mixed-valence POM ([Co^{III}Co^{II}(H$_2$O)W$_{11}$O$_{39}$]$^{7-}$) was accommodated into the channels of PCN-222(Co) via PSM to produce POM@PCN-222(Co). The as-made POM@PCN-222(M) (POM = [Co^{III}Co^{II}(H$_2$O)W$_{11}$O$_{39}$]$^{7-}$, M = Co, Fe, Mn, and Ni) were applied to accelerate the transfer of electrons in the process of selectively reducing CO_2 to CO. Of these systems, H-POM@PCN-222(Co) had the greatest Faradic performance, up to 96.2 %, with a longer resistance, more than 10 h (Fig. 5, bottom).

For the partial CO current density (-1.0 V vs reversible hydrogen electrode (RHE)), the values seen for H-POM@PCN-222(Fe) (-0.67 mA cm^{-2}), H-POM@PCN-222(Mn) (-0.19 mA cm^{-2}) and H-POM@PCN-222(Ni) (-1.1 mA cm^{-2}) were outstripped by that of H-POM@PCN-222(Co) (-16.56 mA cm^{-2}) (Fig. 6a). Furthermore, the total current density calculated for H-POM@PCN-222(Co) was increased to 50.07 mA cm^{-2}, with a reduction of the initial potential to -0.35 V, as a result of POM insertion (Fig. 6b). In addition, as shown in Fig. 6c, the Faradic proficiency of CO was measured (from -0.5 to -1.0 V). In this respect, H-
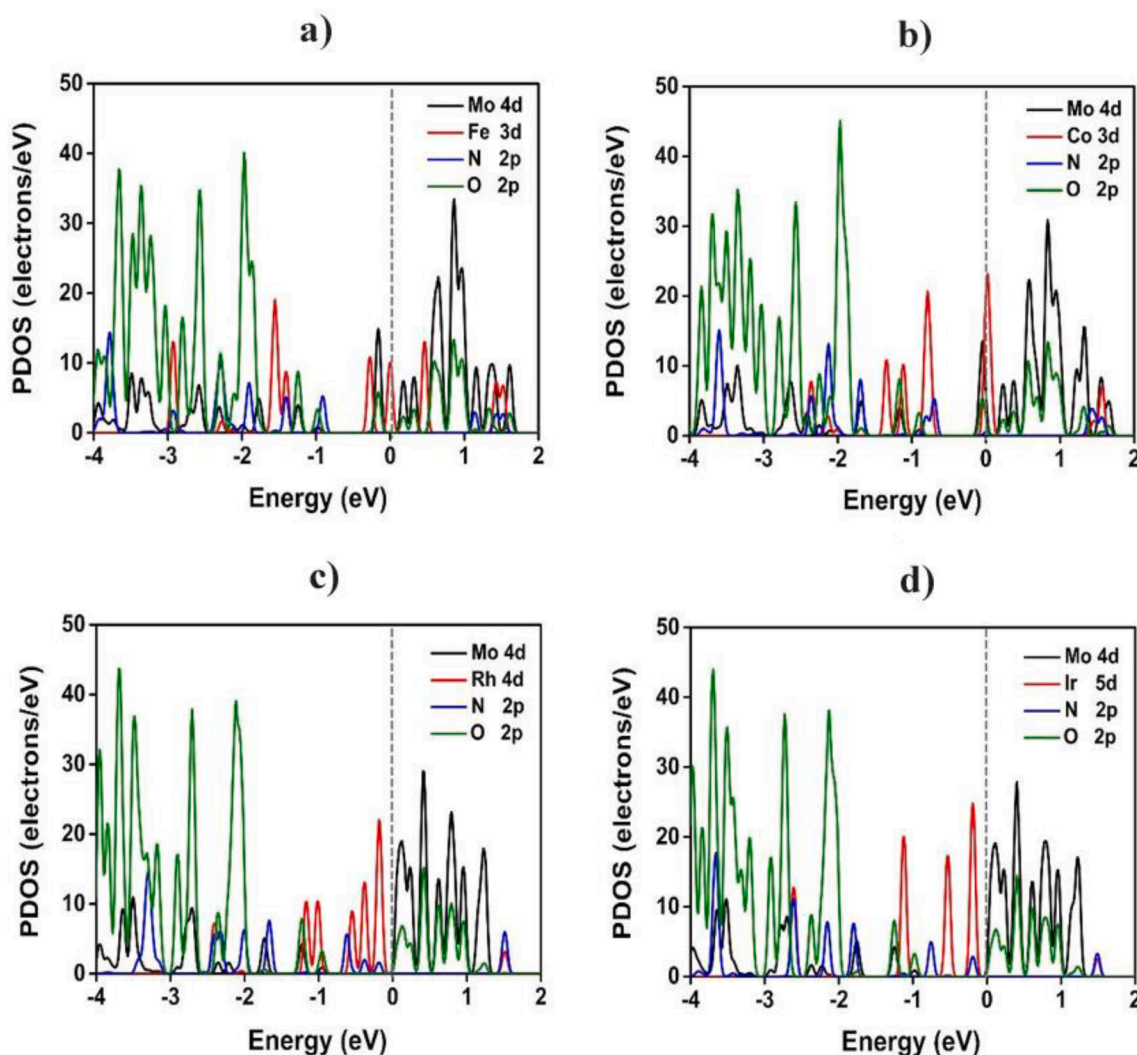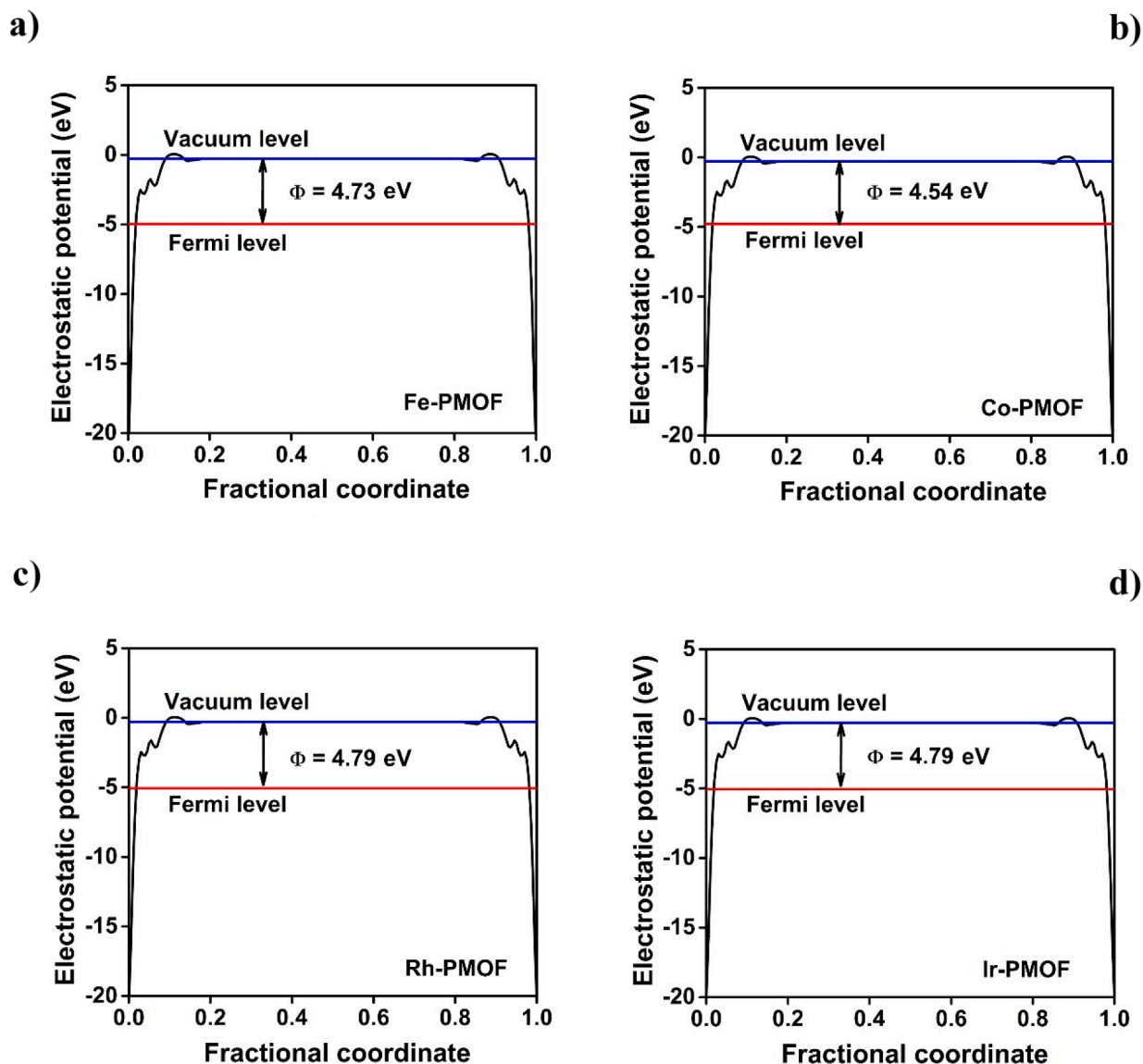
Fig. 9. The work functions of (a) Fe-POMOF, (b) Co-PMOF, (c) Rh-PMOF, and (d) Ir-PMOF. Reproduced with permission from Ref [169]. Copyright 2020 Royal Society of Chemistry.

POM@PCN-222(Co) exhibited a far greater FE_{CO} in this range, whose measured CO_2 electroreduction performance reached a maximum of 96.2 % at −0.8 V. This significantly exceeded the values for H-POM@PCN-222(Fe) (41.79 % at −0.8 V), H-POM@PCN-222(Mn) (31.27 % at −0.7 V), H-POM@PCN-222(Ni) (41.4 % at −0.8 V), PCN-222(Co) (58.2 % at −0.8 V) and POM (10.7 % at −0.8 V). The Tafel slope demonstrating the kinetics of the formation of CO gave values of 379, 263, 422, 494 and 234 mv.dec^{-1} for H-POM@PCN-222(Fe), H-POM@PCN-222(Mn), H-POM@PCN-222(Ni), PCN-222(Co) and POM, respectively. However, these are again outperformed by H-POM@PCN-222(Co), with the lowest slope of all – 216 mv.dec^{-1} – again confirming that, of all the incorporated metals, Co has the best potential kinetics to produce CO (Fig. 6d). The TOF of H-POM@PCN-222(Co) (481 h^{-1}, 1.0 V) also exceeds that of H-POM@PCN-222(M) and PCN-222(Co), again showing its higher catalytic efficiency for the CO generation reaction.

In addition, the electrocatalytic reduction efficiencies of Co-porphyrinic POMMOFs [150,155,156] also exceeded those declared for other MOF-based compounds, as compared in Table 4.

3.2.4. Lindqvist-co-porphyrinic MOF electrocatalyst for CO_2 reduction

Compared to their 3D MOF counterparts, it is expected that 2D porphyrinic MOFs have larger surface areas and more double-faced catalytic active sites that can facilitate CO_2 reduction. With these considerations in mind, tetra-(4-aminophenyl) metalloporphyrin (TM-TAPP) was combined with an electron-rich Lindqvist-pattern POM ($[Mo_6]^{2e/2H}$) to produce a set of two-dimensional TM-POMOFs (TM = Fe, Co, Ni, Cu, Zn, Ru, Rh, Pd, Os, Ir, Pt) (Fig. 7a) [169]. Since CO can play a crucial role as an intermediate in the process of multiple electron-reduction of CO_2, a study was performed for the CO adsorption potency on the TM-POMOFs' surface using DFT computations. The calculations revealed that CO constructs a TM-C bond, located above the focal porphyrinic TM, as shown in Fig. 7b. The adsorptive interaction of the TM-POMOFs with CO can be divided into three groups (Fig. 7c): (i) CO molecules are inclined to desorb from the exterior of the POMOF, as the adsorption potential is very weak. This is the case for Ni-POMOF, Pd-POMOF, Cu-POMOF, Pt-POMOF and Zn-PMOF, which have adsorption potentials of −0.05, −0.05, −0.12, −0.13, and −0.20 eV, respectively. (ii) The MOFs adsorb CO too vigorously, leading to dead-end species: this is the case for Ru-POMOF (-2.7 eV) and Os-POMOF (-2.9 eV) (strong
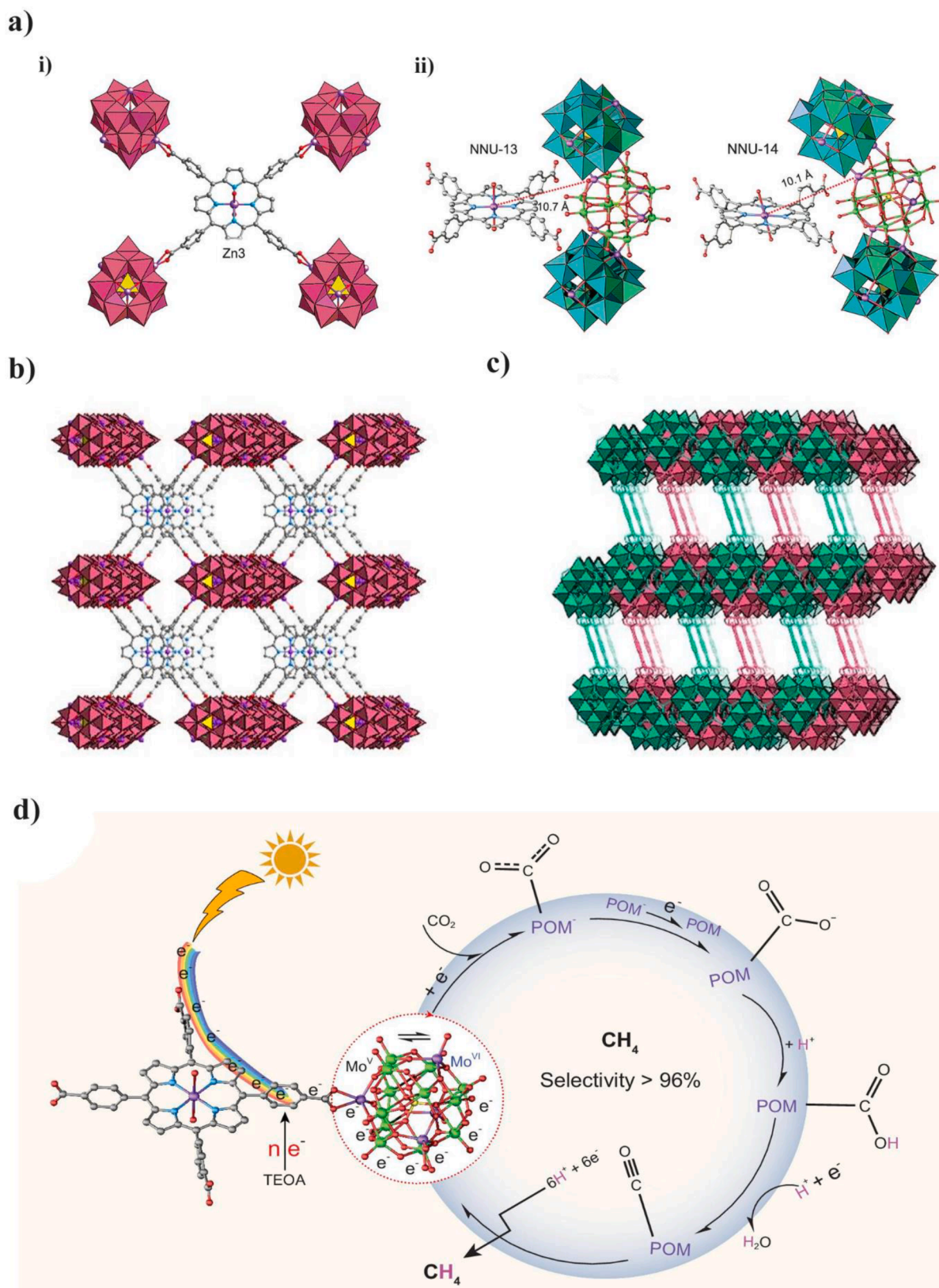
Fig. 10. Representation of ball-and-stick perspectives which (a) (i) show the concurrent assemblage of four POM units and each Zn-TCPP ligand and (ii) display the shortest distances between the Zn in MP and a Zn in the POM unit for both NNU-13 and NNU-14. Color key: Mo, green; Zn, purple; O, red; N, blue; P, yellow; C, grey. Hydrogen atoms and water molecules have been omitted for clarification. (b) 3-dimensional view of the POMCFs, (c) 2-fold interpenetrated frameworks across the b direction, and (d) suggested reaction mechanism of visible-light-driven photocatalytic conversion of CO_2 to CH_4. Reproduced with permission from Ref [170]. Copyright 2020 Oxford Academic. (For interpretation of the references to color in this figure legend, the reader is referred to the web version of this article.)
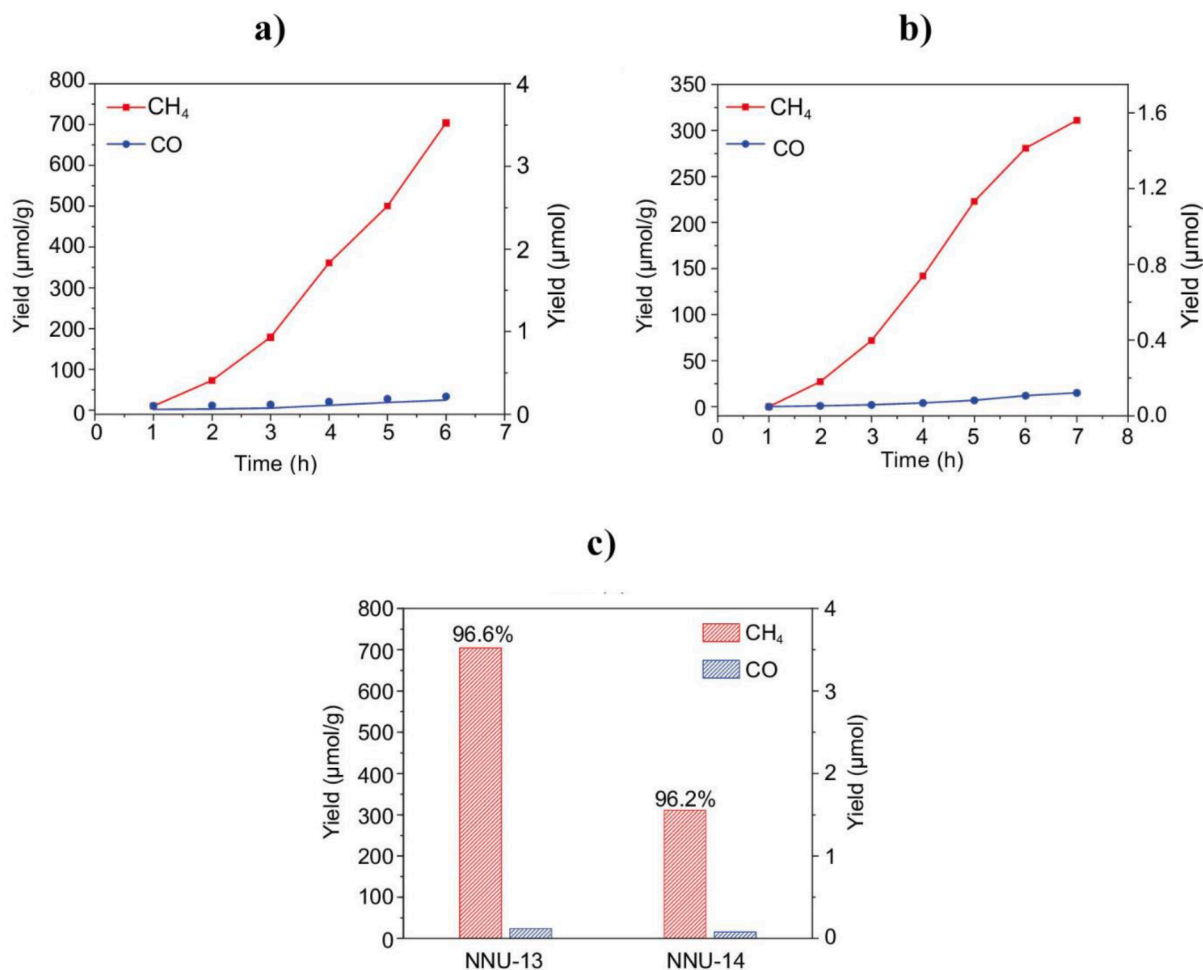
Fig. 11. The amounts of CO and CH_4 formation taking place under prolonged light irradiation in the presence of (a; top left) NNU-13 and (b; top right) NNU-14, and (c; bottom) the total CO and CH_4 yields and selectivity of gas products obtained in CO_2 photoreduction reaction. Reproduced with permission from Ref [170]. Copyright 2020 Oxford Academic.

interaction), making them as unsuitable for catalysis as the first, weakly-adsorbing group. (iii) The adsorption interaction is modest, neither too strong nor too weak – this is seen for Rh-POMOF, Co-POMOF, Ir-POMOF and Fe-POMOF, displaying absorption potentials of -1.03, -1.16, -1.24 and -1.42 eV, respectively. This intermediate-strength interaction makes it more likely for the CO intermediates to undergo subsequent reduction. Charge population investigations (Fig. 7d) showed that the main moiety which provides electrons is Co-POMOF (acting as an electron resource). It acts in conjunction with Co-N_4 (serving as an active site and transmitter agent), which accepts the electrons, enabling a flow of electrons between the Co-POMOFs and $C_xO_yH_z$ during the CO_2 electroreduction reaction.

The partial density of states (PDOS) investigations (Fig. 8a-d) yielded the electrical conductivities near the Fermi level for the four excluded TM-POMOFs (Fe, Co, Rh and Ir), which were 0.18, 0.05, 0.24 and 0.26 eV, respectively. This implies that the best performing of them all would be Co-POMOF. In addition, it explicitly ensures that only the $[Mo_6]^{2e/2H}$ clusters appended to Co-PMOF would have any significant number of Mo-4d states that could cross the Fermi level. Furthermore, this also leads to stronger overlap with the Co-3d states (from the cobalt-porphyrin unit) near the Fermi level. Another consequence is that, on account of the interacting bands' very similar energy levels and spatial overlap, there is very little barrier to acceptance and donation of electrons. This therefore facilitates the migration of the electrons (gained from the $[Mo_6]^{2e/2H}$ motifs) onto the Co-porphyrinic rings.

Meanwhile, the work functions of all four best-performed POMOF materials (Fe-POMOF, Co– POMOF, Rh-POMOF, and Ir-POMOF) were also examined (Fig. 9a-d). The observations indicated that those of Fe-POMOF (4.73 eV), Rh-POMOF (4.79 eV), and Ir-POMOF (4.79 eV) achieved higher than that of Co-POMOF (4.54 eV). It infers due to the lower value of work function for Co-POMOF, the plentiful electrons could take part in the electrochemical process more effectively, deriving the greater performance in CO_2RR. This ultimately profits to an actually higher catalytic ability. As a consequence, the Co-POMOF can own superior capability for CO_2 reduction to that of Fe-POMOF, Rh-POMOF and Ir-POMOF.

3.2.5. CO_2-to-CH_4 photoconversion ability of POM-connected porphyrinic MOF

In recent decades, CO_2 levels in the atmosphere have increased as a result of the ongoing and increasing trend of fossil fuel consumption. In consequence, the solar-driven photocatalytic conversion of CO_2 into a profitable energy source such as CH_4 is of immense significance from the point of view of sustainable development. In pursuit of this goal, well-defined Zn-ε-Keggin-grafted metalloporphyrin coordination frameworks (POMCFs), constructed around an ε-Keggin POM structure (PMo_{12}), were impregnated by tetrahedral nodes of four Zn (II) ions (Fig. 10a-c). The two reported POMOFs $[PMo_8^VMo_4^VO_{35}(OH)_5Zn_4]_2$[Zn-TCPP][$2H_2O$]·xGuest (**NNU-13**) and $[PMo_8^VMo_4^VO_{35}(OH)_5Zn_4]_2$[Zn-TCPP] [$2H_2O$]·yGuest (**NNU-14**), showed unrivaled photocatalytic activity (96.6 % and 96.2 %, respectively) at selectively reducing CO_2 to CH_4 [170].
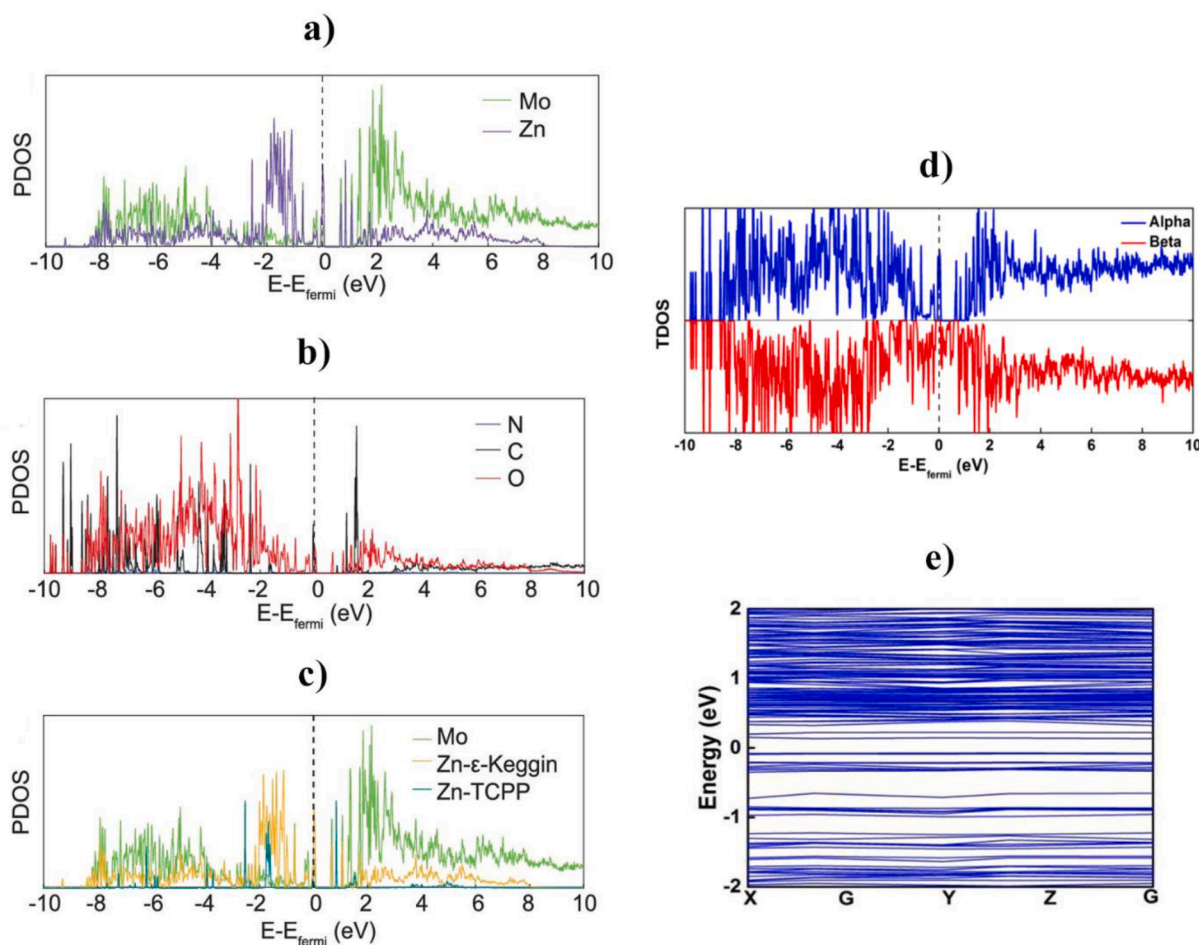
Fig. 12. PDOS calculations of (a; top left) Mo and all Zn atoms, (b; middle left) C, O and N atoms, (c; bottom left) Zn atoms in the TCPP linker andMo, and Zn atoms in Zn-ε-Keggin, (d) TDOS and (e) the band structure of NNU-13. Reproduced with permission from Ref [170]. Copyright 2020 Oxford Academic.

Further details on the selective reduction of CO_2 to CH_4 and CO upon prolonged visible light irradiation are shown in Fig. 11a and Fig. 11b. After 6 h and 7 h of the reaction proceeding, **NNU-13** and **NNU-14** produced 3.52 μmol (i.e. 704 μmol) and 1.56 μmol (i.e. 312 μmol) of CH_4, respectively. Although their CH_4 generation rate was permanently high, the CO output was negligibly low. By comparison, the CO amounts specified after the reaction completion were 4.2 μmol $g^{-1}h^{-1}$ (**NNU-13**) and 1.2 μmol $g^{-1}h^{-1}$ (**NNU-14**). Besides, both **NNU-13** and **NNU-14** displayed higher selectivity for CH_4 ((**NNU-13**; 96.6 %) and (**NNU-14**; 96.2 %)) than those of CO (less than 5 % for both) which are resulted from synergistic conjunction between the POM and TCPP (Fig. 11c). It is also valuable to express that the performances of photocatalytic reduction of CO_2 in terms of both the selectivity and the activity of POMCFs toward CH_4 were the uppermost among the stated heterogeneous photocatalysts [171–177]. At a monochromatic irradiation of $\lambda = 550$ nm, the quantum yields of **NNU-13** (0.04 %) and **NNU-14** (0.02 %) apparently indicate their substantial ability to reduce CO_2 efficaciously. The TONs and TOFs calculated for **NNU-13** and **NNU-14** for creation of CH_4 were 3.56 and 1.57 h^{-1}, and 164.80 and 62.3 h^{-1}, respectively, suggesting that the second catalyst is an ideal candidate for selectively converting CO_2 to CH_4.

Additionally, DFT calculations were done to probe the mechanism of charge-carrier separation. It can be seen that from PDOS measurements (Fig. 12a-c) that the higher level of the valence band (VB) is formed from states which mix several different elements, meaning that its makeup involves both the POM and the MP linker. O 2p, Zn 3d and Mo 4d states contributed to the lower level of the conduction band (CB), implying that only POM contribute significantly to this band. Moreover, the

results indicated that only POM act as electron acceptors, while both POM and the TCPP ligand serve as electron donors. It can be seen from the total density of states (TDOS) and the band structure of **NNU-13** (Fig. 12d and 12e) that the alpha-DOS (DOS: density of state) is unlike to the beta-DOS, suggesting the metalloporphyrin coordination framework (MCF) possesses single electron and magnetic trait. In this occasion, the VB electrons of TCPP ligands in MCF which are exited upon light irradiation, are relocated to the CB of POMs to reduce CO_2.

Taken together, the empirical and theoretical data suggest that the mechanism of the CH_4 photoreduction production (Fig. 10d) is that the porphyrin units generate electrons, primarily after light absorption. This prompts the transfer of the photo-generated electron to the central metal ion, which results in CO formation as the initial intermediate product. As the upper part of the VB is predominantly located on the TCPP linker in both of the catalysts, the electron moves to the POM segment via the TCCP linker. Thereafter, the POM species facilitate electron transmission to CO_2, enabling the subsequent addition of water protons to generate CH_4 molecules with an overall addition of 8 electrons. CH_4 is produced as the prevailing product with high selectivity.

Huang and coworkers (2022) synthesized a novel series of porphyrinic M−POMOFs ([$PMo_8^VMo_4^{VI}O_{35}(OH)_5Zn_4^{II}$]$_2$[$Fe^{III}$-TCPP-Cl]·Guest; [$PMo_8^VMo_4^{VI}O_{35}(OH)_5Zn_4^{II}$]$_2$[$M^{II}$-TCPP][$H_2O$]·Guest; M = Zn, Ni, Cu, Co, and Mn) via a hydrothermal protocol (Fig. 13) [156].

Fig. 13a-d illustrates MP (M−TCPP (M = Fe^{III}, Zn^{II}, Ni^{II}, Cu^{II}, Co^{II}, and Mn^{II}) carboxylic linkers) where the assemblage of reductive Zn-ε-Keggin and six various M−TCPPs created 3D frameworks of porphyrinic M−POMOFs. XRD measurements revealed a virtually similar framework, having the orthorhombic *Fmmm* space group. In case of Fe
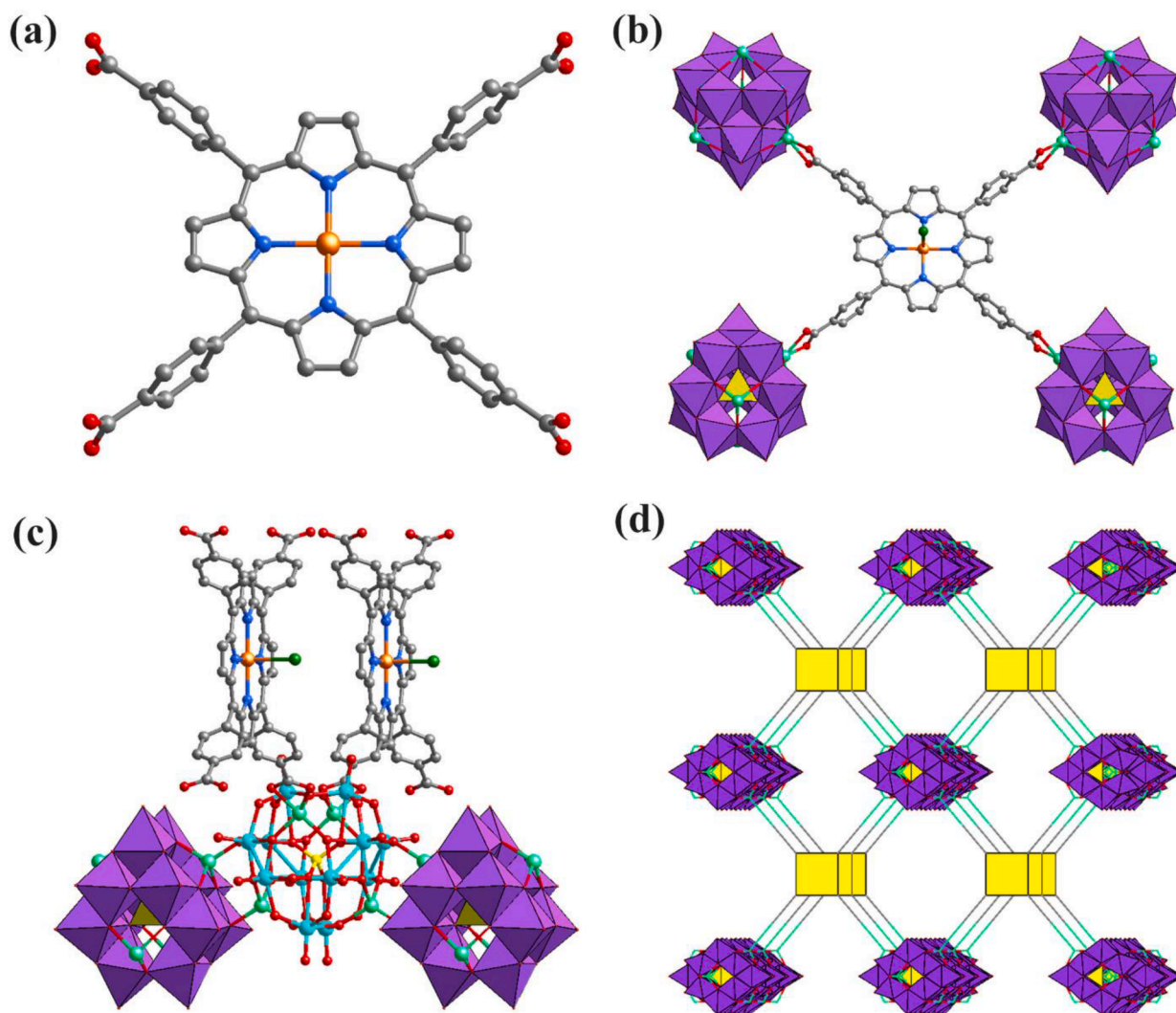
Fig. 13. The crystalline architecture of porphyrinic M−POMOFs. (a) M−TCPP (M = Fe^{III}, Zn^{II}, Ni^{II}, Cu^{II}, Co^{II}, and Mn^{II}) carboxylic linkers. In the case that the M is replaced by Fe, it also connected to a Cl ion in the axial position. Color code: C, black; N, blue; O, red; P, yellow; Cl or O, dark green; Mo, lake blue; Fe, golden; Zn, light green; (b) coordination environment of the Fe-TCPP unit. (c) coordination environment of the Zn-ε-Keggin cluster. (d) 3D frameworks of porphyrinic M−POMOFs. Reproduced with permission from Ref [156]. Copyright 2022 Science. (For interpretation of the references to color in this figure legend, the reader is referred to the web version of this article.)

(III), it attaches to four N atoms of the porphyrin and a distorted Cl atom axially. Whereas for other metals (Co^{II}, Ni^{II}, Zn^{II}, Mn^{II}, and Cu^{II}), they connect through four N atoms and a distorted O atom donating from H$_2$O. Moreover, each Zn-ε-Keggin coordinates to two M−TCPP linkers and two other Zn-ε-Keggin segments. At the same time, each M−TCPP attaches to four Zn-ε-Keggin fragments.

Their observations indicated a superior photocatalytic reduction (PCR) performance of Fe-POMOF in production of CH$_4$ (922 μmol g^{-1}) with higher selectivity, of up to 97.2 %.

Fig. 14a and 14b shows that the CH$_4$ generation for different M−POMOFs decreases in the series of Fe (922 μmol g^{-1}) > Zn (704 μmol g^{-1}) ≫ Ni (29.9 μmol g^{-1}) > Cu (3.8 μmol g^{-1}) > Co (3 μmol g^{-1}) ≈ Mn (2.9 μmol g^{-1}). A similar trend was seen in the selectivity of these porphyrinic M−POMOFs, diminishing in the order Fe (97.2 %) > Zn (96.6 %) ≫ Ni (52.0 %) > Cu (14.2 %) > Co (8.8 %) > Mn (4.5 %). Thus Fe-POMOF exhibited both highest CH$_4$ production and the highest selectivity.

To further investigate ECR performances of M−POMOFs, LSV measurements (Fig. 14c) were exploited at the saturated CO$_2$ atmosphere in 0.5 M KHCO$_3$ solution. Irrespective of the large current densities of those other four M−POMOFs [Mn (20.2 mA cm^{-2}, Zn (21.0 mA cm^{-2}), Cu

(25.0 mA cm^{-2}) and Ni (27.1 mA cm^{-2})] (under −1.2 V vs RHE), Co– and Fe-POMOFs exhibited the highest values (29.2 and 30.1 mA cm^{-2}, respectively). Furthermore, in order to study the dynamics activity of electrical catalysts, Tafel slopes were employed (Fig. 14d). Through this survey, the amounts gained for other M−POMOF were Zn (385 mV decade^{-1}), Mn (263 mV decade^{-1}), Cu (140 mV decade^{-1}) and Ni (107 mV decade^{-1}), respectively. Notwithstanding, those acquired for Co-POMOF (70 mV decade^{-1}) and Fe-POMOF (73 mV decade^{-1}) were comparatively smaller. It can be concluded that the less values which were calculated for Co-POMOF and Fe-POMOF, the higher efficient charge transfer and the bigger active surface; resulting in an extraordinary kinetics of reaction to generate CO remarkably.

Table 5 shows a comparison of the CH$_4$ generated by porphyrinic M−POMOF [139,154] with the amount generated by other previously-published MOF-based frameworks. The PCR efficiency of porphyrinic Fe-POMOF and Zn-POMOFs significantly exceeds that of the other MOFs listed.

a)

b)

c)

d)
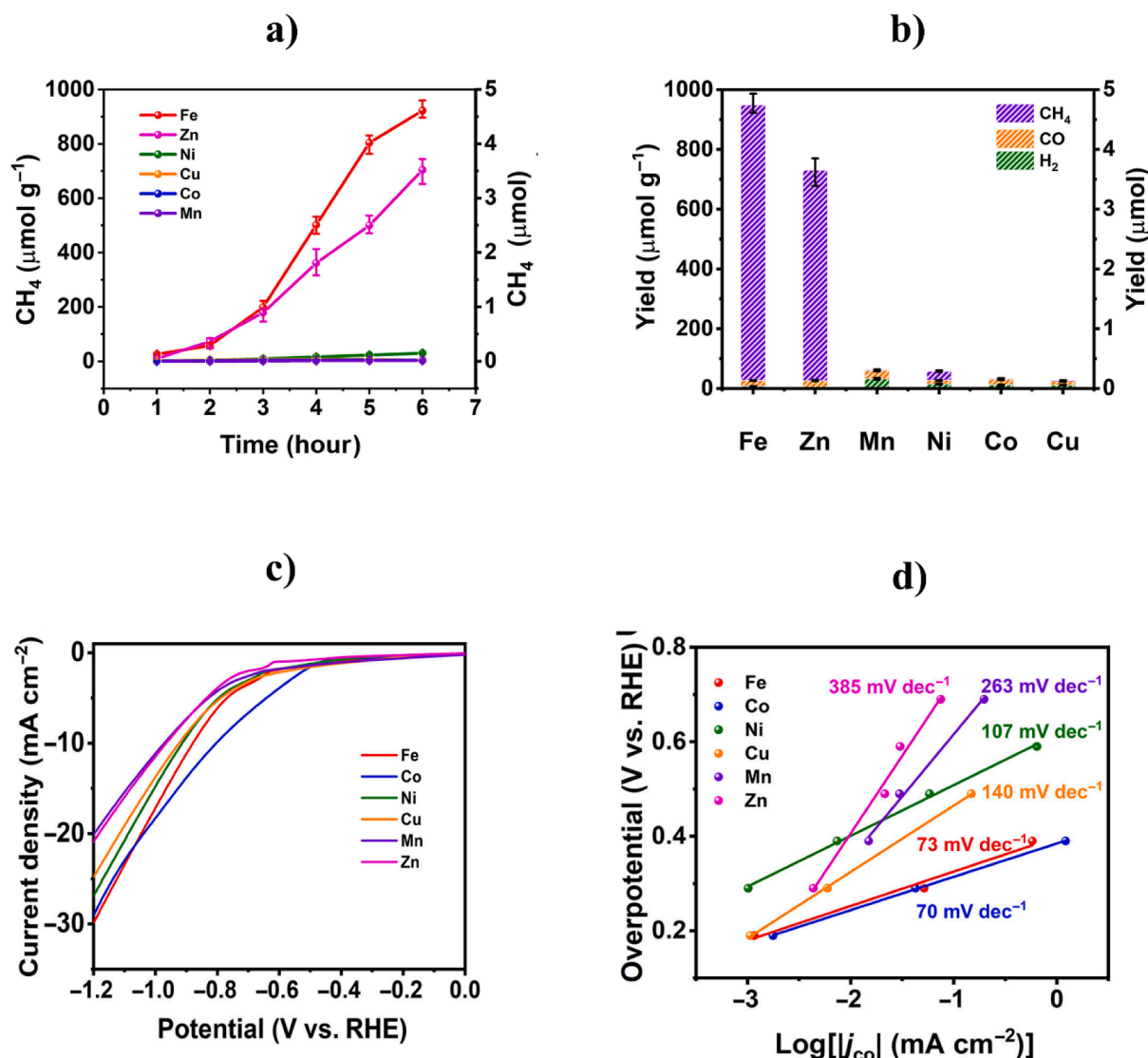
Fig. 14. PCR efficiency of porphyrinic M−POMOFs. (a) CH_4 amounts generated versus the visible irradiation time. (b) The relative output of CH_4, CO, and H_2 from the photocatalytic reduction reaction after 6 h. (c) LSV diagrams which were achieved in 0.5 M $KHCO_3$ electrolyte alongside applying the saturated CO_2 atmosphere (99.999 %), and (d) Tafel slopes of M−POMOFs for CO_2 reduction. Reproduced with permission from Ref [156]. Copyright 2022 Science.

3.3. Construction and catalytic applications of porphyrinic POM@MOFs (Type b)

It is often possible to prepare porphyrinic POM@MOFs by a PSM process in which POM materials are physically absorbed on the surface and are entrapped inside the cavities. It is difficult for single X-ray crystallography to assess the structures formed by this method, and the desired MOF architecture can be procured by several methods of immobilization including covalent grafting, encapsulation, substitution, sol–gel approaches, impregnation, electrostatic interactions and ion exchange. Amongst the aforementioned strategies, impregnation and encapsulation are the most experimentally pragmatic [3]. Briefly, impregnation involves submersion of pre-assembled MOFs, with voids of appropriate shape and size, in a solution of a suitable POM. In view of the weak interaction between the guest (POM) and the host (MOF), it is typical for this strategy to have some downsides when synthesizing POM@MOFs, such as leaching, lack of proper recyclability, inhibition of large pores, low uniformity, and the POM being located on exterior of the MOF structure instead of inside it (Scheme 12a) [10,36]. On the other hand, Encapsulation involves the placement of a guest into the pores of the host and is not often reversible; however, it too has

drawbacks, as it leads to a decrease in the catalytic efficiency as a consequence of aperture hindrance and lower diffusion – although this also has the advantage of diminishing the possibility of leaching and accumulation of the loaded POMs in the event that the POM diameter is bigger than the MOF's channel size (Scheme 12b) [44].

3.3.1. POM@MOFs constituted from tetrapyridyl porphyrin and bimetallic oxides

In 1999, simple covalently-tessellated 3-D frameworks consisting of tetrapyridylporphyrin (tpypor) ligand connected via bimetallic oxides were prepared, with the formulas $[Cu(tpypor)Cu_2Mo_3O_{11}]$ (**5**) and $[\{Fe(tpypor)\}_3Fe(Mo_6O_{19})_2].xH_2O$ (**6**) [178]. When looking at the first (**5**) of these along the *c* axis, X-ray diffraction showed that the resulting frameworks were composed of $\{Cu(tpypor)Cu_2\}^{4+}$ units connecting $\{Mo_3O_{11}\}_n^{4n-}$ polyoxoanion chains (Fig. 15a). The architecture might also be viewed as $\{Cu_2Mo_3O_{11}\}$ oxide components attached to the [Cu(tpypor)] units. In the copper-containing POM@MOF, the Cu^{II} ions in the rigid porphyrin units prefer to adopt either a square planar (sq) or "4 + 1" and "4 + 2" coordination arrangement, which results in a noticeable propensity to bind directly to molybdate moieties. Three different Cu(II) coordination spheres were detected. The first one adopts a square

Table 5
Comparison of the PCR performances of various MOF-based materials for CH_4 production.

PCR MOF catalysts	Light (nm)	Time (h)	Products	Yield (μmol/g)	Refs
Fe-POMOF	$\lambda > 420$	**6**	CH_4	**922**	
			CO	**19**	**156**
			H_2	**8**	
NNU-13		**6**	CH_4	**704**	
			CO	**25**	**170**
NNU-14	$\lambda > 420$	**7**	CH_4	**311**	
			CO	**12**	
PCN-222	$\lambda > 410$	10	CH_4	35	
			CO	55	171
PCN-601	$\lambda > 410$	10	CH_4	101	
			CO	60	
NJU-Bai61	full light spectrum	4	CH_4	63	172
			CO	16	
			H_2	7.48	
ZrPP-1-Co	$\lambda > 420$	15	CH_4	8	
			CO	210	173
TiO_2-Mg-CPO-27	$\lambda = 365$	10	CH_4	40.9	
			CO	23.5	174
MAPbI3@PCN-221 ($Fe_{0.2}$)	$\lambda = 400$	25	CH_4	325	175
			CO	104	
$Cu_3(BTC)_2$@TiO_2	$\lambda < 410$	4	CH_4	11	176
MOF-525			CH_4	37	
			CO	384	
MOF-525-Zn	$\lambda > 400$	6	CH_4	70	177
			CO	670	
MOF-525-Co			CH_4	121	
			CO	1204	

planar CuN_4 coordination environment which is resided in the core porphyrin ligand. The second one displays square pyramidal CuN_2O_3 coordination geometry which is ligated via coordinating to pyridyl nitrogen atoms of two tpypor groups of $\{Mo_3O_{11}\}_n^{4n-}$ polyoxoanion. The third one also forms octahedral CuN_2O_4 segment coordinated by ligation to three or four oxo groups of the $\{Mo_3O_{11}\}_n^{4n-}$ chains (Fig. 15a and 15b).

As regards the other, Fe-containing POMMOF (**6**), each of the large pores generated by the $[\{Fe(tpypor)\}_3Fe]_n^{4n+}$ building blocks is filled by $\{Mo_6O_{19}\}^{2-}$ anions which are physically attached to the space-filling water molecules in an octahedral arrangement (Fig. 15c). The edge dimension of cationic matrix contains cubic building units made of $[Fe_8(tpypor)_6]^{8+}$ with the size of 9.833(1) Å. Here, within the cationic microstructure, two different Fe(II) coordination spheres were characterized. The first one is positioned in the heme core and is axially linked to two pyridyl nitrogen donors from two neighboring [Fe(typpor)] blocks. Whereas the other one is additionally bonded to six pyridyl nitrogen atoms in an octahedral geometry (Fig. 15d). The Fe^{II} sites, in contrast, always adopt a hexacoordinate geometry, supplying a cationic framework for molybdate polyoxides which can be conceived as a ship-in-the-bottle way of arranging metal-porphyrin structures with bimetallic POM clusters inside them.

3.3.2. Mn^{II}-porphyrin-POM-based hybrid framework as dye sweeper/alkylbenzenes oxidizer

To overcome the extreme difficulties posed by the different solubilities of POMs (hydrophilic) and porphyrins (hydrophobic), an effective two-step approach (with mild conditions) was applied, with the first step being the production of the zwitterionic component $\{[Mn^{III}(DMF)_2T\text{-}PyP](PW_{12}O_{40})\}^{2-}$ through the direct interaction of Keggin-type $H_3PW_{12}O_{40}$ with $Mn^{III}Cl\text{-}TPyP$ in dimethyl formamide (DMF). This was followed by reaction with $Cd(NO_3)_2\cdot4H_2O$ in a mixture of DMF and acetic acid to obtain the intercalated $\{[Cd\text{-}(DMF)_2Mn^{III}(DMF)_2TPyP](PW_{12}O_{40})\}\cdot2DMF\cdot5H_2O$ network (**7**) (Fig. 16a). The thus-fabricated framework was utilized as a dye scavenger and an oxidizing heterogeneous catalyst to prepare some phenyl ketones [179]. It is worth noting that under solvent evacuation, the as-gained MOF was porous because only one of the two void types can house a $[PW_{12}O_{40}]^{3-}$ anion. The other is occupied by solvent molecules, and forms enormous 1D channels with dimensions of 5.36(1) Å × 12.44(1) Å; this is shown in Fig. 16b.

As demonstrated clearly in Fig. 16c, just 1 g of solid MOF (**7**) can capture around 0.033 mmol of the methylene blue (MB), 0.063 mmol of the rhodamine B (RhB) and 0.057 mmol of the crystal violet (CV) dyes, which are remarkably higher values than those of $Mn^{III}Cl\text{-}TPyP$ and
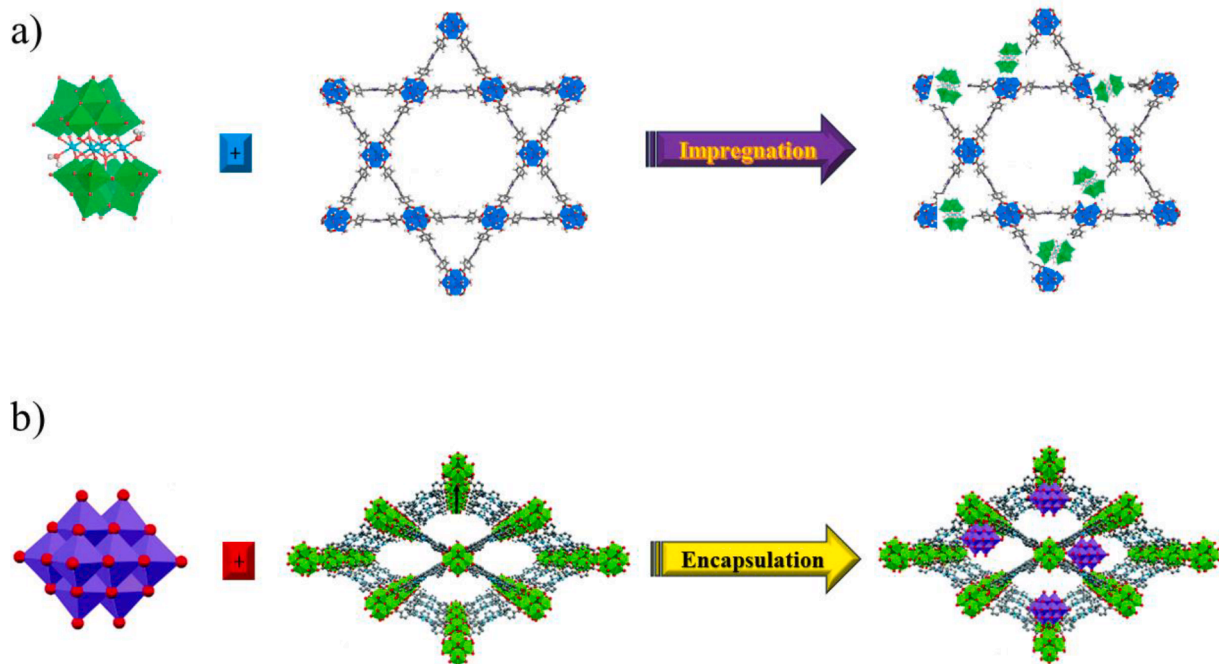
Scheme 12. General demonstration of fabrication approaches of porphyrinic POM@MOFs which are synthesized via (a) impregnation absorbed on the MOF surface, and (b) encapsulation accommodated into the MOF pores. Reproduced with permission from Ref [193,202]. Copyright 2018 American Chemical Society and 2020 Royal Society of Chemistry.
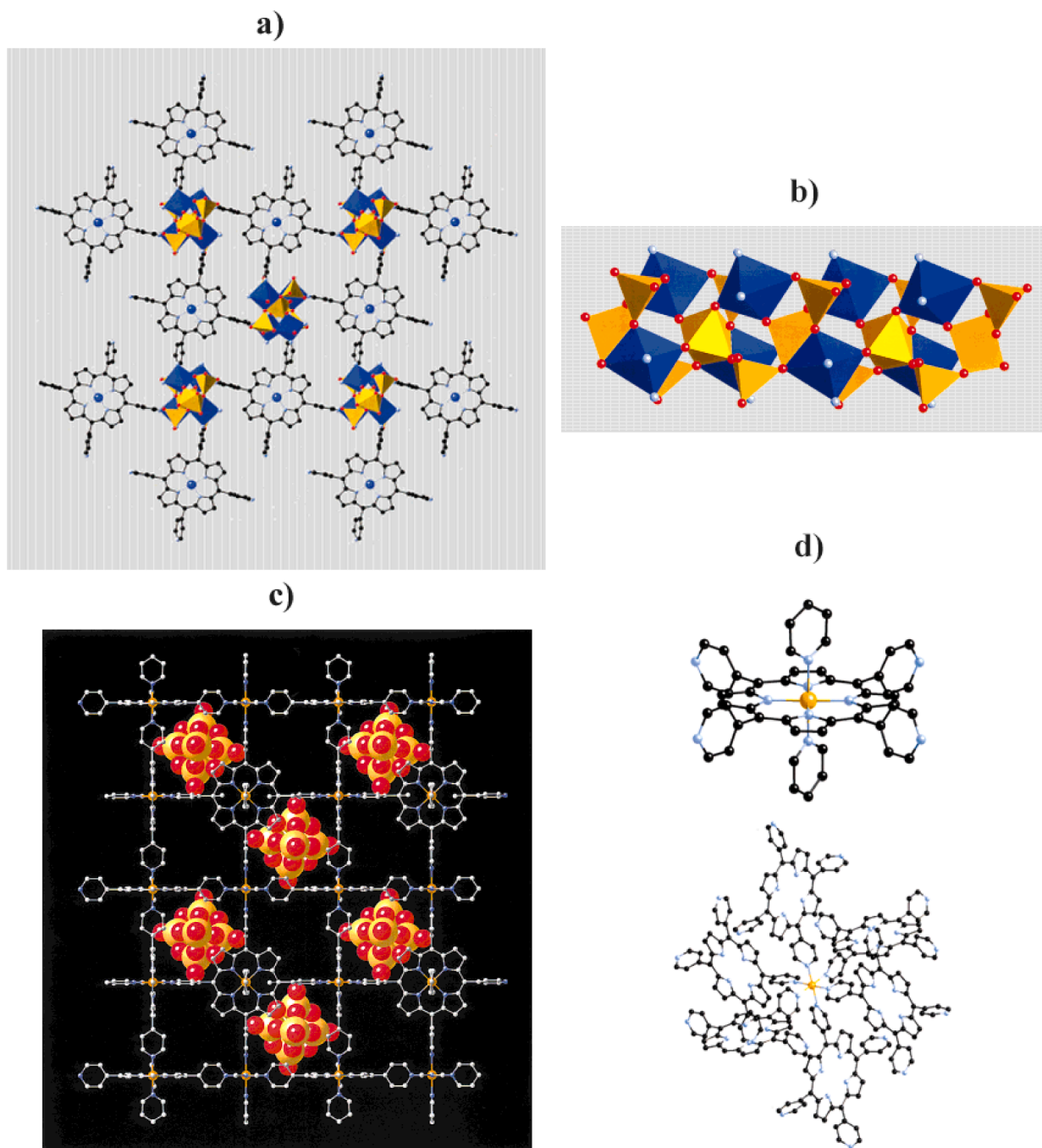
Fig. 15. Structural view of (a) [Cu(tpypor)Cu$_2$Mo$_3$O$_{11}$], (b) a polyhedral representation of the {Cu$_2$Mo$_3$O$_{11}$} chain of **5**, (c) structural view of [{Fe(tpypor)}$_3$Fe (Mo$_6$O$_{19}$)$_2$].xH$_2$O, and (d) views of the two Fe sites of **6**. In the former (**5**), the {Cu(tpypor)} building blocks are stacked in the ab plane, bridged by Cu$_2$Mo$_3$O$_{11}$ chains parallel to the porphyrin linkers along the axis c; and the latter (**6**) shows, viewed along the *c* direction, the scaffold formed from the [{Fe(tpypor)}$_3$Fe]$_n^{4n+}$ framework and combined with {Mo$_6$O$_{19}$}$^{2-}$ anions. Reproduced with permission from Ref [178]. Copyright 1999 Wiley-VCH.

[Bu$_4$N]$_3$[PW$_{12}$O$_{40}$]. However, when compared to POMMOF adsorbents (Table 6), the dye uptake capacity of MOF **7** is much less impressive; it seems that many factors such as structure (linear or non-linear), charge of dye (anionic or cationic), aperture size of the MOF and charge of the POM units can play crucial roles in dye capture [180]. The possible ways in which these factors might account for the wildly varying competence at dye scavenging are as follows. Most importantly, hydrophilic POM clusters regulate the pores and channels of the hydrophobic MOF framework, which in turn permit the entry and departure of the dye. Secondly, cationic dyes would have stronger interaction with the anionic POMs contained within the MOF network. The POM@MOFs

have thus exhibited a better ability to capture the cationic dyes like MB, CV, basic red 2 (BR) and RhB than the anionic ones such as solvent yellow 2 (SY) and methyl orange (MO). However, in some cases, steric hindrance of dye molecules and the adsorption sites on POM@MOFs leads to the adsorption of the dye molecules on the surface, which causes the bulk solid material to have a lower uptake capacity. Variation in the shapes of the dyes could also have a significant effect on adsorption capacity – the shape type (linear (MB) or planar (RhB, BR and CV) would also affect the capture. MB are also smaller than RhB and CV and can be adsorbed more conveniently [181].

An investigation of the sites where dye molecules were absorbed
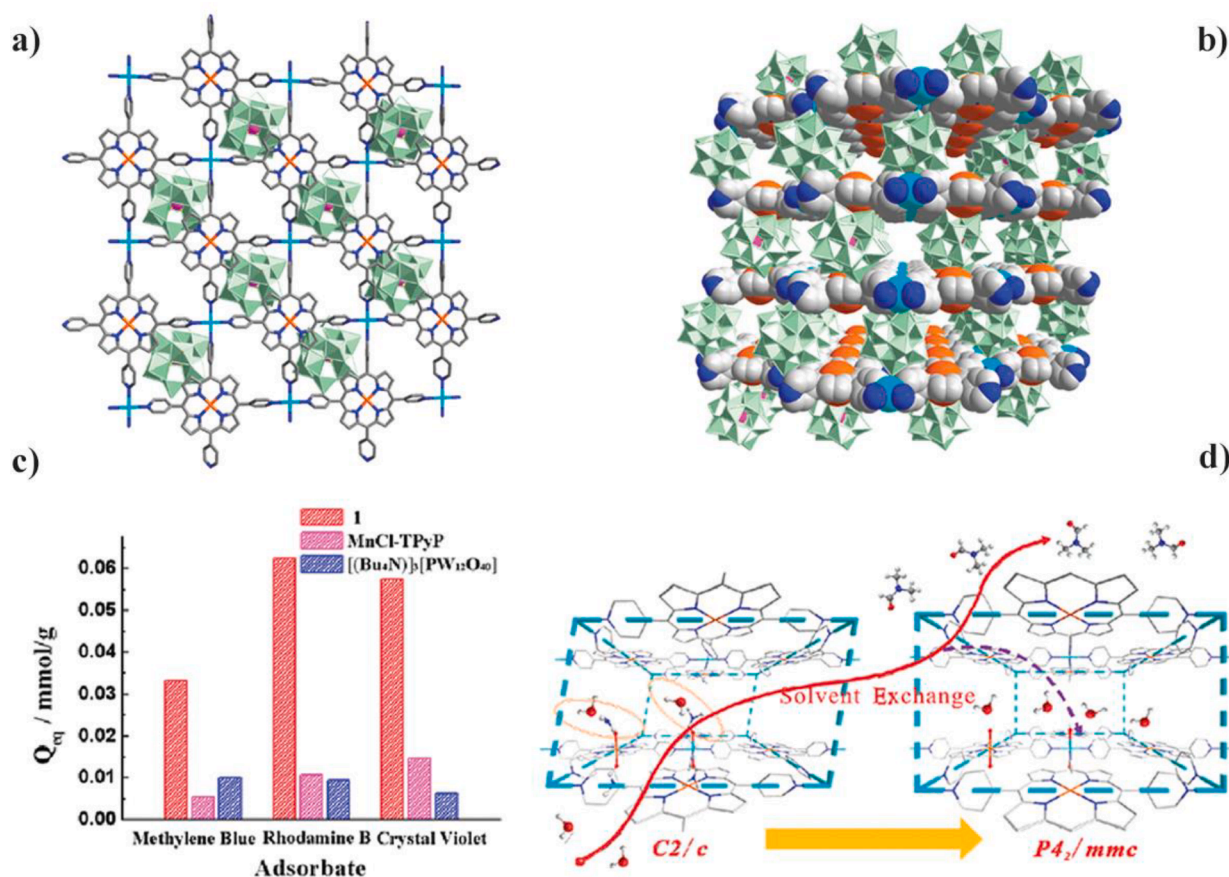
Fig. 16. (a) Depiction of an individual layer of {[Cd-(DMF)$_2$Mn^{III}(DMF)$_2$TPyP](PW$_{12}$O$_{40}$)}·2DMF·5H$_2$O viewed from the c direction. (b) Space-filling view of the as-made porous MOF constructed from [PW$_{12}$O$_{40}$]$^{3-}$ polyanions and Mn^{III}-porphyrinic frameworks, as viewed along the [110] direction. Atoms/clusters: Mn^{III}, orange; Cd, cyan; {WO$_6$}, green octahedra; P, purple; N, blue; C, gray. DMF molecules and H atoms have been removed for clarity. (c) Evaluation of the dye absorption competence of three different catalysts showing 7 (MOF; red), MnCl-TPyP (pink) and [Bu$_4$N]$_3$[PW$_{12}$O$_{40}$] (blue). (d) Single-to-single crystal alternation from 7 to 8 induced by solvent exchange. Reproduced with permission from Ref [179]. Copyright 2012 American Chemical Society. (For interpretation of the references to color in this figure legend, the reader is referred to the web version of this article.)

Table 6
Comparison of adsorption of various dyes on POMMOFs.

MOFs	Dye	Dye amount (mmol/g)	Refs
7	**MB, RhB and CV**	**0.033, 0.063 and 0.057**	[179]
HLJU 1–3	RhB and CV	10 and 0.093	[182]
PW$_{11}$V@MIL-101	MB	40	[183]
H$_6$P$_2$W$_{18}$O$_{62}$@MOF-5	MB	9	[184]
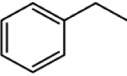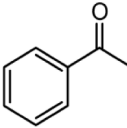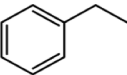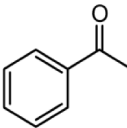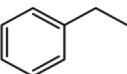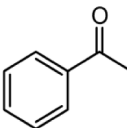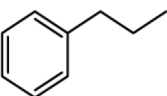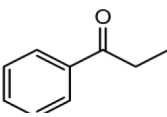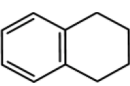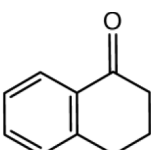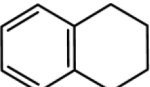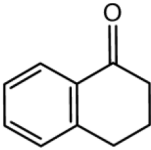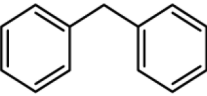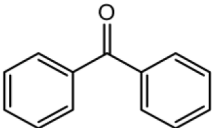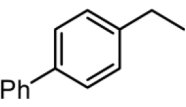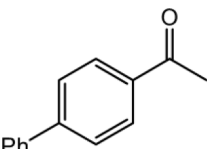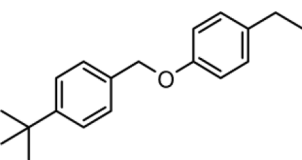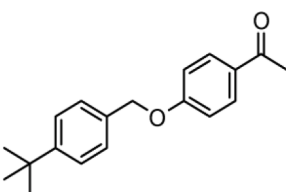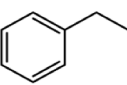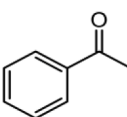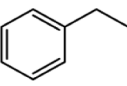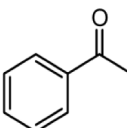
(either on the surface or inside the pores) was performed by X-ray crystallography (Fig. 16d). By immersing the as-reported MOF (**7**) in methylene blue at 50 °C overnight in aqueous media, the compound {[Cd-(H$_2$O)$_2$Mn^{III}(H$_2$O)$_2$TPyP](PW$_{12}$O$_{40}$)}·10H$_2$O (**8**) was obtained, with a very similar crystal structure to that of (**7**). However, they differed in appearance, and in the exchange of DMF for H$_2$O in the channels. In addition, the length of the c axis was lessened from 24.8738 (8) to 23.636(4) Å when the monoclinic *C2/c* space group of **7** was transformed to the tetragonal *P4$_2$/mmc* of **8** with a significant change in unit cell angles. It can be deduced that the dye molecules were absorbed on the outside of the MOF.

When used as an oxidizing catalyst (**7**) to convert alkylbenzenes to phenyl ketones, the MOF catalyst was able to efficiently oxidize propylbenzene and tetrahydronaphthalene to the related ketones with an incredible yield of 92.7 % (entry 1). By comparison to the less efficient MnCl-TPyP (73.6 % yield of acetophenone; entry 2) and [PW$_{12}$O$_{40}$]$^{3-}$ (no activity; entry 3), POM@MOF is seen to be massively superior to its

precursors (Table 7). Following 12 h of reaction, the mixture of compound **7** and *tert*-butylhydroperoxide ((TBHP); oxidant)) in H$_2$O was subjected to heat at 80 °C. Afterward, ethylbenzene (EB) and extra TBHP which were combined into the hot filtrate, was then kept heating at 80 °C for further 12 h. According to GC analysis, the mixture has shown its non-reactive behavior. The heterogeneous character of the catalyst **7** was proved by this experiment and it demonstrated the compound **7** could be recovered conveniently. It was thereafter utilized in consecutive cycles with mild decline in conversions (Table 7, entries 10 and 11). Conversely, when the reusable homogeneous Mn^{III}Cl-TPyP was used in lieu of catalyst **7,** the catalytic performance decreased drastically (Table 7, entry 12). The catalytic activity appears to be significantly influenced by steric hindrance, since larger substrate sizes result in lower reaction yields. Relatively small substrates (ethylbenzene) can in fact reach the Mn^{III} sites in the channel walls, enabling far higher catalytic ability than it would be possible with bigger substrates (4-ethyl-biphenyl and 1-(*tert*-butyl)-4-((4-ethylphenoxy)methyl)-benzene). Reactions can only take place at the external solid surfaces of **7** for the latter molecules (larger one) since they have trouble entering through the pore windows (Table 7, entries 4–9).
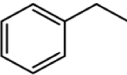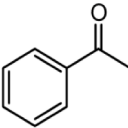
The catalytic efficiency of multiple previously-reported POMMOFs is provided in Table 8. The performance of compound **7** was significantly higher than most of those which were specifically used for oxidation of ethylbenzene to acetophenone (though not the highest so far, see entry 3; the substrate here is different from that of entry 1). Possibly the relevant factor leading to such catalytic efficiency is inherently related

Table 7

Phenyl ketone formation performed by selective alkylbenzene oxidation on diverse homo- and heterogeneous catalysts [179] [a].

Entry	Substrate	Product	Catalyst	Yield (%) [b]
1			**7**	**92.7**
2			MnCl-TPyP	73.6
3			$H_3PW_{12}O_{40}$	0
4			7	92
5			7	82.2
6			MnCl-TPyP	55.3
7			7	37
8			7	25.6
9			7	19.5
10			7	90.4 [c]
11			7	85.4 [d]
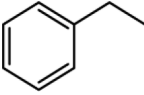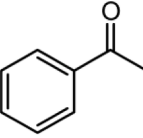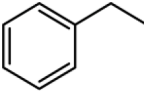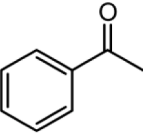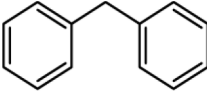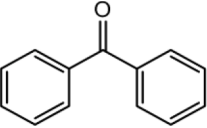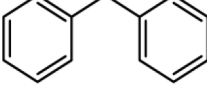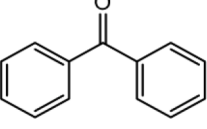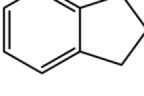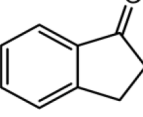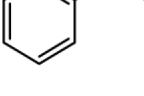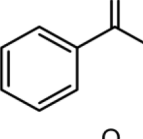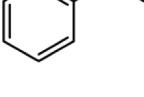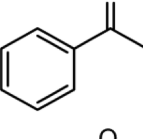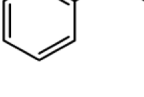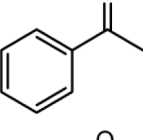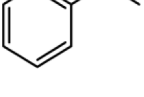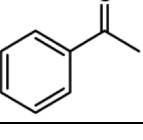
Table 7 (*continued*)

Entry	Substrate	Product	Catalyst	Yield (%)[b]
12			MnCl-TPyP	2.6[c]

[a]Conditions: Catalyst (0.01 mmol), alkylbenzene (0.1 mmol), and TBHP (0.5 mmol) were mixed in water (5 mL) and was kept stirring at 80 °C for 12 h. [b] According to GC analysis. [c] The yield made after second cycle. [d] The conversion gained after cycle six.

Table 8
Comparison of different POMMOF catalysts for oxidation of alkylbenzenes.

Entry	Substrate	Product	Catalyst	Conversion (%)	Refs
1			7	**92.7**	[179]
2			HENU-2	90.6	[185]
3			[Fe(H$_2$O)$_3$(dtb)][Fe(dtb)$_2$][HBW$_{12}$O$_{40}$]·12H$_2$O	99	[186]
4			FeW-PYDC	95.7	[187]
5			PW$_{12}$-Cu-pbba	81	[188]
6			[Cu$_2^I$Cu^{II}(bix)$_2$]{V$_4$O$_{12}$}	96	[189]
7			{[Cu$_2$(μ$_2$-H$_2$O)$_2$(4,4'-bpy)$_3$(SiW$_{12}$O$_{40}$)] (H$_2$O)$_6$}$_n$	79.5	[190]
8			{[Cu$_2$(4,4'-bipy)$_4$(H$_2$O)$_4$](SiW$_{12}$O$_{40}$)(H$_2$O)$_{18}$}$_n$	56.8	[191]
9			[H(C$_{10}$H$_{10}$N$_2$)Cu$_2$][PMo$_{12}$O$_{40}$]	69	[60]
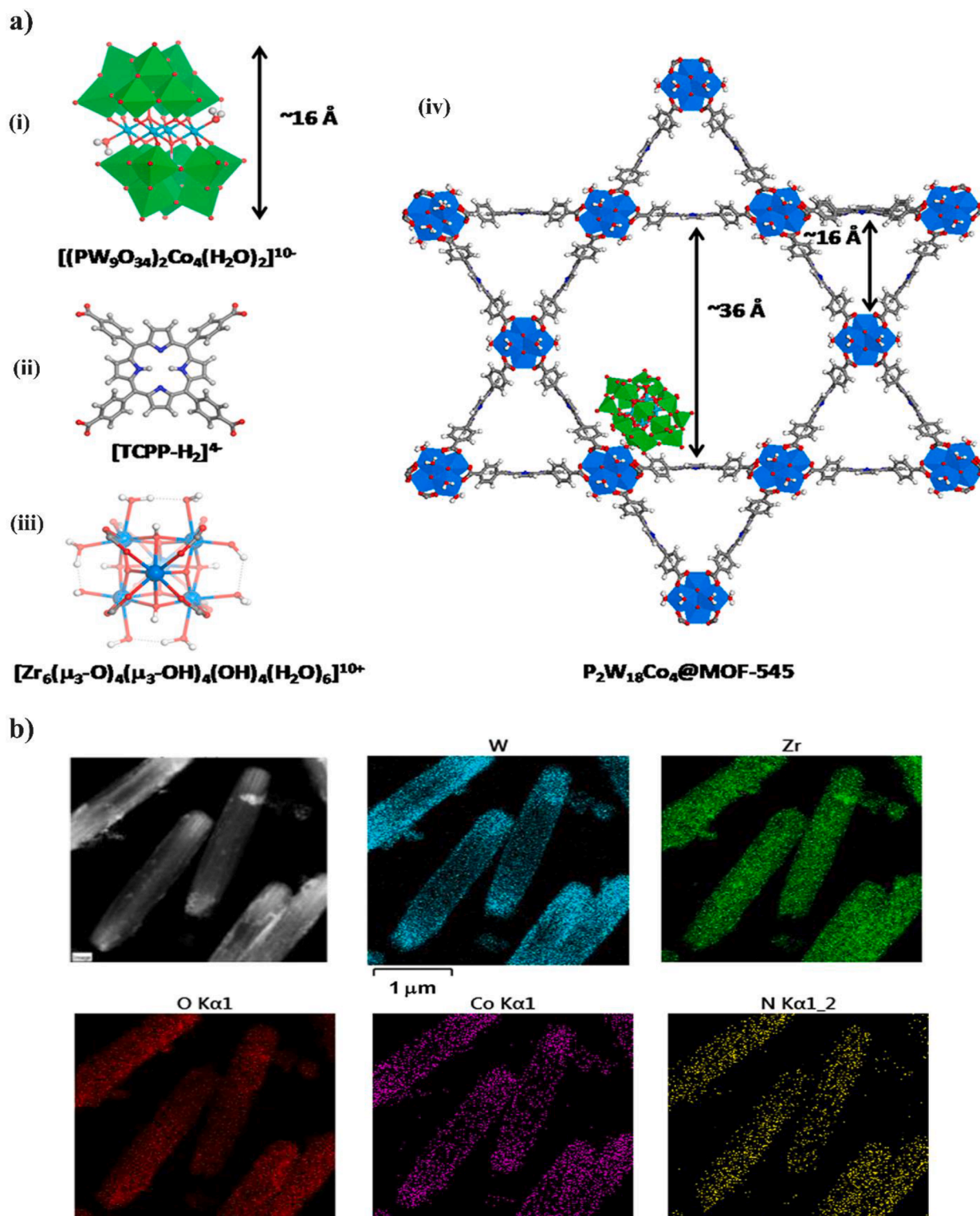
Fig. 17. (a) Representation of as-fabricated POM@MOF-545 composite: (i) the POM ($P_2W_{18}Co_4$) unit; (ii) H_6TCPP ligand; (iii) Zr coordination segment; and (iv) $P_2W_{18}Co_4$@PCN-222, To clarify, the POM position is obtained from computational studies. WO_6, green polyhedra; ZrO_8, blue spheres; Co, cyan spheres; O, red spheres; C, H, gray; N, dark blue. (b) localization of specific elements in POM@MOF-545 (POM (W and Co); and MOF (Zr, N, O)) as shown by STEM-HAAF images coupled with EDS mapping. Reproduced with permission from Ref [193]. Copyright 2018 American Chemical Society. (For interpretation of the references to color in this figure legend, the reader is referred to the web version of this article.)

to the type of the Keggin ion and the corresponding acidities [60,95]. Compound **7** contains a third-row transition metal center (W^{VI}), whose acidity and redox ability are likely to significantly exceed those of Mo^{VI}; thus, the Keggin clusters in **7** should be more acidic under similar

conditions. It might be expected that catalytic oxidation of ethylbenzene is improved by having more acidic POM segments, which would explain the higher catalytic ability of the POM@MOF discussed here. However, it is worth mentioning that straightforward comparisons with other
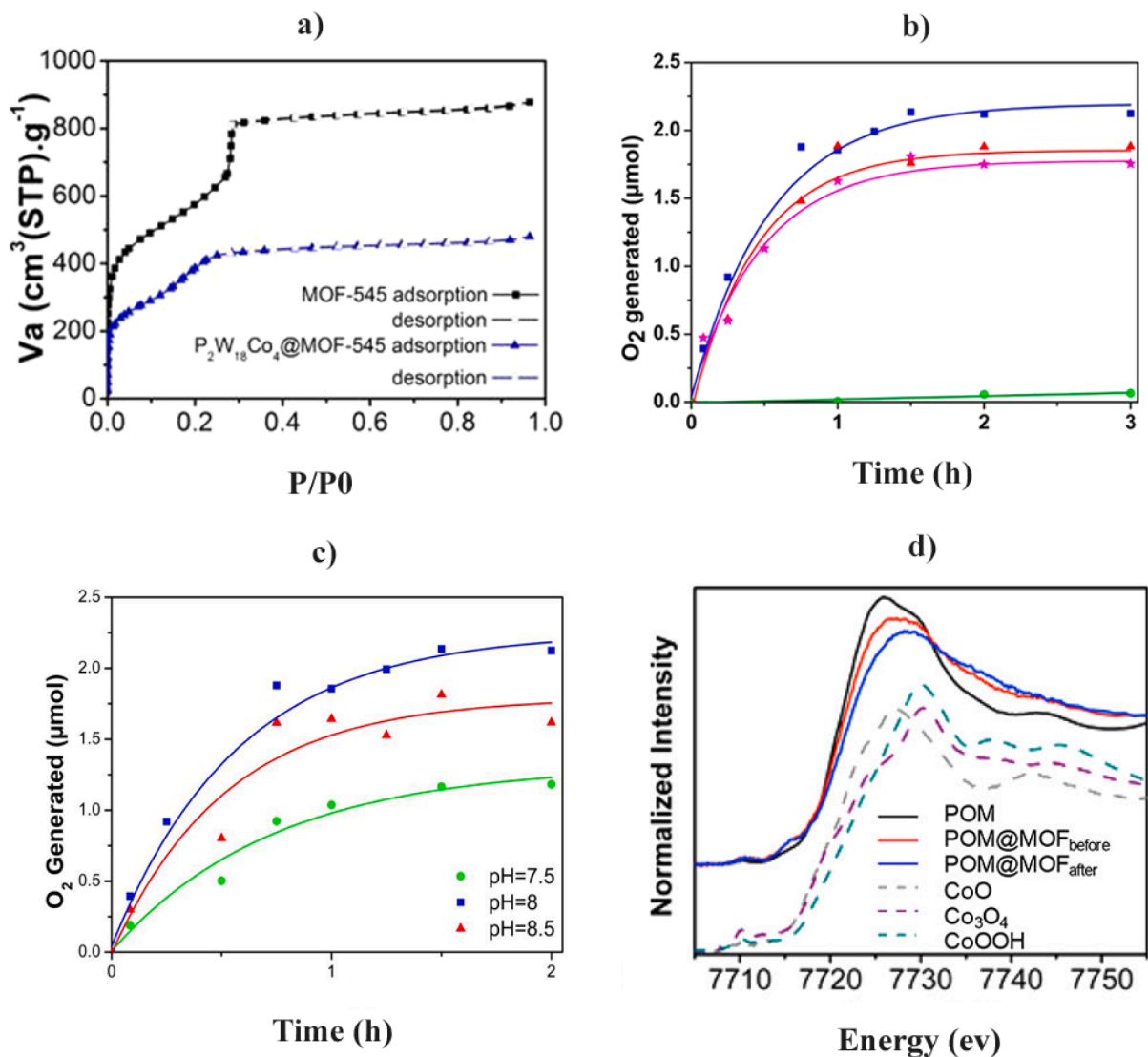
Fig. 18. (a) N_2 ads/des diagram, where black dots and blue triangles depict the adsorption/desorption of PCN-222 before and after POM inclusion, respectively; (b) O_2 generation kinetics diagram evaluated by GC using 0.5 mg of POM@PCN-222 (blue squares), POM@PCN-222 recovered once (red triangles) or for the third time (pink asterisks), and 131 µM TCPP-H_2 and 13 µM $P_2W_{18}Co_4$ (green dots) in 2 mL of 80 mM buffer solution of borate with 5 mM $Na_2S_2O_8$, (c) O_2 generation amount versus time of irradiation with visible-light using 0.5 mg of POM@PCN-222 and 5 mM $Na_2S_2O_8$ (10 µmol) in 2 mL of 80 mM borate buffer solution, at three different pH values, and (d) comparison of XANES spectra of POM and POM@MOF-545 with their relative metal oxides before and after catalysis. Reproduced with permission from Ref [193]. Copyright 2018 American Chemical Society. (For interpretation of the references to color in this figure legend, the reader is referred to the web version of this article.)

catalysts should only be made with careful consideration of the various ways that reaction conditions can vary: e.g., temperature, pressure, additives, co-catalysts, solvents, oxidative reagents and so forth.

3.3.3. $P_2W_{18}Co_4$@MOF-545 composite utilized for water oxidation

The brand-new $P_2W_{18}Co_4$@MOF-545 photocatalyst has three interesting traits – (i) light harvesting (ii) porosity and (iii) catalysis properties – all combined in one porous hybrid material. It is a peculiarly fascinating alternative to generate an ideal platform to be used effectively in water oxidation reaction. Fig. 17a depicts the structure of this new porphyrinic POM@MOF (2018), in which the photocatalytically-active guest $[(PW_9O_{34})_2Co_4(H_2O)_2]^{10-}$ (denoted as $P_2W_{18}Co_4$) is encapsulated in the cavities of the metal-free MOF-545 (also called PCN-222; PCN = Porous Coordination Network) [192,193]. The porphyrin ligand displays astonishingly high thermal/chemical stability and excellent catalytic efficiency, while the large hexagonal pores of the porphyrinic MOFs have shown themselves to be effective hosts for accommodating POMs in its interior.

$P_2W_{18}Co_4$@PCN-222 was manufactured as a dark purple powder by moderate impregnation of pre-obtained MOF by addition to the alkaline salt of $P_2W_{18}Co_4$ in aqueous solution. Rod-shaped crystals with a mean dimension of $2.4 \times 0.4 \times 0.4$ µm were characterized by STEM-HAADF (Scanning Transmission Electron Microscope-High-Angle Annular Dark-Field Imaging) images associated with EDS (Energy Dispersive Spectroscopy) mapping (Fig. 17b). It was revealed that the incidence of elements specific to the POM (W and Co) and to the MOF (Zr, N and O) were both spread over the entire framework. Yet, they also demonstrated that the POM segments had greater concentrations at both crystal rod boundaries, which is in line with the MOF channels being aligned across the rods' longest dimension when viewed along the c axis. In addition, Brunauer-Emmett-Teller (BET) surface area calculations, which were obtained by N_2 ads/des (Fig. 18a), clearly revealed the surface area declined significantly from 2080 to 1180 m^2g^{-1} for the unloaded MOF and the immobilized POM@PCN-222, respectively. This indicates the modification of the cavity distribution after $P_2W_{18}Co_4$ encapsulation. Also, the bulky POM (~16 Å) is properly localized in the
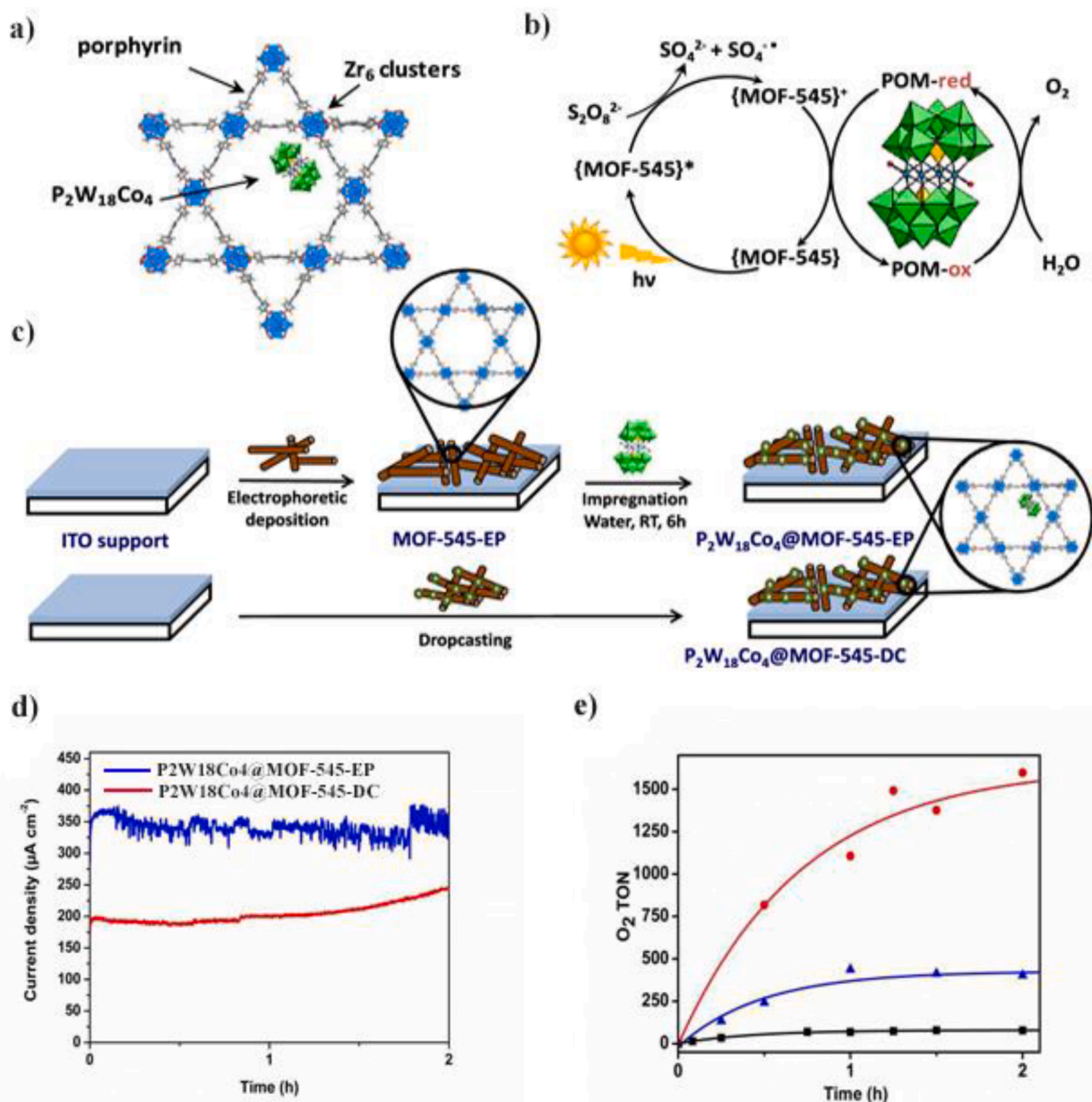
Fig. 19. (a) Graphical illustration of the $P_2W_{18}Co_4$@PCN-222 architecture; (b) suggested mechanism involved in OER water oxidation catalysis by $P_2W_{18}Co_4$@MOF-545 composite; (c) the synthetic methods employed to fabricate both $P_2W_{18}Co_4$@MOF-545-EP and $P_2W_{18}Co_4$@MOF-545-DC thin films; (d) diagram of current density vs. time during the CPE process at pH 8 buffer for $P_2W_{18}Co_4$@MOF-545-EP and -DC; and (e) TONs of O_2 generated during irradiation (5 mM $Na_2S_2O_8$ in 2 mL of 80 mM borate buffer solution, pH 8, $\lambda > 420$ nm, 280 W) for $P_2W_{18}Co_4$@MOF-545-EP (blue triangles), $P_2W_{18}Co_4$@MOF-545-DC (red dots) and 0.5 mg $P_2W_{18}Co_4$@MOF-545 powder in suspension (black squares). Reproduced with permission from Ref [194]. Copyright 2019 American Chemical Society. (For interpretation of the references to color in this figure legend, the reader is referred to the web version of this article.)

MOF's large hexagonal voids (roughly 36 Å). These results showed that the POMs are in fact found in the hexagonal channels, which are the biggest pores in the MOF. As a matter of fact, the peak ascribed to the triangle pores, however, did not decrease considerably, the peak corresponded to the hexagonal pores displayed a drop in intensity dramatically.

The visible-light oxygen evolution reaction (OER) in aqueous solution was performed with $P_2W_{18}Co_4$@MOF-545 together with the sacrificial electron acceptor $Na_2S_2O_8$ in borate buffer at pH 8. The mixture began to generate O_2 promptly on mixing, with a turnover frequency (TOF) = 40×10^{-3} s^{-1} measured over the first 15 min (Fig. 18b).

It was also observed that the optimal pH was around 8, as the photocatalytic competence at this pH was remarkably higher than at pH 7.5 and 8.5 (Fig. 18c). This may conceivably arise from too acidic media

causing the OER not to proceed effectively at pH < 8, and from a low chemical durability of the POM at pH > 8. Measurements obtained via TGA, XRD, EDS and GS analyses all univocally affirmed the composite to be more or less intact both before and after the reaction. However, there was indication of a slight reduction in TON by about 11 and < 5 % over the course of the first and third catalysis runs, respectively.

Following a three-hour photocatalytic experiment, the X-ray absorption near edge spectra (XANES) (Fig. 18d) which were documented on POM@MOF-545, revealed the major edge has shifted to higher energies (0.4 eV) when compared to their starting materials. It was ruled out a net shift in the cobalt oxidation state because the pre-edge region showed neither an intensity change nor the emergence of a new peak. It is preferable to explain this shift as the result of changes in the cobalt's immediate environment rather than to be considered as any significant
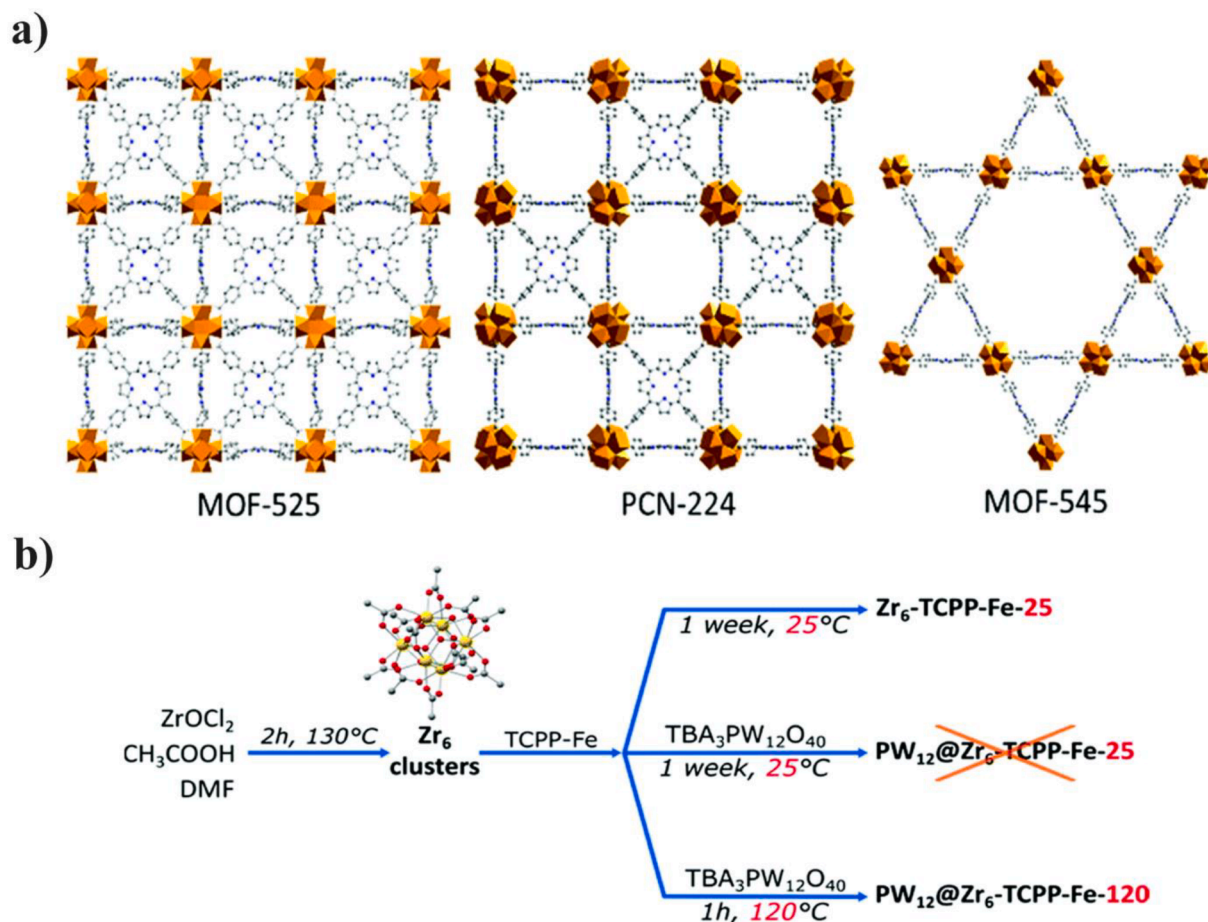
Fig. 20. (a) The three eminent Zr-based TCPP-MOFs which are discussed in this research: the two metal-free MOFs MOF-525 and PCN-224, and the large hexagonal pores of MOF-545 (PCN-222); and (b) schematic demonstration of the fabrication protocol which was exploited for Zr_6-TCPP-Fe and $PW_{12}@Zr_6$-TCPP-Fe, showing the direct role of $PW_{12}O_{40}^{3-}$ in the synthesis of the thermodynamically-favored MOF-545. Reproduced with permission from Ref [199]. Copyright 2020 Royal Society of Chemistry.

structural alterations, which represents that the stability of POM remained constant under various chemically induced OER.

3.3.4. Thin film of metal-free $P_2W_{18}Co_4@PCN-222$ as OER photocatalyst

Recently, a three-in-one photocatalyst network (light harvesting, porosity and catalysis) involving sandwich-like POM ($P_2W_{18}Co_4$) which was confined in the porphyrinic PCN-222 pores, was developed to provide a thin film substrate to catalyze light-driven OER (Fig. 19a) [194]. The incorporation of the POM inside the MOF was carried out by two frequently-used methods, *ex situ* drop casting (DC) and electrophoretic (EP). The reaction utilized pre-constructed POM@MOF deposited on indium tin oxide (ITO) surface as a transparently conductive support. The catalysts were assembled straightforwardly: the pre-manufactured POM@MOF was loaded on ITO by applying DC (named as $P_2W_{18}Co_4@PCN-222$-DC) and immersing ITO electrodes directly into MOF solution, followed by insemination with the POM, employing EP (also called $P_2W_{18}Co_4@PCN-222$-EP). In comparison with DC, the films prepared by EP were thicker and more uniform, so that the MOF particles were thinly scattered on the ITO exterior (Fig. 19c).

The electrocatalytic activity of the prepared thin films was measured (Fig. 19d), with a higher current density of around 350 μA cm^{-2} being obtained for $P_2W_{18}Co_4@MOF-545$-EP than for $P_2W_{18}Co_4@MOF-545$-DC (200 μA cm^{-2}). This confirmed the greater degree of homogeneity and higher density of POM@MOF-EP distributed on the film. After two hours of reaction, the faradic yields for both $P_2W_{18}Co_4@MOF-545$-DC and $P_2W_{18}Co_4@MOF-545$-EP were calculated nearly 100 %. The superior activity of DC thin films is indicated by the comparison of the

electrocatalytic efficacy of both catalysts: TOFs and TONs of $P_2W_{18}Co_4@MOF-545$-DC (310 $\times$ 10^{-3} s^{-1} and 2250) and $P_2W_{18}Co_4@$-MOF-545-EP (73 $\times$ 10^{-3} s^{-1} and 527) within 2-hour period of reaction exhibited the significantly better performances of $P_2W_{18}Co_4@MOF-545$-DC in comparison to $P_2W_{18}Co_4@MOF-545$-EP which can be explained by the fact that EP films have a greater thickness of around 20 μm, whilst DC films have crystalline sizes of approximately 1 μm. Therefore, as part of an insulating layer of materials in $P_2W_{18}Co_4@MOF-545$-EP, a significant fraction of POM@MOF crystallites on top of the film, that is, far from the conductive ITO support, might not be involved in the electrocatalysis. Given this, a larger number of catalytic POM active sites are accessible for $P_2W_{18}Co_4@MOF-545$-DC due to a higher sample dispersion. Fig. 19e depicts the O_2 amount generated by these two compounds during OER under photocatalytic investigations, which significantly outperformed the performances of similar formerly-reported composites – those displayed TONs of 20 ($P_2W_{18}Co_4@MIL-100(Fe)$) [195] and 27 (POM-free MIL-101(Fe)) [196], while the new systems attained values of 1600 and 403 for $P_2W_{18}Co_4@MOF-545$-DC and $P_2W_{18}Co_4@MOF-545$-EP, respectively, after 2 h. For similar previously-synthesized bulky POM@MOF compounds under the same reaction conditions, a TON of only 70 was obtained [197,198]. This experiment has clearly demonstrated that dispersions of light-susceptible porphyrinic POM@MOFs on a thin film surface can be used as fantastic hosts for developing heterogeneous photoactive electrocatalysts.

The reaction mechanism (Fig. 19b) can be described in these steps: (i) first, light is absorbed by the porphyrin, moving an electron to an excited state; (ii) this excited electron is transferred to POM in a 1-
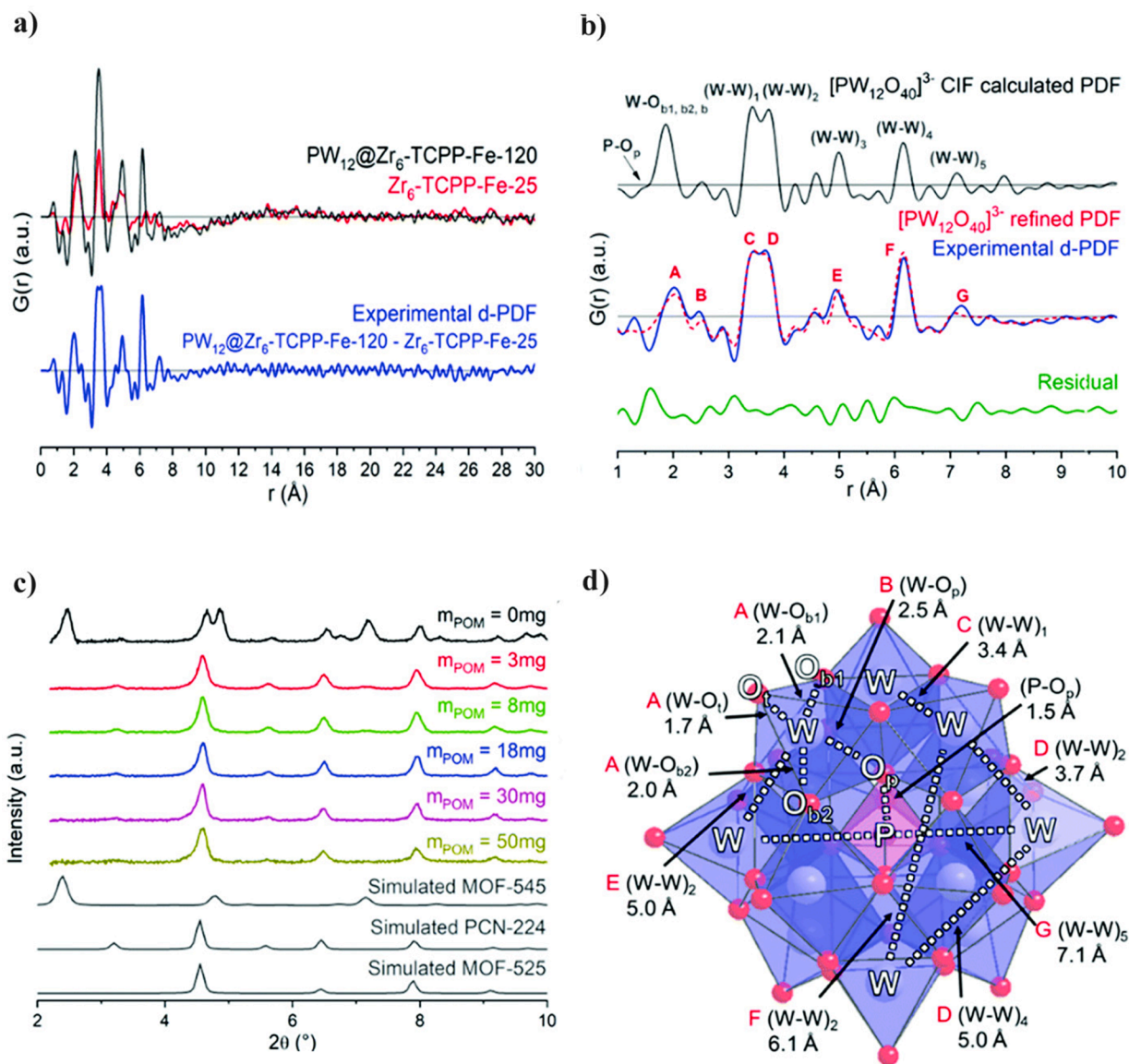
Fig. 21. (a) PDF spectra of $PW_{12}@Zr_6$-TCPP-Fe-120, Zr_6-TCPP-Fe-25 and the d-PDF obtained when combined with the impregnated PW_{12}. (b) Measured PDF profile of isolated PW_{12}, procured from crystallographic data, as well as measured d-PDF of PW_{12} in $PW_{12}@Zr_6$-TCPP-Fe-120. (c) PXRD spectra of the influence of a step-by-step rise in the PW_{12} amount for the synthesis of $PW_{12}@Zr_6$-TCPP-Fe-120. (d) Depiction of A-H peaks' labels and the associated refined distances in the POM cluster. Color code: WO_6, blue octahedra; PO_4, pink tetrahedron; O, red sphere; W, grey spheres; P, pink sphere. Reproduced with permission from Ref [199]. Copyright 2020 Royal Society of Chemistry. (For interpretation of the references to color in this figure legend, the reader is referred to the web version of this article.)

electron redox reaction; and finally (iii) water provides electrons to the porphyrin to make up for the loss, being oxidized to O_2 after losing 4 electrons.

3.3.5. Immobilized $PW_{12}O_{40}^{3-}$ as a structure-directing agent in the preparation of Zr-based MOFs

Experimental and theoretical procedures have together found evidence of the structure-directing role of Keggin-kind $PW_{12}O_{40}^{3-}$ (PW_{12}) polyoxometalate to be encapsulated inside Fe-metallated Zr-based porphyrinic MOFs voids (Fig. 20a). These three Zr_6-TCCP-based MOFs (MOF-525, PCN-224 and MOF-545) have proved to encompass enough large surface areas and spacious pores to enable the heterogenization of molecular catalysts like POM because of the enormous size of the TCPP linker in order to modify their catalytic properties at a large scale. It was found that the formation of MOF-525/PCN-224 is substantially kinetically favored over the thermodynamically-stable MOF-545 (PCN-222) phase. Fig. 20b depicts the synthetic routes in which high temperature

was applied in an *in situ* process to insert the POM. As the small apertures of MOF-525 and PCN-222 inhibit POM inclusion through impregnation, this yielded the thermodynamically-favored MOF-545 at higher temperature (third strategy in Fig. 20b; $PW_{12}@Zr_6$-TCCP-Fe-120) by addition of $(TBA)_3PW_{12}O_{40}$ as modulator after 1 h at 120 °C. PW_{12}, however, was not incorporated into the MOF via synthesis at RT (second strategy in Fig. 20b; $PW_{12}@Zr_6$-TCPP-Fe-25) [199].

Pair distribution function (PDF) measurements of the MOF (Fig. 21a and 21b) was undertaken due to the fact that it is difficult to determine the structure of the MOF-525/PCN-222 admixture from PXRD (powder x-ray diffraction) alone. First and most importantly, with a distinct peak at 3.1 Å and a rather intense peak at 5.1 Å, both of which are characteristics of Zr-connected TCPP linkers, it shares a lot of similarities with the spectrum of the MOF-525. Although, secondary characteristic peaks, such as a strong peak at 4.0 Å (linked to H_2O and –OH molecules in substitution of absent linkers) and a PDF profile that were analogous to PCN-224 (in the radial distance range of [5.5–7.5 Å]), the potential
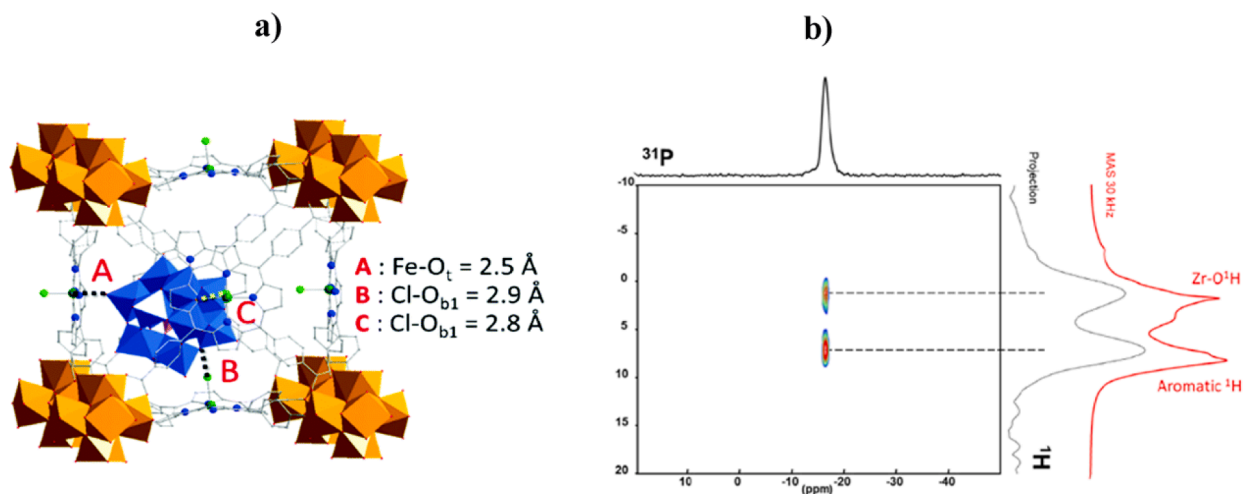
Fig. 22. (a) Most probable locating of the POM in the Zr-based porphyrinic MOF framework attained by DFT calculations. (b) 2D ^{31}P-^{1}H HETCOR Solid-State NMR CPMAS spectra of PW12@Zr6-TCPP-120 measured at 10 kHz of (achieving the HETCOR NMR data on the Fe-metallated MOF is not possible because of its paramagnetism). Reproduced with permission from Ref [199]. Copyright 2020 Royal Society of Chemistry.
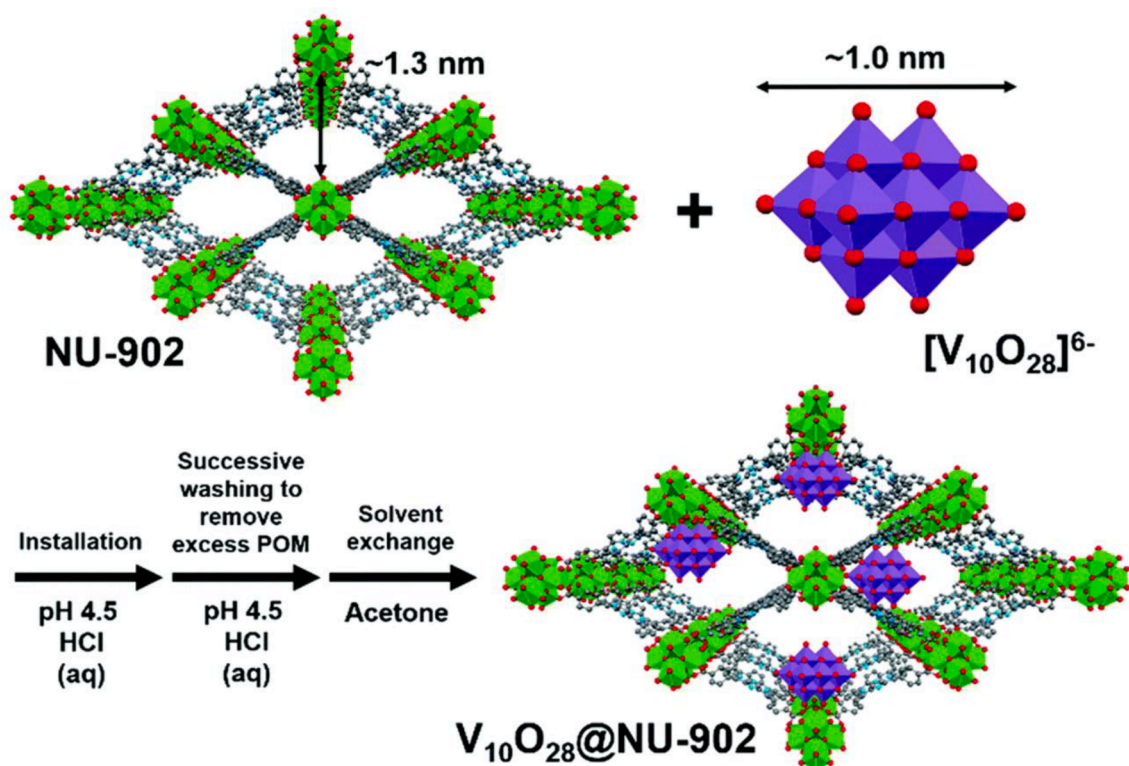
Fig. 23. Schematic illustration of the encapsulation of decavanadate inside Zr-based porphyrinic MOF, NU-902. Green: Zr; red: O; purple: V; grey: C; blue: N. Reproduced with permission from Ref [202]. Copyright 2020 Royal Society of Chemistry. (For interpretation of the references to color in this figure legend, the reader is referred to the web version of this article.)

existence of PCN-224 in Zr$_6$-TCPP-Fe-25 structure was pointed out. Subsequently, PDF data were utilized to examine the integrity of the incorporated POM structure in PW$_{12}$@Zr$_6$-TCCP-Fe-120. The differential PDF (d-PDF) of the accommodated PW$_{12}$ was derived by directly deducting the PDF of Zr$_6$-TCPP-Fe-25 from that of PW$_{12}$@Zr$_6$-TCCP-Fe-120 (Fig. 21a). Since, the d-PDF profile of the POM is the same as that of an isolated PW$_{12}$ (computed from crystallographic data) which is in the range of 1–10 Å (Fig. 21b), it is possible to precisely assign all PDF peaks specific for W-O and W-W distances, enabling the structure refinement for the PW$_{12}$ as seen in Fig. 21d. Altogether, the results obtained by PDF

showed that Zr$_6$-TCPP-Fe-25 is definitely a combination of MOF-525 and PCN-224. Furthermore, additional observations using PDF, the refined structure of PW$_{12}$ and the reasonably high level of refinement (R$_w$ = 29.3 %) proved the long-term stability of POM on incorporation in Zr$_6$-TCPP-Fe-120.

While maintaining all other synthetic parameters constant, the experimentation was concentrated on the effects of a gradual increase in the amount of PW$_{12}$ (added to the reaction medium of PW$_{12}$@Zr$_6$-TCPP-Fe-120) on the topologies of the resultant MOFs. In the absence of PW$_{12}$, however, a combination of the kinetic, MOF-525(Fe)/PCN-224(Fe), and
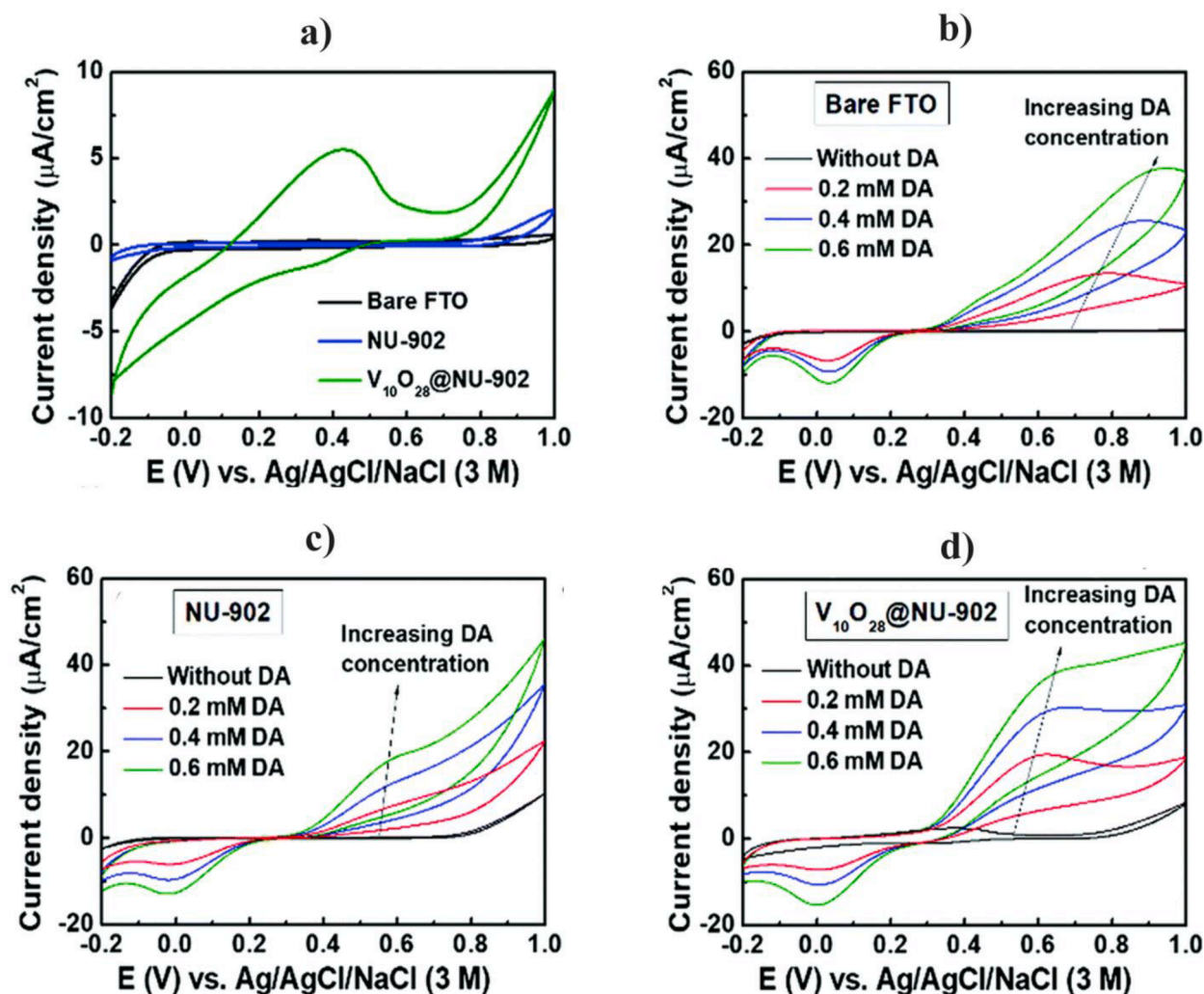
Fig. 24. Cyclic voltametric diagrams of (a) the empty FTO thin film, and the deposited ones with NU-902 and $V_{10}O_{28}$@NU-902; and (b) vacant FTO, (c) NU-902 thin film substrate, and (d) $V_{10}O_{28}$@NU-902, all evaluated in the presence of different concentrations of DA. All CV curves were assessed at a scan rate of 10 mV/s with 0.05 M MOPS/NaOH aqueous solutions (pH = 4.5) as the electrolytes. Reproduced with permission from Ref [202]. Copyright 2020 Royal Society of Chemistry.

thermodynamic, PCN-222, compounds were obtained. Remarkably, however, the addition of a relatively little quantity of PW_{12} overwhelmed the production of the thermodynamic phase (MOF-545(Fe)) (Fig. 21c, red); suggesting that PW_{12} has a significant structure-directing impact when synthesis was performed at higher temperature. The PXRD diagrams of the PW_{12}@Zr6-TCPP-Fe-120 composites, which are corresponded to PCN-224(Fe) or to the mixture of MOF-525(Fe)/PCN-224 (Fe), are all identical when obtained for greater PW_{12} amounts.

Density functional theory (DFT) calculations in combination with solid-state NMR (nuclear magnetic resonance) studies were in accordance with the temperature-topology relationship of a host–guest interaction. The DFT calculations indicated a non-centered position of the POM inside the cubic pore of the MOF, pointing toward the center where the Zr-oxocluster node are located (Fig. 22a). These findings depict a strong connection with the 2D $^{31}P\{^1H\}$ magic angle spinning nuclear magnetic resonance (MAS NMR) spectroscopy (Fig. 22b), which demonstrates how close the POMs are to the inorganic nodes spatially. Totally, the data analyses gained for POMMOF connections via DFT calculations aligned with solid-state NMR measurements, have further simplified the information attained by PDF study.

3.3.6. $V_{10}O_{28}$@NU-902 as a heterogeneous electrocatalyst for dopamine oxidation

There are chemically robust and highly porous zirconium-based

MOFs which are well-known for their chemical durability in aqueous conditions, [200,201] and which integrate redox-active segments – porphyrin linker and POM. These can be used as redox-hopping electrocatalysts to transmit charge to the porphyrinic MOF in order to oxidize dopamine (DA) effectually. The electrostatic interaction taking place between POM and *hexa*-Zr-oxo moieties, and also the suitable size of decavanadates for insertion into the MOF, have made it possible to perform post-synthetic impregnation of a redox-active sodium decavanadate (a vanadium-based POM, $Na_6V_{10}O_{28}$) into the one-dimensional pores of NU-902 (NU; Northwestern University) ($V_{10}O_{28}$@NU-902) (Fig. 23) [202]. Thereafter, thin films of NU-902 and $V_{10}O_{28}$@NU-902, which were loaded onto fluorine-doped tin oxide (FTO) substrates, demonstrated an ability to serve as heterogeneous catalysts for electrocatalytic oxidation of DA in aqueous solution.

The solution contained 3-(N-morpholino)propanesulfonic acid (MOPS) and NaOH at pH = 4.5. Surprisingly, even when applying potentials significantly less than + 0.8 V vs. Ag/AgCl/NaCl (3 M), neither the empty layer FTO nor the deposited NU-902 thin film substrates showed significant electrochemical activity. It is expected that however the porphyrin ligands in NU-902 displayed redox hopping abilities, the charge-transmission did not happen for porphyrin-based materials with the potential lower than + 0.8 V vs. Ag/AgCl/NaCl (3 M). It can facilitate the charge-transfer when the porphyrin linkers are oxidized by the $[V_{10}^{5+}O_{28}]^{6-}$ moieties and the onset current is near + 0.8 V (Fig. 24a). The
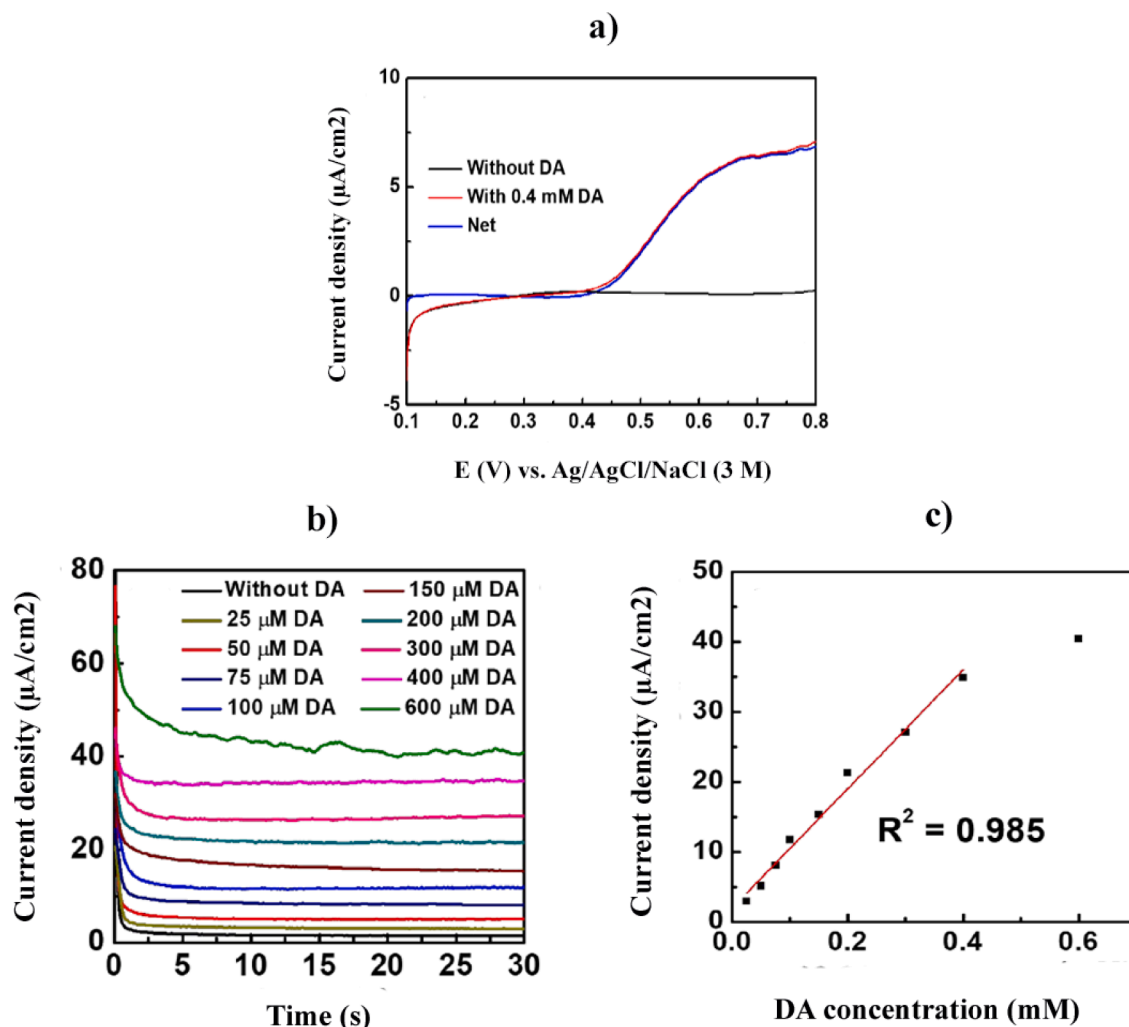
Fig. 25. (a) LSV plots of the $V_{10}O_{28}$@NU-902 thin film observed in 0.05 M MOPS/NaOH aqueous solutions (pH = 4.5) with and without 0.4 mM of DA. The net response between two LSV curves is also depicted. (b) Amperometric curves of $V_{10}O_{28}$@NU-902 thin films at an employed potential of + 0.7 V vs. Ag/AgCl/NaCl (3 M) obtained in 0.05 M MOPS/NaOH aqueous solutions (pH = 4.5) with several DA concentrations. (c) diagram of current response versus the DA concentration. Reproduced with permission from Ref [202]. Copyright 2020 Royal Society of Chemistry.

Table 9
The DA sensing factors of $V_{10}O_{28}$@NU-902 in comparison with previously-reported MOF sensors.

Compound	Procedure	Linear range (µM)	LOD (µM)	Refs
$V_{10}O_{28}$@NU-902	**AMPa**	**24–400**	**2.1**	[202]
POMOFs/rGO	CV[b]/DPV[c]	1–200	4.7	[203]
HKUST-1	DPV	0.5–100	0.11	[204]
N-doped Cu-based MOF	AMP	0.0005–46.81	0.00015	[205]
$PMo_{10}V_2$@MIL-101	CV/SWV[d]	1–250	1.3	[206]
POM-γCD MOF/LSGE	DPV	0.050—1000	0.010	[207]
Au@ZIF-8	DPV	0.5–50	8.6	[208]

[a]AMP = amperometry; [b] CV = cyclic voltammetry; [c] DPV = differential pulse voltammetry; [d] SWV = square-wave voltammetry.

$V_{10}O_{28}$@NU-902 composite did in fact display redox hopping competence between POM units on investigation using cyclic voltammetry (CV), the results of which (using a voltage range that includes + 0.8 V vs. Ag/AgCl/NaCl (3 M)) are shown in Fig. 24a. In addition, Fig. 24b-d depicts the CV diagrams of the free FTO substrate, NU-902 and $V_{10}O_{28}$@NU-902 thin films, respectively, all recorded at various DA concentrations. The CV curves of the bare FTO (Fig. 24b) showed anodic peaks for DA oxidation at about + 0.8 V vs. Ag/AgCl/NaCl (3 M). When applying NU-902 thin film as electrocatalyst, the peaks for the DA oxidation moved to around + 0.6 V (Fig. 24c) even though the changes for increase in current density between each DA concentration got negligibly less than that observed for the bare FTO. In the presence of the $V_{10}O_{28}$@NU-902 substrate, increasing the DA concentration leads to considerably larger and more linear current densities around + 0.6 V than measured for the NU-902 thin film and bare FTO (+0.8 V). This indicates that the $V_{10}O_{28}$@NU-902 thin film electrocatalyst can oxidize DA to dopamine-o-quinone (DAQ) much more efficiently (Fig. 24d).

It was reasoned that such a heterogeneous electrocatalyst could be utilized for the detection of amperometric DA owing to fact that the CV curves regarding the $V_{10}O_{28}$@NU-902 composite displayed a linear increment in current density when DA concentration increased. Fig. 25a revealed that the net current response consisted of a discrete plateau at around + 0.7 V vs. Ag/AgCl/NaCl (3 M). Moreover, it indicates with applying such voltage, the DA electrocatalytic oxidation may happen inside the diffusion-controlled area.

As indicated in Fig. 25b, $V_{10}O_{28}$@NU-902 thin films in 0.05 M MOPS/NaOH aqueous solutions (pH = 4.5) and with an applied potential of + 0.7 V vs. Ag/AgCl/NaCl (3 M), were carried out for amperometric sensing invesrigations. For each amperometric curve, the current response was recorded at 30 s as exhibited in Fig. 25c which
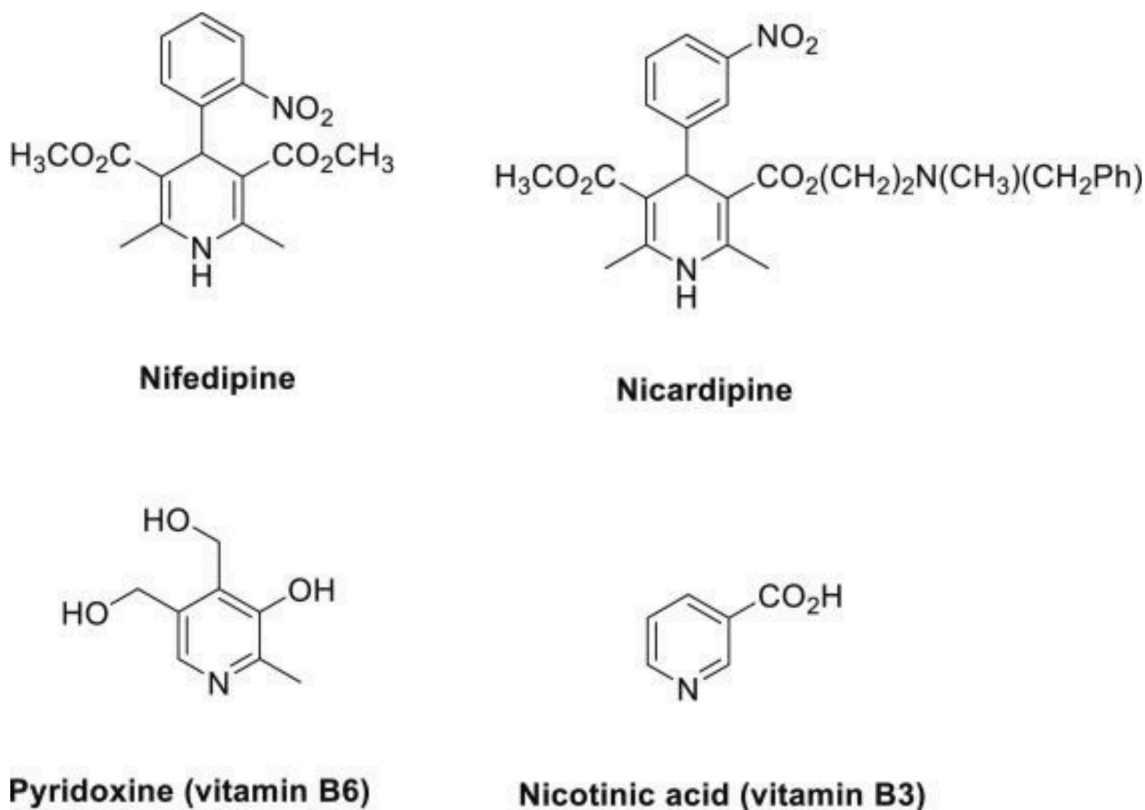
Scheme 13. Some of the N-heterocycles (pyridine-isolated organic compounds) involving Nifedipine, Nicardipine, Pyridoxine (vitamin B6) and Nicotinic acid (vitamin B3). Reproduced with permission from Ref [209]. Copyright 2022 Elsevier.
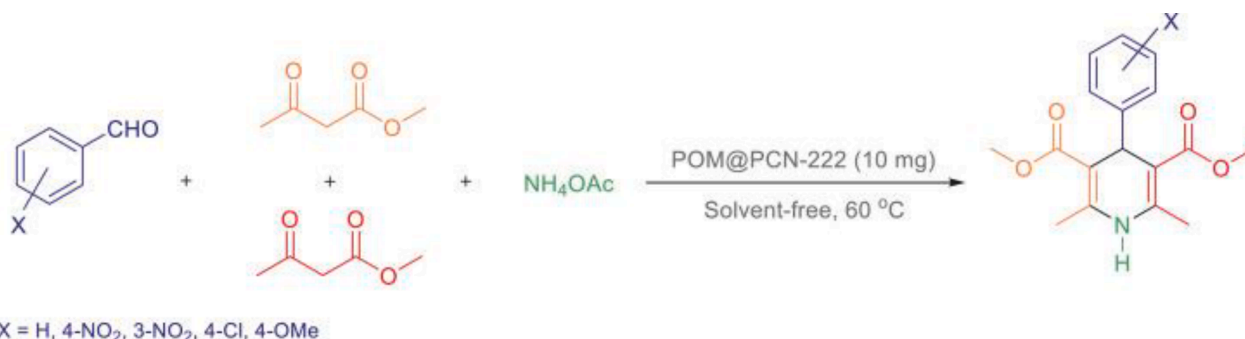
Scheme 14. Schematic representation of the multicomponent reaction among aldehydes, methyl acetoacetate and ammonium acetate for N-heterocycles production derived under visible-light illumination. Reproduced with permission from Ref [209]. Copyright 2022 Elsevier.

displays the plot of the current response versus the concentration of DA. To estimate the sensitivity and linear range of the sensor, Equation (1) was used to determine limit of detection (LOD) with respect to a noise-to-signal ratio, in which N represents the noise in current density taken out from the amperometric curve before DA addition.

$$LOD = \frac{3 \times N}{Sensitivity} \tag{1}$$

The amperometric DA sensor assembled from $V_{10}O_{28}$@NU-902 thin film, achieved considerable linear range (25–400 µM), sensitivity (85 µA/mM-cm^2) and LOD (2.1 µM) upon employing the potential of $+0.7$ V vs. Ag/AgCl/NaCl (3 M) (Fig. 25c).

Table 9 lists the electrocatalytic capability of several POMMOFs to oxidize DA to DAQ. The data acquired for $V_{10}O_{28}$@NU-902 are similar to those of previously reported DA sensors. However, nearly all previous reports employed glassy carbon electrodes (GCE) or other kinds of

substrates are costly, rigid, and inappropriate for point-of-care (PoC) analytical utilizations. The authors of the work on $V_{10}O_{28}$@NU-902 exploited ITO, which is much less expensive and more accessible, thus meeting the main prerequisite for PoC use. All the observations demonstrate that, in comparison to other sensors, the $V_{10}O_{28}$@NU-902-based sensor exhibited modest and more meaningful linear range and LOD.

3.3.7. POM@Zr-porphyrinic MOF mediator for photocatalytic creation of N-heterocycles

The recent solvothermal preparation of $H_3PW_{12}O_{40}$@MOF-545 was accomplished using porous metal-free PCN-222 as a starting material. After impregnation with the POM, it was used as a support to assemble the desired composites via a simple PSM technique at room temperature. The resulting compound was then used to catalyze the one-pot production of N-heterocycles (pyridine-isolated organic compounds). This is the first reported application of such hybrid materials as effective

Table 10

Results of varied reaction conditions for multicomponent synthesis of N-heterocycles [209] [a].

Entry	Catalyst	Solvent or solvent-free	T (C)	Time (h)	Yield (%)[b]	TON/TOF (h^{-1})[c]
1	–	solvent-free	r.t.	24	–	–
2	POM@PCN-222[d]	solvent-free	r.t.	24	27	18/0.75
3	POM@PCN-222	solvent-free	40	7.5	75	47.77/6.37
4	POM@PCN-222	solvent-free	60	5	90	57.32/11.46
5	POM@PCN-222	solvent-free	80	5	89	56.69/11.33
6	POM@PCN-222[e]	solvent-free	60	7	78	78/11.14
7	POM@PCN-222[f]	solvent-free	60	5	91	37.92/7.58
8	POM@PCN-222	EtOH	60	7	70	44.58/6.37
9	POM@PCN-222	EtOH	Reflux	7	77	49.04/7.01
10	POM@PCN-222	CH$_3$CN	60	10	70	44.58/4.46
11	POM@PCN-222	CH$_3$CN	Reflux	10	75	47.77/4.77
12	POM@PCN-222	CH$_3$CN/H$_2$O	Reflux	10	76	48.41/4.84
13	POM@PCN-222	H$_2$O	60	10	58	35.94/3.69
14	PCN-222	solvent-free	60	8	60	38.22/4.78
15	TCPP	solvent-free	60	5	16	10.19/2.04
16	ZrOCl$_2$·8H$_2$O	solvent-free	60	5	47	29.94/5.99
17	POM	solvent-free	60	5	71	45.22/9.04
18	PCN-222 + POM[g]	solvent-free	60	5	80	50.95/10.19

[a] Reaction conditions: benzaldehyde (1 mmol), methyl acetoacetate (2 mmol), ammonium acetate (1 mmol), and catalyst (~1.6 mol%) done under solvent or solvent-free conditions.

[b] Yields denote to isolated and the most purified products.

[c] TON (turnover number) = product (mmol)/catalyst (mmol), and TOF (turnover frequency) = TON/time (h).

[d] POM@PCN-222 (10 mg, equivalent to 0.0106 mmol of Zr(IV), 0.0035 mmol of TCPP, and 0.0016 mmol of POM as active sites, total active sites = 0.0157 mmol).

[e] 1 mol%. [f] 2.4 mol%. [g] PCN-222 (1.41 mol%) and POM (0.16 mol%).

catalysts for the photochemical fabrication of well-known N-heterocycles – target systems including Nifedipine, Nicardipine, Pyridoxine (vitamin B6) and Nicotinic acid (vitamin B3) (Scheme 13), derived from the reaction components of aldehydes, methyl acetoacetate and ammonium acetate (Scheme 14) [209].

Table 10 lists the results for a variety of multicomponent reaction conditions upon visible-light illumination (including different solvents), for the POM@MOF-545 system as well as for some other catalysts. From all of the assessed conditions, the best results were seen for a short (5 h) solvent-free reaction using POM@MOF-545 (entry 4), which had a very high yield (90 %) combined with the highest values for TON and TOF (57.32 and 11.46 h^{-1}, respectively). In comparison, unfunctionalized MOF-545 (PCN-222) (entry 14) afforded only 60 % yield after the reaction was performed for a longer time (8 h), and the TON/TOF values were only 38.22/4.78 h^{-1}. The respective catalytic performance of MOF-545 might be attributed to the presence of Zr$_6$-node (Lewis acidic sites) and porphyrin linkers (Lewis basic sites) of MOF-545. Besides, control assessments were fulfilled with TCPP (as MOF linker) and ZrOCl$_2$·8H$_2$O (as Zr-node precursor) fragments, and noticeably affirmed their effectual functions in the catalysis (entries 15 and 16).

Nevertheless, conversions and TON/TOF were considerably lessened in comparison with those attained for POM@MOF-545. The POM by itself (entry 17), under the same optimized reaction conditions, did somewhat better, with a yield of 71 % after 5 h with TON of 45.22 and TOF of 9.04 h^{-1}.

MOF-545 as catalyst (equimolar in Zr and TCPP in POM@MOF-545) was physically combined with POM (equimolar in POM to POM@MOF-545) and evaluated in order to investigate the functions of the support and active sites (entry 18). The production conversion earned 80 % (TON/TOF = 50.95/10.19 h^{-1}), which was relatively less than that observed for POM@ MOF-545 (entry 4; conversion 90 % and TON/TOF = 57.32/11.46 h^{-1}). The observations also discovered that the POM@MOF-545, Zr-nodes and TCPP linkers play their roles as catalytically active sites in the reaction. Meanwhile, the synergistic functions among porphyrinic MOF, POM and the employment of the 3D ordered porous active sites within MOF structure have boosted the catalytic efficacy of POM@MOF-545, which could be correlated to the PW$_{12}$ insertion inside porphyrinc MOF framework.

However, as far as we are aware, the class of POMMOFs has not displayed much ability to heterogeneously catalyze a multicomponent reaction; only one example of such ability is given in the literature, which we will now consider. A conceivable path to prepare pyridines is possible through their relevant 1,4-dihydropyridines oxidation. Typically, β-keto esters, aldehydes and ammonia reagents react *in situ* together to synthesize Hantzsch 1,4-dihydropyridines [210,211]. In nature, 1,4-dihydropyridines derivatives are formed by cytochrome *P*-450 enzymes [212,213]. Unfortunately, when performed technologically, these procedures possess major downsides, such as the utilization of expensive oxidizing agents/catalysts, the need for additives, and extreme reaction conditions (temp/pressure). Although a great many protocols [214–220] have been put into action to synthesize pyridine derivatives, the fabrication of pyridines under moderate conditions via oxidation of 1,4-dihydropyridines in a one-pot reaction media is still challenging – but has been accomplished.

Fig. 26 depicts the proposed mechanism for the catalytic/photocatalytic N-heterocycle synthesis using H$_3$PW$_{12}$O$_{40}$@PCN-222 as a catalyst. Starting from POM@PCN-222 (Fig. 26a) which possesses porphyrin linkers (as photosensitizer) [221] and Lewis acids (POM and Zr clusters) [45,222], it stimulates the activation of corresponding aldehyde to be added to enol form of methyl acetoacetate (**1**) through nucleophilic attack in a Knoevenagel reaction so as to produce intermediate (**2**). Simultaneously, the enamine intermediate (**3**) is made from the attack of ammonia, that is formed from ammonium acetate *In situ*, to the second methyl acetoacetate which is also activated by POM@PCN-222. Then, the intermediate (**4**) is constituted via the reaction of enamine (**3**) with the activated intermediate (**2**) in Michael addition. Next, cyclization and condensation reactions bring about the formation of dihydropyridine (**5**). In the further step (Fig. 26b), radical cation (**6**) and radical anion POM@PCN-222$^{•-}$ are manufactured upon visible light illumination on POM@PCN-222, in which through a single electron transfer (SET) process, the excited species POM@PCN-222* is shaped and reductively quenched by (**5**). Electron paramagnetic resonance (EPR) was a useful tool in monitoring the reaction, as it was able to detect the superoxide radical anion (O$_2^{•-}$) species (Fig. 27), which was the agent responsible for abstracting the proton from (**6**) after the latter was formed from (**5**) during the catalytic process. O$_2^{•-}$ is believed to have been generated earlier by transferring an electron to O$_2$ from POM@PCN-222$^{•-}$, and subsequently grabbed by 5,5-dimethyl-1-pyrroline *N*-Oxide (DMPO) (acting as a radical scavenger). This was then followed by creation of (**7**) by removing an electron, in order to provide the final, desired pyridine derivative product (Fig. 26b) [223].

Notably, coupling the photosynthesizing and photothermal abilities of porphyrin spacers (particularly TCPP) with the Lewis-acidic properties of the POM and Zr$_6$-SBU inorganic moieties will promote novel, synergistically superior heterogeneous catalysts, making the procedure easier and more eco-friendly. In this experiment, it led to synthesis of

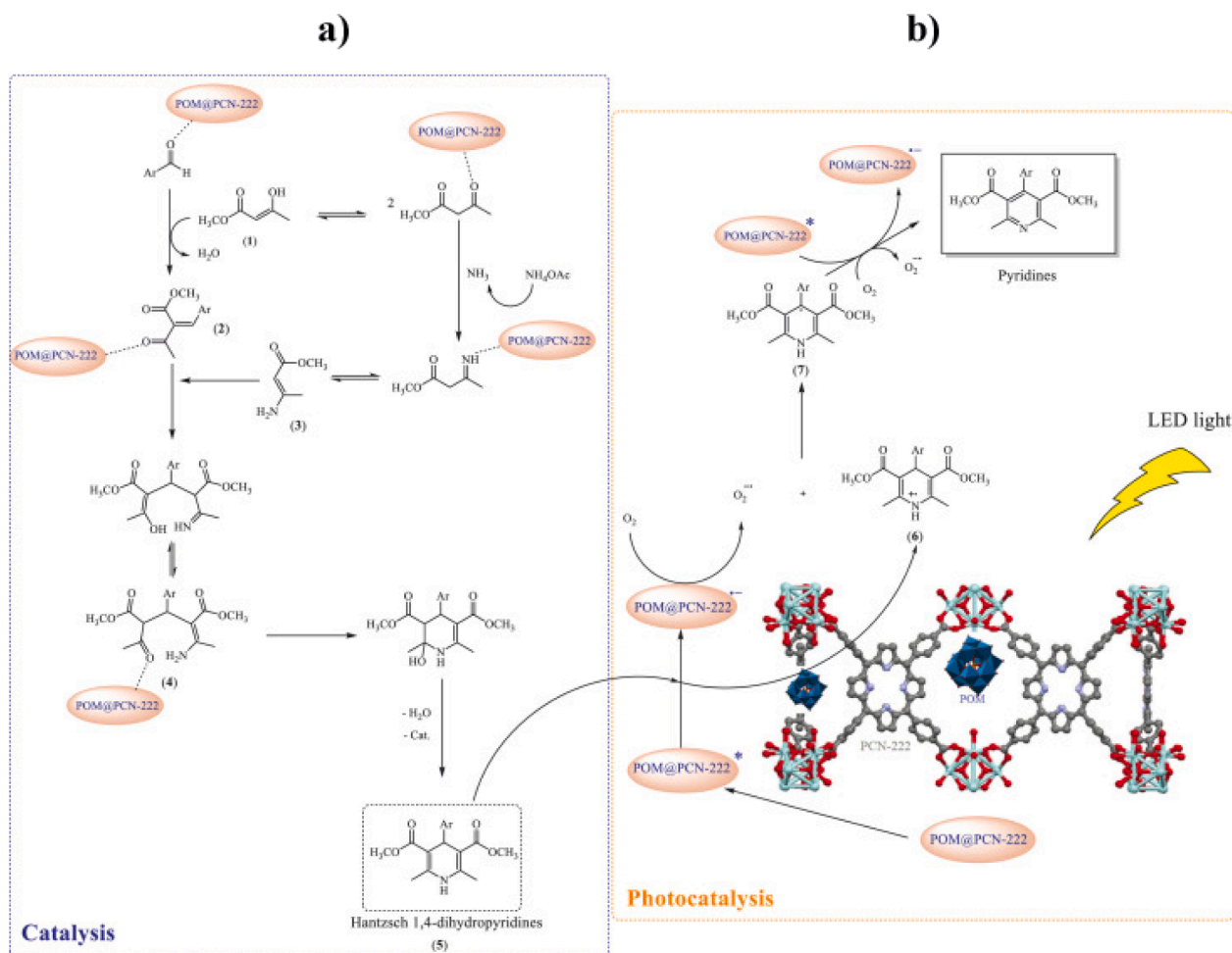**Fig. 26.** The proposed synergistic (a) catalytic and (b) photocatalytic mechanism for the synthesis of pyridine derivatives in a one-pot strategy under visible-LED-light using POM@MOF-545 as a catalyst. Reproduced with permission from Ref [209]. Copyright 2022 Elsevier.
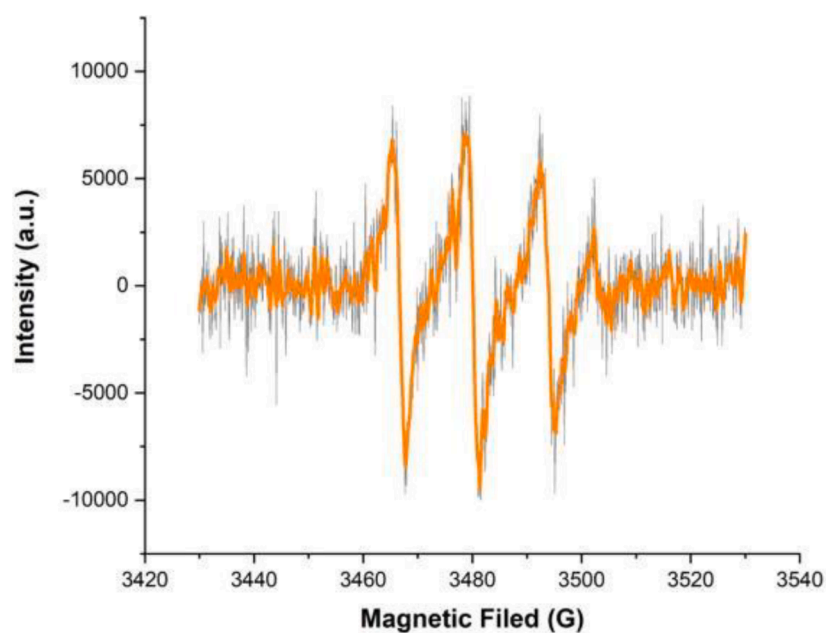

Fig. 27. EPR signal of superoxide radical anion ($O_2^{\bullet-}$). Reproduced with permission from Ref [209]. Copyright 2022 Elsevier.

pyridine derivatives by reaction with O_2 without the addition of any extra chemical supplements, which would be beneficial for both the pharmaceutical industry and organic chemists seeking ease and selectivity of reaction.

Innumerable challenges lie ahead in synthesizing and using porphyrinic POMMOF catalysts; however, we hope that our review has presented an important and systematic overview of the field, which will encourage researchers to develop new strategies for the rational design and use of these compounds for heterogeneous catalytic reactions in the near future.

4. Conclusions and future perspectives

To sum up, POMs and MPs, on which this review has focused, are known as two notable groups of molecular catalysts and have attracted significant interest in recent years. In this work, we have outlined the two groups of porphyrinic POMMOFs synthesized so far, in which POMs either embed themselves as a guest in the MOF's channels (these are termed POM@MOFs) or are directly attached to the organic linkers or metal ions/clusters which make up the architecture of the MOF (POMMOFs); both classes together are termed POMMOFs. On one hand, the incorporation/encapsulation of POMs into porphyrinic frameworks can not only enhance the catalytic activity and stability of the network, but also improve the reusability of POMs, which currently suffer the problem of self-accumulation on use. Furthermore, this superior combination is able to improve the low surface area and/or poor electron transfer properties of POMs when they are incorporated into the MOF structure. Dispersion of POMs in the ordered channels and adjustable pores of porphyrinic MOFs can furnish the resultant POMMOFs with an ordered dissemination of POMs that act as highly efficient active sites. Additionally, this allows POMs to share with the composite as a whole their unmatched physicochemical traits, including their modifiable acid-base, redox and catalytic properties. Integration of biomimetic porphyrin metal ion complexes into the porous MOF framework, on the other hand, leads to massively increased stability, as the suicidal self-oxidation of molecular porphyrin-based compounds is obstructed by incorporation into a MOF. The result is a compound that is capable of improved catalytic activity under significantly harsher conditions, including high temperatures/pressures, vast ranges of pH, specific kinds of solvents, and so on, than the original POM and MP can withstand.

The crystalline porphyrinic POMMOFs, as an ever-increasing subset of POMMOFs, combine the various advantages listed above to serve as excellent heterogeneous catalysts in plenty of catalytic reactions, including photocatalysis, alkylation, hydrolysis, detoxification, electrocatalysis, biocatalysis, oxidation, epoxidation, acylation esterification, and others. Therefore, porphyrinic POMMOFs, with their distinctive chemical architectures and frameworks, are rewarding targets for investigation of their structural features. In addition, POM and MP insertion in MOF composition can facilitate the interactions between active sites, reagents and products. It can also further improve the high surface areas and hydrophilic/hydrophobic properties of cavities and surfaces in MOFs, which will be beneficial for their catalytic performances and selectivity towards different reactants. The nanoscale structure of the MOF framework, and its strong selectivity, call for further investigation in order to explore the full range of possibilities they represent. Only a limited number of studies have benefitted from the sophisticated catalytic properties of porphyrinic POMMOFs for heterogeneous catalysis.

Even though, compared with many other types of POMs and MPs, the porphyrinic POMMOFs reported so far are very limited in both numbers and diversity. The kinds of POMs that have been engaged as synthons for fabrication of porphyrinic POMMOFs are still mainly limited to some decavanadates and Keggin- and Anderson-type POMs. Since the O atoms on the exterior of POM clusters contribute as strong M=O bonds, they are almost chemically inactive; merely a small number of POMMOFs could be straightforwardly functionalized by POM-hybrid components

and organic linkers due to the electronic repulsion. Moreover, the porphyrin linkers used to synthesize such POMMOFs are also restricted to a few types such as TCPP, TAPP, TPyP, and TPP; there is a lot of unexplored territory in the field of porphyrinic MOFs as regards linker type.

However, the results of deploying these systems as heterogeneous catalysts have been positive for a variety of reactions, they have demonstrated appealing catalytic efficiencies, involving high durability, performance, recyclability, and selectivity which surpassed those of their individual precursors. That said, to date their catalytic utilizations have been principally concentrated in certain fields: photocatalysis, electrocatalytic CO_2 reduction, OER and some limited organic transformations. There remains a great deal of work to do to improve the catalytic proficiency of porphyrinic POMMOFs in these reaction types and extend it to others; and the studies on porphyrinic POMMOFs have almost unanimously focused on the functionalization of the POMs thanks to their advantages in the various reaction types discussed above, with variation of the linkers being (as noted) an underexplored field. By and large, accurate and detailed understanding of catalytic mechanisms is a high priority and it is important to be able to predict them, particularly in terms of the correlation between the fundamental characteristics of the reactants and how they are activated, and the active sites of porphyrinic POMMOFs. The information so far available on POMs and MOFs is very extensive, and we hold that porphyrinic POMMOFs will continue to draw attention and that their catalytic exploitation will increase and improve. The unique synergy between hydrophilic POMs and readily-substituted porphyrinic MOFs leads to highly valuable potential utilizations not only in the catalytic realm, but also in a variety of applications in biomedicine, photocalysis, electrochemical oxidation/reduction, magnetism, lithium-ion batteries, supercapacitors, bio-fuel and energy storage, and others. Porphyrinic POMMOFs are advanced porous materials that simultaneously exhibit the unique and typical features of POMs, MPs and MOFs, which are notable for their redox chemistry, for their biomimetic behavior, and for their porosity and high surface areas, respectively.

While we have found many interesting examples of research into them to discuss, experimentation on porous porphyrinic POMMOFs is still in its infancy. It is anticipated that further comprehensive investigations will be carried out to probe and extend the capabilities of porphyrinic POMMOFs as effective porous heterogeneous catalysts. We hope that our detailed review can contribute a valuable knowledge base for subsequent investigations and enhancement of porphyrinic POMMOFs, which we are certain it will continue to captivate researchers in the field of catalysis as development of these systems continues.

CRediT authorship contribution statement

Arash Ebrahimi: Conceptualization, Software, Writing – original draft. **Lukáš Krivosudský:** Validation, Writing – review & editing, Supervision, Project administration, Funding acquisition. **Alexey Cherevan:** Validation, Writing – review & editing, Project administration. **Dominik Eder:** Supervision, Project administration.

Declaration of competing interest

The authors declare that they have no known competing financial interests or personal relationships that could have appeared to influence the work reported in this paper.

Data availability

No data was used for the research described in the article.

Acknowledgments

References

[1] L. Cronin, A. Müller, From serendipity to design of polyoxometalates at the nanoscale, aesthetic beauty and applications, Chem. Soc. Rev. 41 (2012) 7333–7334, https://doi.org/10.1039/C2CS90087D.

[2] A.S. Cherevan, S.P. Nandan, I. Roger, R. Liu, C. Streb, D. Eder, Polyoxometalates on functional substrates: concepts, synergies, and future perspectives, Adv. Sci. 7 (2020) 1903511, https://doi.org/10.1002/advs.201903511.

[3] A.V. Anyushin, A. Kondinski, T.N. Parac-Vogt, Hybrid polyoxometalates as post-functionalization platforms: from fundamentals to emerging applications, Chem. Soc. Rev. 49 (2020) 382–432, https://doi.org/10.1039/C8CS00854J.

[4] J. Zhang, Y. Huang, G. Li, Y. Wei, Recent advances in alkoxylation chemistry of polyoxometalates: from synthetic strategies, structural overviews to functional applications, Coord. Chem. Rev. 378 (2019) 395–414, https://doi.org/10.1016/j.ccr.2017.10.025.

[5] Q. Liu, X. Wang, Polyoxometalate clusters: sub-nanometer building blocks for construction of advanced materials, Matter. 2 (2020) 816–841, https://doi.org/10.1016/j.matt.2020.01.020.

[6] S.-S. Wang, G.-Y. Yang, Recent advances in polyoxometalate-catalyzed reactions, Chem. Rev. 115 (2015) 4893–4962, https://doi.org/10.1021/cr500390v.

[7] J.-C. Liu, Q. Han, L.-J. Chen, J.-W. Zhao, C. Streb, Y.-F. Song, Aggregation of Giant cerium-bismuth tungstate clusters into a 3D porous framework with high proton conductivity, Angew. Chem. Int. Ed. 57 (2018) 8416–8420, https://doi.org/10.1002/anie.201803649.

[8] M. Taghizadeh, E. Mehrvarz, A. Taghipour, Polyoxometalate as an effective catalyst for the oxidative desulfurization of liquid fuels: a critical review, Rev. Chem. Eng. 36 (2019) 831–858, https://doi.org/10.1515/revce-2018-0058.

[9] D.-L. Long, R. Tsunashima, L. Cronin, Polyoxometalates: building blocks for functional nanoscale systems, Angew. Chem., Int. Ed. 49 (2010) 1736–1758, https://doi.org/10.1002/anie.200902483.

[10] D.-Y. Du, J.-S. Qin, S.-L. Li, Z.-M. Su, Y.-Q. Lan, Recent advances in porous polyoxometalate-based metal-organic framework materials, Chem. Soc. Rev. 43 (2014) 4615–4632, https://doi.org/10.1039/C3CS60404G.

[11] I.A. Weinstock, R.E. Schreiber, R. Neumann, Dioxygen in polyoxometalate mediated reactions, Chem. Rev. 118 (2018) 2680–2717, https://doi.org/10.1021/acs.chemrev.7b00444.

[12] J. Dong, J. Hu, Y. Chi, Z. Lin, B. Zou, S. Yang, C.L. Hill, C. Hu, A polyoxoniobate-polyoxovanadate double-anion catalyst for simultaneous oxidative and hydrolytic decontamination of chemical warfare agent simulants, Angew. Chem., Int. Ed. 56 (2017) 4473–4477, https://doi.org/10.1002/anie.201700159.

[13] M. Sun, J. Zhang, P. Putaj, V. Caps, F. Lefebvre, J. Pelletier, J.-M. Basset, Catalytic oxidation of light alkanes (C1–C4) by heteropoly compounds, Chem. Rev. 114 (2014) 981–1019, https://doi.org/10.1021/cr300302b.

[14] E. Fernandez-Bartolome, J. Santos, S. Khodabakhshi, L.J. McCormick, S.J. Teat, C. Saenz de Pipaon, J.R. Galan-Mascarós, N. Martín, J.S. Costa, A robust and unique iron (II) mosaic-like MOF, Chem. Commun. 54 (2018) 5526–5529, https://doi.org/10.1039/C8CC01561A.

[15] J.M. Casas-Solvas, A. Vargas-Berenguel, Porous metal-organic framework nanoparticles, Nanomaterials 12 (2022) 507, https://doi.org/10.3390/nano12030527.

[16] Q. Wang, Q. Gao, A.M. Al-Enizi, A. Nafady, S. Ma, Recent advances in MOF-based photocatalysis: environmental remediation under visible light, Inorg. Chem. Front. 7 (2020) 300–339, https://doi.org/10.1039/C9QI01120J.

[17] Z. Gharehdaghi, R. Rahimi, S.M. Naghib, F. Molaabasi, Fabrication and application of copper metal-organic frameworks as nanocarriers for pH-responsive anticancer drug delivery, J. Iran. Chem. Soc. 19 (2022) 2227–2737, https://doi.org/10.1007/s13738-021-02490-8.

[18] J. Chen, Y. Zhu, S. Kaskel, Porphyrin-based metal-organic frameworks for biomedical applications, Angew. Chem. Int. Ed. 60 (2021) 5010–5035, https://doi.org/10.1002/anie.201909880.

[19] T. Rasheed, K. Rizwan, Metal-organic frameworks based hybrid nanocomposites as state-of-the-art analytical tools for electrochemical sensing applications, Biosens. Bioelectron. 199 (2022) 113867–113878, https://doi.org/10.1016/j.bios.2021.113867.

[20] Y. Bai, Y. Duo, L.-H. Xie, W. Rutledge, J.-R. Li, H.-C. Zhou, Zr-based metal-organic frameworks: design, synthesis, structure, and applications, Chem. Soc. Rev. 45 (2016) 2327–2367, https://doi.org/10.1039/C5CS00837A.

[21] J.-S. Qin, S. Yuan, Q. Wang, A. Alsalme, H.-C. Zhou, Mixed-linker strategy for the construction of multifunctional metal-organic frameworks, J. Mater. Chem. a. 5 (2017) 4280–4291, https://doi.org/10.1039/C6TA10281F.

[22] O. Karagiaridi, W. Bury, J.E. Mondloch, J.T. Hupp, O.K. Farha, Solvent-assisted linker exchange: an alternative to the de novo synthesis of unattainable metal–organic frameworks, Angew. Chem. Int. Ed. 53 (2014) 4530–4540, https://doi.org/10.1002/anie.201306923.

[23] S.S. Rajasree, X. Li, P. Deria, Physical properties of porphyrin-based crystalline metal-organic frameworks, Commun Chem. 4 (2021) 47, https://doi.org/10.1038/s42004-021-00484-4.

[24] B. Meunier, S.P. de Visser, S. Shaik, Mechanism of oxidation reactions catalyzed by cytochrome P-450 enzymes, Chem. Rev. 104 (2004) 3947–3980, https://doi.org/10.1021/cr020443g.

[25] S. Shao, V. Rajendiran, J.F. Lovell, Metalloporphyrin nanoparticles: coordinating diverse theranostic functions, Coord. Chem. Rev. 379 (2019) 99–120, https://doi.org/10.1016/j.ccr.2017.09.002.

[26] S. Shaik, S. Cohen, Y. Wang, H. Chen, D. Kumar, W. Thiel, P-450 enzymes: their structure, reactivity, and selectivity-modeled by QM/MM calculations, Chem. Rev. 110 (2010) 949–1017, https://doi.org/10.1021/cr900121s.

[27] C.F. Pereira, M.M.Q. Simões, J.P.C. Tomé, F.A. Almeida Paz, Porphyrin-based metal-organic frameworks as heterogeneous catalysts in oxidation reactions, Molecules 21 (2016) 1348, https://doi.org/10.3390/molecules21101348.

[28] D. Mansuy, Activation of alkanes: the biomimetic approach, Coord. Chem. Rev. 125 (1993) 129–141, https://doi.org/10.1016/0010-8545(93)85013-T.

[29] J.J. Perry, J.A. Perman, M.J. Zaworotko, Design and synthesis of metal-organic frameworks using metal-organic polyhedra as supermolecular building blocks, Chem. Soc. Rev. 38 (2009) 1400–1417, https://doi.org/10.1039/B807086P.

[30] L.-J. Chen, X. Zhao, X.-P. Yan, Porphyrinic metal-organic frameworks for biological applications, Adv Sens. Energy Mater. 2 (2023) 100045, https://doi.org/10.1016/j.asems.2022.100045.

[31] A.A. Vodyashkin, A.V. Sergorodceva, P. Kezimana, Y.M. Stanishevskiy, Metal-organic framework (MOF)—a universal material for biomedicine, Int. J. Mol. Sci. 24 (2023) 7819, https://doi.org/10.3390/ijms24097819.

[32] X. Zhao, Z. Zhang, X. Cai, B. Ding, C. Sun, G. Liu, C. Hu, S. Shao, M. Pang, Postsynthetic ligand exchange of metal-organic framework for photodynamic therapy, ACS Appl. Mater. Interfaces. 11 (2019) 7884–7892, https://doi.org/10.1021/acsami.9b00740.

[33] X. Zheng, L. Wang, M. Liu, P. Lei, F. Liu, Z. Xie, Nanoscale mixed-component metal-organic frameworks with photosensitizer spatial-arrangement-dependent photochemistry for multimodal-imaging-guided photothermal therapy, Chem. Mater. 30 (2018) 6867–6876, https://doi.org/10.1021/acs.chemmater.8b03043.

[34] X. Zhang, M.C. Wasson, M. Shayan, E.K. Berdichevsky, J. Ricardo-Noordberg, Z. Singh, E.K. Papazyan, A.J. Castro, P. Marino, Z. Ajoyan, Z. Chen, T. Islamoglu, A.J. Howarth, Y. Liu, M.B. Majewski, M.J. Katz, J.E. Mondloch, O.K. Farha, A historical perspective on porphyrin-based metal-organic frameworks and their applications, Coord. Chem. Rev. 429 (2021) 213615, https://doi.org/10.1016/j.ccr.2020.213615.

[35] P. Mialane, C. Mellot-Draznieks, P. Gairola, M. Duguet, Y. Benseghir, O. Oms, A. Dolbecq, Heterogenisation of polyoxometalates and other metal-based complexes in metal-organic frameworks: from synthesis to characterisation and applications in catalysis, Chem. Soc. Rev. 50 (2021) 6152–6220, https://doi.org/10.1039/D0CS00323A.

[36] X.-X. Li, D. Zhao, S.-T. Zheng, Recent advances in POM-organic frameworks and POM-organic polyhedra, Coord. Chem. Rev. 397 (2019) 220–240, https://doi.org/10.1016/j.ccr.2019.07.005.

[37] M. Samaniyan, M. Mirzaei, R. Khajavian, H. Eshtiagh-Hosseini, C. Streb, Heterogeneous catalysis by polyoxometalates in metal-organic frameworks, ACS Catal. 9 (2019) 10174–10191, https://doi.org/10.1021/acscatal.9b03439.

[38] J.-X. Liu, X.-B. Zhang, Y.-L. Li, S.-L. Huang, G.-Y. Yang, Polyoxometalate functionalized architectures, Coord. Chem. Rev. 414 (2020) 213260, https://doi.org/10.1016/j.ccr.2020.213260.

[39] T. Ohmura, N. Setoyama, Y. Mukae, A. Usuki, S. Senda, T. Matsumoto, K. Tatsumi, Supramolecular porphyrin-based metal-organic frameworks: CU(II) naphthoate-CU(II) tetrapyridyl porphine structures exhibiting selective CO2/N2 separation, CrstEngComm 19 (2017) 5173–5177, https://doi.org/10.1039/C7CE01138E.

[40] S. Abednatanzi, P.G. Derakhshandeh, H. Depauw, F.-X. Coudert, H. Vrielinck, P. Van Der Voort, K. Leus, Mixed-metal metal-organic frameworks, Chem. Soc. Rev. 48 (2019) 2535–2565, https://doi.org/10.1039/C8CS00337H.

[41] J.W. Han, C.L. Hill, A coordination network that catalyzes O2-based oxidations, J. Am. Chem. Soc. 129 (2007) 15094–15095, https://doi.org/10.1021/ja069319v.

[42] X.-X. Li, L.-J. Zhang, C.-Y. Cui, R.-H. Wang, G.-Y. Yang, Designed construction of cluster organic frameworks from lindqvist-type polyoxovanadate cluster, Inorg. Chem. 57 (2018) 10323–10330, https://doi.org/10.1021/acs.inorgchem.8b01528.

[43] G.A. Senchyk, A.B. Lysenko, A.A. Babaryk, E.B. Rusanov, H. Krautscheid, P. Neves, A.A. Valente, I.S. Gonçalves, K.W. Krämer, S.-X. Liu, S. Decurtins, K.V. Domasevitch, Triazolyl-based copper-molybdate hybrids: from composition space diagram to magnetism and catalytic performance, Inorg. Chem. 53 (2014) 10112–10121, https://doi.org/10.1021/ic5009736.

[44] S. Zhang, F. Ou, S. Ning, P. Cheng, Polyoxometalate-based metal-organic frameworks for heterogeneous catalysis, Inorg. Chem. Front. 8 (2021) 1865–1899, https://doi.org/10.1039/D0QI01407A.

[45] C.T. Buru, O.K. Farha, Strategies for incorporating catalytically active polyoxometalates in metal-organic frameworks for organic transformations, ACS Appl. Mater. Interfaces. 12 (2020) 5345–5360, https://doi.org/10.1021/acsami.9b19785.

[46] K. Maru, S. Kalla, R. Jangir, MOF/POM hybrids as catalysts for organic transformations, Dalton Trans. 51 (2022) 11952–11986, https://doi.org/10.1039/D2DT01895K.

[47] K.P. Sullivan, Q. Yin, D.L. Collins-Wildman, M. Tao, Y.V. Geletii, D.G. Musaev, T. Lian, C.L. Hill, Multi-tasking POM systems, Front. Chem. 6 (2018) 365, https://doi.org/10.3389/fchem.2018.00365.

[48] O.A. Kholdeeva, N.V. Maksimchuk, G.M. Maksimov, Polyoxometalate-based heterogeneous catalysts for liquid phase selective oxidations: comparison of different strategies, Catal. Today. 15 (2010) 107–113, https://doi.org/10.1016/j.cattod.2009.12.016.

[49] W.-Q. Kan, S.-Z. Wen, Y.-H. Kan, H.-Y. Hu, S.-Y. Niu, X.-Y. Zhang, Four polyoxometalate-based semiconductive coordination polymers: syntheses, structures, photoluminescent and photocatalytic properties, Synth. Met. 198 (2014) 51–58, https://doi.org/10.1016/j.synthmet.2014.09.028.

[50] Y. Liu, C. Tang, M. Cheng, M. Chen, S. Chen, L. Lei, Y. Chen, H. Yi, Y. Fu, L. Li, Polyoxometalate@Metal-organic framework composites as effective photocatalysts, ACS Catal. 11 (2021) 13374–13396, https://doi.org/10.1021/acscatal.1c03866.

[51] J. Chen, K. Shen, Y. Li, Greening the processes of metal-organic framework synthesis and their use in sustainable catalysis, ChemSusChem 10 (2017) 3165–3187, https://doi.org/10.1002/cssc.201700748.

[52] S.-W. Lia, Z. Yang, R.-M. Gao, G. Zhang, J.-S. Zhao, Direct synthesis of mesoporous SRL-POM@MOF-199@MCM-41 and its highly catalytic performance for the oxide sulfurization of DBT, Appl. Catal. B. 221 (2018) 574–583, https://doi.org/10.1016/j.apcatb.2017.09.044.

[53] Z. Li, G. Li, C. Li, S. Dong, R. Tang, C. Wang, Z. Zhang, L. Yin, Rational microstructure design on metal-organic framework composites for better electrochemical performances: design principle synthetic strategy, and promotion mechanism, Small. 4 (2020) 1900756, https://doi.org/10.1002/smtd.201900756.

[54] J. Liu, M. Huang, Z. Hua, Y. Dong, Z. Feng, T. Sun, C. Chen, Polyoxometalate-based metal organic frameworks: recent advances and challenges, ChemistrySelect 7 (2022) e202200546.

[55] I. Ullah, A. Munir, A. Haider, N. Ullah, Supported polyoxometalates as emerging nanohybrid materials for photochemical and photoelectrochemical water splitting, Nanophotonics. 10 (2021) 1595–1620, https://doi.org/10.1515/nanoph-2020-0542.

[56] A. Bavykina, N. Kolobov, I.S. Khan, J.A. Bau, A. Ramire, J. Gascon, Metal-organic frameworks in heterogeneous catalysis: recent progress, new trends, and future perspectives, Chem. Rev. 120 (2020) 8468–8535, https://doi.org/10.1021/acs.chemrev.9b00685.

[57] M. Mirzaei, H. Eshtiagh-Hosseini, M. Alipour, A. Frontera, Recent developments in the crystal engineering of diverse coordination modes (0–12) for keggin-type polyoxometalates in hybrid inorganic–organic architectures, Coord. Chem. Rev. 275 (2014) 1–18, https://doi.org/10.1016/j.ccr.2014.03.012.

[58] L. Feng, K.-Y. Wang, J. Willman, H.-C. Zhou, Hierarchy in metal-organic frameworks, ACS Cent. Sci. 6 (2020) 359–367, https://doi.org/10.1021/acscentsci.0c00158.

[59] M. Lu, M. Zhang, J. Liu, T.-Y. Yu, J.-N. Chang, L.-J. Shang, S.-L. Li, Y.-Q. Lan, Confining and highly dispersing single polyoxometalate clusters in covalent organic frameworks by covalent linkages for CO2 photoreduction, J. Am. Chem. Soc. 144 (2022) 1861–1871, https://doi.org/10.1021/jacs.1c11987.

[60] S. Roy, V. Vemuri, S. Maiti, K.S. Manoj, U. Subbarao, S.C. Peter, Two keggin-based isostructural POMOF hybrids: synthesis, crystal structure, and catalytic properties, Inorg. Chem. 57 (2018) 12078–12092, https://doi.org/10.1021/acs.inorgchem.8b01631.

[61] L. Vilà-Nadal, L. Cronin, Design and synthesis of polyoxometalate-framework materials from cluster precursors, Nat. Rev. Mater. 2 (2017) 17054, https://doi.org/10.1038/natrevmats.2017.54.

[62] H.N. Miras, L. Vilà-Nadal, L. Cronin, Polyoxometalate based open frameworks (POM-OFs), Chem. Soc. Rev. 43 (2014) 5679–5699, https://doi.org/10.1039/C4CS00097H.

[63] B. Li, D. Ma, Y. Li, Y. Zhang, G. Li, Z. Shi, S. Feng, M.J. Zaworotko, S. Ma, Dual functionalized cages in metal-organic frameworks via stepwise postsynthetic modification, Chem. Mater. 28 (2016) 4781–4786, https://doi.org/10.1021/acs.chemmater.6b01898.

[64] J. Niu, S. Zhang, H. Chen, J. Zhao, P. Ma, J. Wang, 1-D, 2-D, and 3-D organic-inorganic hybrids assembled from keggin-type polyoxometalates and 3d–4f heterometals, Cryst. Growth Des. 11 (2011) 3769–3777, https://doi.org/10.1021/cg2001249.

[65] Z. Zhuanfang, F. Enze, Z. Shuangqi, W. Zhaojun, Z. Wenzhi, Z. Ming, D.G. Hua, A new two-fold interpenetrating metal-organic framework based on polyoxometalate: synthesis, structure, efficient hydrogen evolution and dye degradation, J. Solid State Chem. 323 (2023) 124066, https://doi.org/10.1016/j.jssc.2023.124066.

[66] D. Chai, C.J. Gómez-Garcíab, B. Lia, H. Panga, H. Ma, X. Wang, L. Tan, Polyoxometalate-based metal-organic frameworks for boosting electrochemical capacitor performance, Chem. Eng. J. 373 (2019) 587, https://doi.org/10.1016/j.cej.2019.05.084.

[67] W.-L. Zhou, J. Liang, L. Zhao, X.-L. Wang, K.-Z. Shao, Z.-M. Su, Hydrothermal synthesis, crystal structure and properties of a 3D inorganic–organic hybrid based on keggin-type polyanion and silver-pyrazine circles, Inorg. Chem. Commun. 47 (2014) 48–51, https://doi.org/10.1016/j.inoche.2014.07.014.

[68] C.T. Buru, P. Li, B.L. Mehdi, A. Dohnalkova, A.E. Platero-Prats, N.D. Browning, K. W. Chapman, J.T. Hupp, O.K. Farha, Adsorption of a catalytically accessible polyoxometalate in a mesoporous channel-type metal-organic framework, Chem. Mater. 29 (2017) 5174–5181, https://doi.org/10.1021/acs.chemmater.7b00750.

[69] Z. Cui, H. Lin, L. Zeng, J. Lu, A new functionalized POM-based MOF containing 1D [Mo3O10]n2n- chains and the flexible bis(pyrazine)-bis(amide) ligand, Inorg.

Chem. Commun. 126 (2021) 108493, https://doi.org/10.1016/j.inoche.2021.108493.

[70] Y.-X. Ding, Q.-H. Zheng, M.-T. Peng, C. Chen, K.-F. Zou, B.-X. Dong, W.-L. Liu, Y.-L. Teng, A new ε-keggin polyoxometalate-based metal-organic framework: from design and synthesis to electrochemical hydrogen evolution, Catal. Commun. 161 (2021) 106367, https://doi.org/10.1016/j.catcom.2021.106367.

[71] Z.-W. Cui, H.-Y. Lin, J. Luan, Two Anderson-type polyoxometalate-based hybrids constructed with different bis(pyrazine)-bis(amide) ligands: efficient adsorption dyes and electrocatalytic activities, Polyhedron 194 (2021) 114943, https://doi.org/10.1016/j.poly.2020.114943.

[72] H.-N. Wang, M. Zhang, A.-M. Zhang, F.-C. Shen, X.-K. Wang, S.-N. Sun, Y.-J. Chen, Y.-Q. Lan, Polyoxometalate-based metal-organic frameworks with conductive polypyrrole for supercapacitors, ACS Appl. Mater. Interfaces. 10 (2018) 32265–32270, https://doi.org/10.1021/acsami.8b12194.

[73] S. Zhang, J. Zhao, P. Ma, H. Chen, J. Niu, J. Wang, Organic-inorganic hybrids based on monovacant keggin type silicotungstates and 3d–4f heterometals, Cryst. Growth Des. 12 (2012) 1263–1272, https://doi.org/10.1021/cg2012759.

[74] J. Sun, S. Abednatanzi, P. Van Der Voort, Y.-Y. Liu, K. Leus, POM@MOF hybrids: synthesis and applications, Catalysts 10 (2020) 578, https://doi.org/10.3390/catal10050578.

[75] Z.-H. Wang, X.-F. Wang, Z. Tan, X.-Z. Song, Polyoxometalate/metal-organic framework hybrids and their derivatives for hydrogen and oxygen evolution electrocatalysis, Mater. Today Energy. 19 (2021) 100618, https://doi.org/10.1016/j.mtener.2020.100618.

[76] N. Li, J. Liu, B.-X. Dong, Y.-Q. Lan, Polyoxometalate-based compounds for photo- and electrocatalytic applications, Angew. Chem. Int. Ed. 59 (2020) 20779–20793, https://doi.org/10.1002/anie.202008054.

[77] J.-J. Ye, C.-D. Wu, Immobilization of polyoxometalates in crystalline solids for highly efficient heterogeneous catalysis, Dalton Trans. 45 (2016) 10101–10112, https://doi.org/10.1039/C6DT01378C.

[78] C. Streb, C. Ritchie, D.-L. Long, P. Kögerler, L. Cronin, Modular assembly of a functional polyoxometalate-based open framework constructed from unsupported AgI···AgI interactions, Angew. Chem. Int. Ed. 46 (2007) 7579–7582, https://doi.org/10.1002/anie.200702698.

[79] P. Yang, W. Zhao, A. Shkurenko, Y. Belmabkhout, M. Eddaoudi, X. Dong, H. N. Alshareef, N.M. Khashab, Polyoxometalate-cyclodextrin metal-organic frameworks: from tunable structure to customized storage functionality, J. Am. Chem. Soc. 141 (2019) 1847–1851, https://doi.org/10.1021/jacs.8b11998.

[80] W. Xu, X. Pei, C.S. Diercks, H. Lyu, Z. Ji, O.M. Yaghi, A metal-organic framework of organic vertices and polyoxometalate linkers as a solid-state electrolyte, J. Am. Chem. Soc. 141 (2019) 17522–17526, https://doi.org/10.1021/jacs.9b10418.

[81] Y. Liu, S. Liu, S. Liu, D. Liang, S. Li, Q. Tang, X. Wang, J. Miao, Z. Shi, Z. Zheng, Facile synthesis of a nanocrystalline metal-organic framework impregnated with a phosphovanadomolybdate and its remarkable catalytic performance in ultradeep oxidative desulfurization, ChemCatChem 5 (2013) 3086–3091, https://doi.org/10.1002/cctc.201300378.

[82] J. Lan, Y. Wang, B. Huang, Z. Xiao, P. Wu, Application of polyoxometalates in photocatalytic degradation of organic pollutants, Nanoscale Adv 3 (2021) 4646–4658, https://doi.org/10.1039/D1NA00408E.

[83] X. Xu, X. Lu, Y. Yang, F. Nosheen, X. Wang, Tuning the growth of metal-organic framework nanocrystals by using polyoxometalates as coordination modulators, Sci. China Mater. 58 (2015) 370–377, https://doi.org/10.1007/s40843-015-0053-2.

[84] X.-L. Yang, Y.-S. Ye, Z.-M. Wang, Z.-H. Zhang, Y.-L. Zhao, F. Yang, Z.-Y. Zhu, T. Wei, POM-based MOF-derived Co3O4/CoMoO4 nanohybrids as anodes for high-performance lithium-ion batteries, ACS Omega 5 (2020) 26230–26236, https://doi.org/10.1021/acsomega.0c03929.

[85] B. Silva, O.J. de Barros, A.C. de Lima Neto, J. Oliveira Frós, Metal-organic framework nanocrystals, ChemistrySelect 3 (2018) 7459–7471, https://doi.org/10.1002/slct.201801423.

[86] C. Dey, T. Kundu, R. Banerjee, Reversible phase transformation in proton conducting strandberg-type POM based metal organic material, Chem. Commun. 48 (2012) 266–268, https://doi.org/10.1039/C1CC15162B.

[87] W.-W. He, S.-L. Li, H.-Y. Zang, G.-S. Yang, S.-R. Zhang, Z.-M. Su, Y.-Q. Lan, Entangled structures in polyoxometalate-based coordination polymers, Coord. Chem. Rev. 279 (2014) 141–160, https://doi.org/10.1016/j.ccr.2014.03.022.

[88] Y.-F. Song, D.-L. Long, C. Ritchie, L. Cronin, Nanoscale polyoxometalate-based inorganic/organic hybrids, Chem. Soc. Jpn. 11 (2011) 158–171, https://doi.org/10.1002/tcr.201100002.

[89] D. Wang, L. Liu, J. Jiang, L. Chen, J. Zhao, Polyoxometalate-based composite materials in electrochemistry: state-of-the-art progress and future outlook, Nanoscale. 12 (2020) 5705–5718, https://doi.org/10.1039/C9NR10573E.

[90] S.Y. Lai, K.H. Ng, C.K. Cheng, H. Nur, M. Nurhadi, M. Arumugam, Photocatalytic remediation of organic waste over keggin-based polyoxometalate materials: a review, Chemosphere 263 (2021) 128244, https://doi.org/10.1016/j.chemosphere.2020.128244.

[91] M. Zhao, S. Ou, C.-D. Wu, Porous metal-organic frameworks for heterogeneous biomimetic catalysis, Acc. Chem. Res. 47 (2014) 1199–1207, https://doi.org/10.1021/ar400265x.

[92] D. Li, H.-Q. Xu, L. Jiao, H.-L. Jiang, Metal-organic frameworks for catalysis: state of the art, challenges, and opportunities, EnergyChem. 1 (2019) 100005, https://doi.org/10.1016/j.enchem.2019.100005.

[93] S.-S. Wang, W.-B. Yang, W. Yang, X.-Y. Wu, W. Wu, S.-X. Wang, L. Lin, C.-Z. Lu, A bi-polyoxometallate-based host–guest metal-organic framework, Chem. Commun. 56 (2020) 2503–2506, https://doi.org/10.1039/C9CC09008H.

[94] M.A. Nasalevich, M. van der Veen, F. Kapteijn, J. Gascon, Metal-organic frameworks as heterogeneous photocatalysts: advantages and challenges, CrstEngComm 16 (2014) 4919–4926, https://doi.org/10.1039/C4CE00032C.

[95] Y. Ma, H. Peng, J. Liu, Y. Wang, X. Hao, X. Feng, S.U. Khan, H. Tan, Y. Li, Polyoxometalate-based metal-organic frameworks for selective oxidation of aryl alkenes to aldehydes, Inorg. Chem. 57 (2018) 4109–4116, https://doi.org/10.1021/acs.inorgchem.8b00282.

[96] D. Li, Q. Xu, Y. Li, Y. Qiu, P. Ma, J. Niu, J. Wang, A stable polyoxometalate-based metal-organic framework as highly efficient heterogeneous catalyst for oxidation of alcohols, Inorg. Chem. 58 (2019) 4945–4953, https://doi.org/10.1021/acs.inorgchem.8b03589.

[97] Y. Ren, M. Wang, X. Chen, B. Yue, H. He, Heterogeneous catalysis of polyoxometalate based organic-inorganic hybrids, Materials. 8 (2015) 1545–1567, https://doi.org/10.3390/ma8041545.

[98] Y. Hou, P. Han, L. Zhang, H. Li, Z. Xu, pH-controlled assembling of POM-based metal-organic frameworks for use as supercapacitors and efficient oxidation catalysts for various sulfides, Inorg. Chem. Front. 10 (2023) 148–157, https://doi.org/10.1039/D2QI01922A.

[99] X. Zhong, Y. Lu, F. Luo, Y. Liu, X. Li, S. Liu, A nanocrystalline POM@MOFs catalyst for the degradation of phenol: effective cooperative catalysis by metal nodes and POM guests, Chem. Eur. J. 24 (2018) 3045–3051, https://doi.org/10.1002/chem.201705677.

[100] S. Zhang, W. Shi, P. Cheng, The coordination chemistry of N-heterocyclic carboxylic acid: a comparison of the coordination polymers constructed by 4,5-imidazoledicarboxylic acid and 1H–1,2,3-triazole-4,5-dicarboxylic acid, Coord. Chem. Rev. 352 (2017) 108–150, https://doi.org/10.1016/j.ccr.2017.08.022.

[101] X. Zhao, S. Zhang, J. Yang, L. Li, G. Wu, W. Shi, G. Yang, N. Guan, P. Cheng, Polyoxometalate-based metal-organic frameworks as visible-light-induced photocatalysts, Inorg. Chem. 57 (2018) 5030–5037, https://doi.org/10.1021/acs.inorgchem.8b00098.

[102] L. Jiao, Y. Wang, H.-L. Jiang, Q. Xu, Metal-organic frameworks as platforms for catalytic applications, Adv. Mat 30 (2018) 1703663, https://doi.org/10.1002/adma.201703663.

[103] N. Lotfian, M.M. Heravi, M. Mirzaei, B. Heidari, Applications of inorganic-organic hybrid architectures based on polyoxometalates in catalyzed and photocatalyzed chemical transformations, Appl. Organomet. Chem. 33 (2019) e4808.

[104] A. Haruna, Z. Merican, A. Merican, S.G. Musa, Recent advances in catalytic oxidative desulfurization of fuel oil – a review, J. Ind. Eng. Chem. 112 (2022) 20–36, https://doi.org/10.1016/j.jiec.2022.05.023.

[105] S. Parshamoni, C. Viravaux, M. Robert, C. Mellot-Draznieks, G. Chen, P. Mialane, A. Dolbecq, J. Bonin, Heterogenization of molecular cobalt catalysts in robust metal-organic frameworks for efficient photocatalytic CO₂ reduction, catal, Sci. Technol. 12 (2022) 5418–5424, https://doi.org/10.1039/D2CY01147F.

[106] J.-W. Sun, P.-F. Yan, G.-H. An, J.-Q. Sha, C. Wang, G.-M. Li, POM species, temperature and counterions modulated the various dimensionalities of POM-based metal–organic frameworks, Dalton Trans. 45 (2016) 1657–1667, https://doi.org/10.1039/C5DT04094A.

[107] M.-X. Yang, S. Lin, L.-J. Chen, X.-H. Chen, X.-H. Yang, J. Guo, Three POM-based MOFs containing Ag/3-pttz frameworks with 1D to 3D features, Polyhedron 87 (2015) 329–337, https://doi.org/10.1016/j.poly.2014.11.021.

[108] L. Liu, H.-Y. Zhang, H.-J. Wang, S. Chen, J.-H. Wang, J.-W. Sun, Metallocycle-supported POM-based metal-organic frameworks assembled from isomeric N-rich ligands: structures and selective adsorption and separation of cationic dyes, Eur. J. Inorg. Chem. 2019 (2019) 1839–1846, https://doi.org/10.1002/ejic.201900086.

[109] M. Wei, X. Wang, X. Duan, Crystal structures and proton conductivities of a MOF and two POM–MOF composites based on CuII ions and 2,2′-Bipyridyl-3,3′-dicarboxylic acid, Chem. Eur. J. 19 (2013) 1607–1616, https://doi.org/10.1002/chem.201203154.

[110] Z. Fang, D. Chen, Z. Li, X. Ma, X. Wan, Z. Deng, X. Peng, A self-confinement synthesis of a POM-decorated MOF thin film for actively hydrolyzing ethyl acetate, Chem. Commun. 56 (2020) 13840–13843, https://doi.org/10.1039/D0CC05637E.

[111] T.-P. Hu, Y.-Q. Zhao, K. Mei, S.-J. Lin, X.-P. Wang, D. Sun, A novel silver(i)-keggin-polyoxometalate inorganic–organic hybrid: a Lewis acid catalyst for cyanosilylation reaction, CrstEngComm 17 (2015) 5947–5952, https://doi.org/10.1039/C5CE00953G.

[112] S. Abednatanzi, K. Leus, P. Gohari Derakhshandeh, F. Nahra, K. De Keukeleere, K. Van Hecke, I. Van Driessche, A. Abbasi, S.P. Nolan, P., Van der voort, POM@IL-MOFs – inclusion of POMs in ionic liquid modified MOFs to produce recyclable oxidation catalysts, Catal. Sci. Technol. 7 (2017) 1478–1487, https://doi.org/10.1039/C6CY02662A.

[113] S. Ahn, S.L. Nauert, C.T. Buru, M. Rimoldi, H. Choi, N.M. Schweitzer, J.T. Hupp, O.K. Farha, J.M. Notestein, Pushing the limits on metal-organic frameworks as a catalyst support: NU-1000 supported tungsten catalysts for *o*-xylene isomerization and disproportionation, J. Am. Chem. Soc. 140 (2018) 8535–8543, https://doi.org/10.1021/jacs.8b04059.

[114] Q. Niu, G. Liu, Z. Lv, C. Si, H. Han, M. Jin, Mono-substituted polyoxometalate CLUSTERS@ZR-MOFs: reactivity, kinetics, and catalysis for cycloolefins-H₂O₂ biphase reactions, Mol. Catal. 504 (2021) 111465, https://doi.org/10.1016/j.mcat.2021.111465.

[115] Y. Zhang, Y. Liu, D. Wang, J. Liu, J. Zhao, State-of-the-art advances in the syntheses, structures, and applications of polyoxometalate-based metal-organic frameworks, Polyoxometalates 2 (2023) 9140017, https://doi.org/10.26599/POM.2022.9140017.

[116] A. Ebrahimi, L. Krivosudský, Metalloporphyrin metal-organic frameworks: eminent synthetic strategies and recent practical exploitations, Molecules 27 (2022) 4917, https://doi.org/10.3390/molecules27154917.

[117] C.Y. Lee, O.K. Farha, B.J. Hong, A.A. Sarjeant, S.T. Nguyen, J.T. Hupp, Light-harvesting metal-organic frameworks (MOFs): efficient strut-to-strut energy transfer in bodipy and porphyrin-based MOFs, J. Am. Chem. Soc. 133 (2011) 15858–15861, https://doi.org/10.1021/ja206029a.

[118] G. Liu, H. Cui, S. Wang, L. Zhang, C.-Y. Su, A series of highly stable porphyrinic metal–organic frameworks based on iron–oxo chain clusters: design, synthesis and biomimetic catalysis, J. Mater. Chem. A. 8 (2020) 8376–8382, https://doi.org/10.1039/D0TA02033H.

[119] Z. Zhang, L. Zhang, L. Wojtas, M. Eddaoudi, M.J. Zaworotko, Template-directed synthesis of nets based upon octahemioctahedral cages that encapsulate catalytically active metalloporphyrins, J. Am. Chem. Soc. 134 (2012) 928–933, https://doi.org/10.1021/ja208256u.

[120] Z.-X. Yang, F. Gong, D. Lin, Y. Huo, Recent advances in polyoxometalate-based single-molecule magnets, Coor. Chem. Rev. 492 (2023) 215205, https://doi.org/10.1016/j.ccr.2023.215205.

[121] T. Rasheed, K. Rizwan, M. Bilal, H.M.N. Iqbal, Metal-organic framework-based engineered materials—fundamentals and applications, Molecules 25 (2020) 1598, https://doi.org/10.3390/molecules25071598.

[122] L. Deng, X. Dong, Z.-H. Zhou, Intrinsic molybdenum-based POMOFs with impressive gas adsorptions and photochromism, Chem. Eur. J. 27 (2021) 9643–9653, https://doi.org/10.1002/chem.202100745.

[123] N. Ogiwara, T. Iwano, T. Ito, S. Uchida, Proton conduction in ionic crystals based on polyoxometalates, Coord. Chem. Rev. 462 (2022) 214524, https://doi.org/10.1016/j.ccr.2022.214524.

[124] Z. Shi, Y. Zhou, L. Zhang, C. Mu, H. Ren, New supramolecular compounds based on porphyrin and polyoxometalate: synthesis, characterization and nonlinear optical and optical limiting properties, RSC Adv. 4 (2014) 50277–50284, https://doi.org/10.1039/C4RA09384D.

[125] W. Lin, Z. Wang, L. Ma, A novel octupolar metal-organic NLO material based on a chiral 2D coordination network, J. Am. Chem. Soc. 121 (1999) 11249–11250, https://doi.org/10.1021/ja9928327.

[126] J. Zhang, Q. Xiang, Y. Zhu, J. Yang, Y. Song, C. Zhang, Two W/S/Cu-cluster-containing metal-organic frameworks fabricated by multidentate organic ligands: new topologies, strong NLO properties, and efficient luminescent detection, Cryst. Growth Des. 21 (2021) 3225–3233, https://doi.org/10.1021/acs.cgd.0c01580.

[127] O.R. Evans, W. Lin, Crystal engineering of NLO materials based on metal-organic coordination networks, Acc. Chem. Res. 35 (2002) 511–522, https://doi.org/10.1021/ar0001012.

[128] Z. Wang, W. Yan, G. Zhao, K. Wu, Z.-G. Gu, Q.-H. Li, Novel third-order nonlinear optical materials with Craig-möbius aromaticity, J. Phys. Chem. Lett. 12 (2021) 11784–11789, https://doi.org/10.1021/acs.jpclett.1c03541.

[129] C. Zhang, Y. Song, X. Wang, Correlations between molecular structures and third-order non-linear optical functions of heterothiometallic clusters: a comparative study, Coord. Chem. Rev. 251 (2007) 111–141, https://doi.org/10.1016/j.ccr.2006.06.007.

[130] B.J. Coe, J.A. Harris, B.S. Brunschwig, I. Asselberghs, K. Clays, J. Garín, J. Orduna, Three-dimensional nonlinear optical chromophores based on metal-to-ligand charge-transfer from ruthenium (II) or iron (II) centers, J. Am. Chem. Soc. 127 (2005) 13399–13410, https://doi.org/10.1021/ja053879x.

[131] A. Colombo, C. Dragonetti, V. Guerchais, D. Roberto, An excursion in the second-order nonlinear optical properties of platinum complexes, Coord. Chem. Rev. 446 (2021) 214113, https://doi.org/10.1016/j.ccr.2021.214113.

[132] Y. Liang, W. Hu, X. Yuan, Z. Zeng, B. Zhu, Y. Gu, Switchable nonlinear optical absorption of metal-organic frameworks, Adv. Opt. Mater. 10 (2022) 2200779, https://doi.org/10.1002/adom.202200779.

[133] A. Al-Yasari, N. Van Steerteghem, H. Kearns, H. El Moll, K. Faulds, J.A. Wright, B. S. Brunschwig, K. Clays, J. Fielden, Organoimido-polyoxometalate nonlinear optical chromophores: a structural, spectroscopic, and computational study, Inorg. Chem. 56 (2017) 10181–10194, https://doi.org/10.1021/acs.inorgchem.7b00708.

[134] M.U. Khan, S. Hussain, M.A. Asghar, K.S. Munawar, R.A. Khera, M. Imran, M. M. Ibrahim, M.M. Hessien, G.A.M. Mersal, Exploration of nonlinear optical properties for the first theoretical framework of non-fullerene DTS (FBTTh2)2-based derivatives, ACS Omega 7 (2022) 18027–18040, https://doi.org/10.1021/acsomega.2c01474.

[135] Y. Pan, S. Sanati, M. Nadafan, R. Abazari, J. Gao, A.M. Kirillov, Postsynthetic modification of NU-1000 for designing a polyoxometalate-containing nanocomposite with enhanced third-order nonlinear optical performance, Inorg. Chem. 61 (2022) 18873–18882, https://doi.org/10.1021/acs.inorgchem.2c02709.

[136] R. Lamare, R. Ruppert, C. Boudon, L. Ruhlmann, J. Weiss, Porphyrins and polyoxometalate scaffolds, Chem. Eur. J. 27 (2021) 16071–16081, https://doi.org/10.1002/chem.202102277.

[137] S. Ul Hassan, H.M. Asif, Y. Zhou, L. Zhang, N. Qu, J. Li, Z. Shi, Closer is better and two is superior to one": third-order optical nonlinearities of a family of porphyrin-Anderson type polyoxometalate hybrid compounds, J. Phys. Chem. c. 120 (2016) 27587–27599, https://doi.org/10.1021/acs.jpcc.6b09951.

[138] S.-L. Zhu, X. Xu, S. Ou, M. Zhao, W.-L. He, C.-D. Wu, Assembly of a metalloporphyrin-polyoxometalate hybrid material for highly efficient activation of molecular oxygen, Inorg. Chem. 55 (2016) 7295–7300, https://doi.org/10.1021/acs.inorgchem.6b00971.

[139] N. Mizuno, K. Yamaguchi, K. Kamata, Epoxidation of olefins with hydrogen peroxide catalyzed by polyoxometalates, Coord. Chem. Rev. 249 (2005) 1944–1956, https://doi.org/10.1016/j.ccr.2004.11.019.

[140] E. Brulé, Y.R. de Miguel, Supported metalloporphyrincatalysts for alkeneepoxidation, Org. Biomol. Chem. 4 (2006) 599–609, https://doi.org/10.1039/B509985D.

[141] K. Leus, Y.-Y. Liu, P. Van der Voort, Metal-organic frameworks as selective or chiral oxidation catalysts, Catal. Rev. - Sci. Eng. 56 (2014) 1–56, https://doi.org/10.1080/01614940.2014.864145.

[142] X. Song, D. Hu, X. Yang, H. Zhang, W. Zhang, J. Li, M. Jia, J. Yu, Polyoxomolybdic cobalt encapsulated within zr-based metal-organic frameworks as efficient heterogeneous catalysts for olefins epoxidation, ACS Sustainable Chem. Eng. 7 (2019) 3624–3631, https://doi.org/10.1021/acssuschemeng.8b06736.

[143] N.V. Maksimchuk, K.A. Kovalenko, S.S. Arzumanov, Y.A. Chesalov, M.S. Melgunov, A.G. Stepanov, V.P. Fedin, O.A. Kholdeeva, Hybrid Polyoxotungstate/MIL-101 materials: synthesis, characterization, and catalysis of H₂O₂-based alkene epoxidation, Inorg. Chem. 49 (2010) 2920–2930, https://doi.org/10.1021/ic902459f.

[144] S. Wang, Y. Liu, Z. Zhang, X. Li, H. Tian, T. Yan, X. Zhang, S. Liu, X. Sun, L. Xu, F. Luo, S. Liu, One-step template-free fabrication of ultrathin mixed-valence polyoxovanadate-incorporated metal-organic framework nanosheets for highly efficient selective oxidation catalysis in air, ACS Appl. Mater. Interfaces. 11 (2019) 12786–12796, https://doi.org/10.1021/acsami.9b00908.

[145] D. Hu, X. Song, S. Wu, X. Yang, H. Zhang, X. Chang, M. Jia, Solvothermal synthesis of co-substituted phosphomolybdate acid encapsulated in the UiO-66 framework for catalytic application in olefin epoxidation, Chinese J. Catal. 42 (2021) 356–366, https://doi.org/10.1016/S1872-2067(20)63665-8.

[146] D. Dutta, A.D. Jana, M. Debnath, A. Bhaumik, J. Marek, M. Ali, Robust 1D open rack-like architecture in coordination polymers of Anderson POMs [{Na4(H2O) 14}{Cu(gly)}2][TeMo6O24] and [{Cu (en)2}3{TeW6O24}]: synthesis, characterization and heterogeneous catalytic epoxidation of olefins, Dalton Trans. 39 (2010) 11551–11559, https://doi.org/10.1039/C0DT00426J.

[147] X. Song, Y. Yan, Y. Wang, D. Hu, L. Xiao, J. Yu, W. Zhang, M. Jia, Hybrid compounds assembled from copper-triazole complexes and phosphomolybdic acid as advanced catalysts for the oxidation of olefins with oxygen, Dalton Trans. 46 (2017) 16655–16662, https://doi.org/10.1039/C7DT03198J.

[148] J. Du, X. Liu, J. Zhang, Y. Liu, E. Zhu, G. Che, M. Jia, Facile synthesis of a polycatenane compound based on ag-triazole complexes and phosphomolybdic acid for the catalytic epoxidation of olefins with molecular oxygen, Catalysts 9 (2019) 568, https://doi.org/10.3390/catal9070568.

[149] L.-N. Xiao, C.-X. Zhao, X.-M. Shi, H. Zhang, W. Wu, X.-B. Cui, Three new compounds based on similar molybdenum-vanadium clusters and several types of copper complexes, CrstEngComm 20 (2018) 969–977, https://doi.org/10.1039/C7CE01908D.

[150] Y.R. Wang, Q. Huang, C.-T. He, Y. Chen, J. Liu, F.-C. Shen, Y.-Q. Lan, Oriented electron transmission in polyoxometalate-metalloporphyrin organic framework for highly selective electroreduction of CO₂, Nat. Commun. 9 (2018) 4466, https://doi.org/10.1038/s41467-018-06938-z.

[151] W. Zheng, L.Y.S. Lee, Metal-organic frameworks for electrocatalysis: catalyst or precatalyst? ACS Energy Lett. 6 (2021) 2838–2843, https://doi.org/10.1021/acsenergylett.1c01350.

[152] P.-Q. Liao, J.-Q. Shen, J.-P. Zhang, Metal-organic frameworks for electrocatalysis, Coord. Chem. Rev. 373 (2018) 22–48, https://doi.org/10.1016/j.ccr.2017.09.001.

[153] Y. Xu, Q. Li, H. Xue, H. Pang, Metal-organic frameworks for direct electrochemical applications, Coor. Chem. Rev. 376 (2018) 292–318, https://doi.org/10.1016/j.ccr.2018.08.010.

[154] X. Li, Q.-L. Zhu, MOF-based materials for photo- and electrocatalytic CO₂ reduction, EnergyChem. 2 (2020) 100033, https://doi.org/10.1016/j.enchem.2020.100033.

[155] M.-L. Sun, Y.-R. Wang, W.-W. He, R.-L. Zhong, Q.-Z. Liu, S. Xu, J.-M. Xu, X.-L. Han, X. Ge, S.-L. Li, Y.-Q. Lan, A.M. Al-Enizi, A. Nafady, S. Ma, Efficient electron transfer from electron-sponge polyoxometalate to single-metal site metal-organic frameworks for highly selective electroreduction of carbon dioxide, Small 17 (2021) 2100762, https://doi.org/10.1002/smll.202100762.

[156] Q. Huang, Q. Niu, X.-F. Li, J. Liu, S.-N. Sun, L.-Z. Dong, S.-L. Li, Y.-P. Cai, Y.-Q. Lan, Demystifying the roles of single metal site and cluster in CO₂ reduction via light and electric dual-responsive polyoxometalate-based metal-organic frameworks, Sci. Adv. 8 (2022) eadd5598, https://doi.org/10.1126/sciadv.add5598.

[157] Z. Xin, Y.-R. Wang, Y. Chen, W.-L. Li, L.-Z. Dong, Y.-Q. Lan, Metallocene implanted metalloporphyrin organic framework for highly selective CO₂ electroreduction, Nano Energy 67 (2020) 104233, https://doi.org/10.1016/j.nanoen.2019.104233.

[158] N. Kornienko, Y. Zhao, C.S. Kiley, C. Zhu, D. Kim, S. Lin, C.J. Chang, O.M. Yaghi, P. Yang, Metal-organic frameworks for electrocatalytic reduction of carbon dioxide, J. Am. Chem. Soc. 137 (2015) 14129–14135, https://doi.org/10.1021/jacs.5b08212.

[159] H. Idan, D.S. Matthew, D. Pravas, P.K. Clifford, K.F. Omar, T.H. Joseph, Fe-porphyrin-based metal-organic framework films as high-surface concentration, heterogeneous catalysts for electrochemical reduction of CO₂, Acs Catal. 38 (2015) 6302–6309, https://doi.org/10.1021/acscatal.5b01767.

[160] D. Zhao, X.-H. Liu, Y. Zhao, P. Wang, Y. Liu, M. Azam, S.I. Al-Resayes, Y. Lu, W.-Y. Sun, Ionic exchange of metal-organic frameworks to access single nickel sites for efficient electroreduction of CO₂, J. Am. Chem. Soc. 139 (2017) 8078–8081, https://doi.org/10.1021/jacs.7b02736.

[161] R. Haldar, K. Batra, S.M. Marschner, A.B. Kuc, S. Zahn, R.A. Fischer, S. Braese, T. Heine, C. Woell, Bridging the green gap: metal-organic framework heteromultilayers assembled from porphyrinic linkers identified by using computational screening, Chem. Eur. J. 25 (2019) 7847–7851, https://doi.org/10.1002/chem.201901585.

[162] Y. Wang, P. Hou, Z. Wang, P. Kang, Zinc imidazolate metal-organic frameworks (ZIF-8) for electrochemical reduction of CO2 to CO, ChemPhysChem 18 (2017) 3142–3147, https://doi.org/10.1002/cphc.201700716.

[163] X. Jiang, H. Li, J. Xiao, D. Gao, R. Si, F. Yang, Y. Li, G. Wang, X. Bao, Carbon dioxide electroreduction over imidazolate ligands coordinated with zn (II) center in ZIFs, Nano Energy 52 (2018) 345–350, https://doi.org/10.1016/j.nanoen.2018.07.047.

[164] Q. Huang, Q. Li, J. Liu, Y.R. Wang, R. Wang, L.Z. Dong, Y.H. Xia, J.L. Wang, Y.-Q. Lan, Disclosing CO₂ activation mechanism by hydroxyl-induced crystalline structure transformation in electrocatalytic process, Matter. 1 (2019) 1656–1668, https://doi.org/10.1016/j.matt.2019.07.003.

[165] L. Ye, J. Liu, Y. Gao, C. Gong, M. Addicoat, T. Heine, C. Woell, L. Sun, Highly oriented MOF thin film-based electrocatalytic device for the reduction of CO₂ to CO exhibiting high faradaic efficiency, J. Mater. Chem. A. 4 (2016) 15320–15326, https://doi.org/10.1039/C6TA04801C.

[166] Y.T. Guntern, J.R. Pankhurst, J. Vávra, M. Mensi, V. Mantella, P. Schouwink, R. Buonsanti, Nanocrystal/metal-organic framework hybrids as electrocatalytic platforms for CO₂ conversion, Angew. Chem. Int. Ed. 58 (2019) 12632–12639, https://doi.org/10.1002/anie.201905172.

[167] R. Hinogami, S. Yotsuhashi, M. Deguchi, Y. Zenitani, H. Hashiba, Y. Yamada, Electrochemical reduction of carbon dioxide using a copper rubeanate metal-organic framework, Ecs Electrochem. Lett. 1 (2012) H17–H19, https://doi.org/10.1149/2.001204eel.

[168] X. Tan, C. Yu, C. Zhao, H. Huang, X. Yao, X. Han, W. Guo, S. Cui, H. Huang, J. Qiu, Restructuring of Cu₂O to Cu₂O@Cu-metal-organic frameworks for selective electrochemical reduction of CO₂, ACS Appl. Mater. Interfaces 11 (2019) 9904–9910, https://doi.org/10.1021/acsami.8b19111.

[169] C. Wang, C. Yan Zhu, M. Zhang, Y. Geng, Y.G. Li, Z.M. Su, An intriguing window opened by a metallic two-dimensional lindqvist-cobaltporphyrin organic framework as an electrochemical catalyst for the CO₂ reduction reaction, J. Mater. Chem. a. 8 (2020) 14807–14814, https://doi.org/10.1039/D0TA04993J.

[170] Q. Huang, J. Liu, L. Feng, Q. Wang, W. Guan, L.-Z. Dong, L. Zhang, L.-K. Yan, Y.-Q. Lan, H.-C. Zhou, Multielectron transportation of polyoxometalate-grafted metalloporphyrin coordination frameworks for selective CO₂-to-CH₄ photoconversion, Natl. Sci. Rev. 7 (2020) 53–63, https://doi.org/10.1093/nsr/nwz096.

[171] Z.-B. Fang, T.-T. Liu, J. Liu, S. Jin, X.-P. Wu, X.-Q. Gong, K. Wang, Q. Yin, T.-F. Liu, R. Cao, H.-C. Zhou, Boosting interfacial charge-transfer kinetics for efficient overall CO₂ photoreduction via rational design of coordination spheres on metal-organic frameworks, J. Am. Chem. Soc. 142 (2020) 12515–12523, https://doi.org/10.1021/jacs.0c05530.

[172] Y. Gao, L. Zhang, Y. Gu, W. Zhang, Y. Pan, W. Fang, J. Ma, Y.-Q. Lan, J. Bai, Formation of a mixed-valence Cu(i)/Cu(ii) metal-organic framework with the full light spectrum and high selectivity of CO2 photo reduction into CH4, Chem. Sci. 11 (2020) 10143–10148, https://doi.org/10.1039/D0SC03754K.

[173] E.-X. Chen, M. Qiu, Y.-F. Zhang, Y.-S. Zhu, L.-Y. Liu, Y.-Y. Sun, X. Bu, J. Zhang, Q. Lin, Acid and base resistant zirconium polyphenolate-metalloporphyrin scaffolds for efficient CO₂ photoreduction, Adv. Mater. 30 (2018) 1704388, https://doi.org/10.1002/adma.201704388.

[174] M. Wang, D. Wang, Z. Li, Self-assembly of CPO-27-Mg/TiO₂ nanocomposite with enhanced performance for photocatalytic CO2 reduction, Appl. Catal. Environ. 183 (2016) 47–52, https://doi.org/10.1016/j.apcatb.2015.10.037.

[175] L.-Y. Wu, Y.-F. Mu, X.-X. Guo, W. Zhang, Z.-M. Zhang, M. Zhang, T.-B. Lu, Encapsulating perovskite quantum dots in iron-based metal-organic frameworks (MOFs) for efficient photocatalytic CO2 reduction, Angew. Chem. Int. Ed. 58 (2019) 9491–9495, https://doi.org/10.1002/anie.201904537.

[176] R. Li, J. Hu, M. Deng, H. Wang, X. Wang, Y. Hu, H.-L. Jiang, J. Jiang, Q. Zhang, Y. Xie, Y. Xiong, Integration of an inorganic semiconductor with a metal-organic framework: a platform for enhanced gaseous photocatalytic reactions, Adv. Mater. 26 (2014) 4783–4788, https://doi.org/10.1002/adma.201400428.

[177] H. Zhang, J. Wei, J. Dong, G. Liu, L. Shi, P. An, G. Zhao, J. Kong, X. Wang, X. Meng, J. Zhang, J. Ye, Efficient visible-light-driven carbon dioxide reduction by a single-atom implanted metal-organic framework, Angew. Chem. Int. Ed. 55 (2016) 14310–14314, https://doi.org/10.1002/anie.201608597.

[178] D. Hagrman, P.J. Hagrman, J. Zubieta, Solid-state coordination chemistry: the self-assembly of microporous organic-inorganic hybrid frameworks constructed from tetrapyridylporphyrin and bimetallic oxide chains or oxide clusters, Angew. Chem. Int. Ed. 38 (1999) 3165–3168, https://doi.org/10.1002/(SICI)1521-3773(19991102)38:21<3165::AID-ANIE3165>3.0.CO;2-O.

[179] C. Zou, Z. Zhang, X. Xu, Q. Gong, J. Li, C.-D. Wu, A multifunctional organic-inorganic hybrid structure based on MnIII-porphyrin and polyoxometalate as a highly effective dye scavenger and heterogeneous catalyst, J. Am. Chem. Soc. 134 (2012) 87–90, https://doi.org/10.1021/ja209196t.

[180] M. Najafi, S. Abednatanzi, P. Gohari Derakhshandeh, F. Mollarasouli, S. Bahrani, E. Sadati Behbahani, Metal-organic and covalent organic frameworks for the remediation of aqueous dye solutions: adsorptive, catalytic and extractive processes, Coord. Chem. Rev. 454 (2022) 214332, https://doi.org/10.1016/j.ccr.2021.214332.

[181] J.-S. Qin, S.-R. Zhang, D.-Y. Du, P. Shen, S.-J. Bao, Y.-Q. Lan, Z.-M. Su, A microporous anionic metal-organic framework for sensing luminescence of

lanthanide (III) ions and selective absorption of dyes by ionic exchange, Chem. Eur. J. 20 (2014) 5625–5630, https://doi.org/10.1002/chem.201304480.

[182] J.-W. Sun, P.-F. Yan, G.-H. An, J.-Q. Sha, G.-M. Li, G.-Y. Yang, Immobilization of polyoxometalate in the metal-organic framework rht-MOF-1: towards a highly effective heterogeneous catalyst and dye scavenger, Sci. Rep. 6 (2016) 25595, https://doi.org/10.1038/srep25595.

[183] A.-X. Yan, S. Yao, Y.-G. Li, Z.-M. Zhang, Y. Lu, W.-L. Chen, E.-B. Wang, Incorporating polyoxometalates into a porous MOF greatly improves its selective adsorption of cationic dyes, Chem. Eur. J. 20 (2014) 6927–6933, https://doi.org/10.1002/chem.201400175.

[184] X. Liu, W. Gong, J. Luo, C. Zou, Y. Yang, S. Yang, Selective adsorption of cationic dyes from aqueous solution by polyoxometalate-based metal-organic framework composite, Appl. Surf. Sci. 362 (2016) 517–524, https://doi.org/10.1016/j.apsusc.2015.11.151.

[185] D. Li, X. Ma, Q. Wang, P. Ma, J. Niu, J. Wang, Copper-containing polyoxometalate-based metal-organic frameworks as highly efficient heterogeneous catalysts toward selective oxidation of alkylbenzenes, Inorg. Chem. 58 (2019) 15832–15840, https://doi.org/10.1021/acs.inorgchem.9b02189.

[186] Y. Wang, Z.-X. Liu, X.-P. Zhao, Y.-Y. Ma, S.-M. Zhang, W.-J. Cui, J. Du, Z.-G. Han, Polyoxometalate-encapsulated metal-organic frameworks with diverse cages for the C-H bond oxidation of alkylbenzenes, Chin. J. Chem. 42 (2023) 100011, https://doi.org/10.1016/j.cjsc.2023.100011.

[187] Q. Wang, B. Xu, Y. Wang, H. Wang, X. Hu, P. Ma, J. Niu, J. Wang, Polyoxometalate-incorporated framework as a heterogeneous catalyst for selective oxidation of C-H bonds of alkylbenzenes, Inorg. Chem. 60 (2021) 7753–7761, https://doi.org/10.1021/acs.inorgchem.1c00135.

[188] Y. Zheng, Q. Shen, Z. Li, X. Jing, C. Duan, Two copper-containing polyoxometalate-based metal-organic complexes as heterogeneous catalysts for the C-H bond oxidation of benzylic compounds and olefin epoxidation, Inorg. Chem. 61 (2022) 11156–11164, https://doi.org/10.1021/acs.inorgchem.2c01073.

[189] T.-Y. Dang, R.-H. Li, H.-R. Tian, W. Guan, Y. Lu, S.-X. Liu, Highly efficient multi-site synergistic catalysis of a polyoxovanadate-based metal-organic framework for benzylic C-H bond oxidation, J. Mater. Chem. A. 10 (2022) 16514–16523, https://doi.org/10.1039/D2TA03886B.

[190] F. Yu, X.-J. Kong, Y.-Y. Zheng, Y.-P. Ren, L.-S. Long, R.-B. Huang, pH-dependent assembly of 0D to 3D keggin-based coordination polymers: structures and catalytic properties, Dalton Trans. (2009) 9503–9509, https://doi.org/10.1039/B911606K.

[191] F. Yu, P.-Q. Zheng, Y.-X. Long, Y.-P. Ren, X.-J. Kong, L.-S. Long, Y.-Z. Yuan, R.-B. Huang, L.-S. Zheng, Polyoxometalate-based metal-organic frameworks as heterogeneous catalysts for selective oxidation of ethylbenzene, Eur. J. Inorg. Chem. 2010 (2010) 4526–4531, https://doi.org/10.1002/ejic.201000491.

[192] K. Yu, D.-I. Won, W.I. Lee, W.-S. Ahn, Porphyrinic zirconium metal-organic frameworks: synthesis and applications for adsorption/catalysis, Korean J. Chem. Eng. 38 (2021) 653–673, https://doi.org/10.1007/s11814-020-0730-z.

[193] G. Paille, M. Gomez-Mingot, C. Roch-Marchal, B. Lassalle-Kaiser, P. Mialane, M. Fontecave, C. Mellot-Draznieks, A. Dolbecq, A fully Noble metal-free photosystem based on cobalt-polyoxometalates immobilized in a porphyrinic metal-organic framework for water oxidation, J. Am. Chem. Soc. 140 (2018) 3613–3618, https://doi.org/10.1021/jacs.7b11788.

[194] G. Paille, M. Gomez-Mingot, C. Roch-Marchal, M. Haouas, Y. Benseghir, T. Pino, M.-H. Ha-Thi, G. Landrot, P. Mialane, M. Fontecave, A. Dolbecq, C. Mellot-Draznieks, Thin films of fully Noble metal-free POM@MOF for photocatalytic water oxidation, ACS Appl. Mater. Interfaces. 11 (2019) 47837–47845, https://doi.org/10.1021/acsami.9b13121.

[195] L. Che, Q. Xu, X. Liang, J. Wang, X. Su, Iron-based metal-organic frameworks as catalysts for visible light-driven water oxidation, Small 12 (2016) 1351–1358, https://doi.org/10.1002/smll.201503526.

[196] W.A. Shah, A. Waseem, M.A. Nadeem, P. Kögerler, Leaching-free encapsulation of cobalt-polyoxotungstates in MIL- 100(Fe) for highly reproducible photocatalytic water oxidation, Appl. Catal. 567 (2018) 132–138, https://doi.org/10.1016/j.apcata.2018.08.002.

[197] J. Han, D. Wang, Y.H. Du, S. Xi, Z. Chen, S. Yin, T. Zhou, R. Xu, Polyoxometalate immobilized in MIL-101(Cr) as an efficient catalyst for water oxidation, Appl. Catal. a. 521 (2016) 83–89, https://doi.org/10.1016/j.apcata.2015.10.015.

[198] Z. Huang, Z. Luo, Y.V. Geletii, O. Yin, J.W. Wickers, Q. Yin, D. Wu, Y. Hou, Y. Ding, J. Song, D.G. Musaev, C.L. Hill, T. Lian, Efficient light-driven carbon free cobalt-based molecular catalyst for water oxidation, J. Am. Chem. Soc. 133 (2011) 2068–2071, https://doi.org/10.1021/ja109681d.

[199] M. Duguet, A. Lemarchand, Y. Benseghir, P. Mialane, M. Gomez-Mingot, C. Roch-Marchal, M. Haouas, M. Fontecave, C. Mellot-Draznieks, C. Sassoye, A. Dolbecq, Structure-directing role of immobilized polyoxometalates in the synthesis of porphyrinic Zr-based metal–organic frameworks, Chem. Commun. 56 (2020) 10143–10146, https://doi.org/10.1039/D0CC04283H.

[200] A.J. Howarth, Y. Liu, P. Li, Z. Li, T.C. Wang, J.T. Hupp, O.K. Farha, Chemical, thermal and mechanical stabilities of metal-organic frameworks, Nat. Rev. Mater. 1 (2016) 15018, https://doi.org/10.1038/natrevmats.2015.18.

[201] S. Yuan, J.S. Qin, C.T. Lollar, H.C. Zhou, Stable metal-organic frameworks with group 4 metals: current status and trends, ACS Cent. Sci. 4 (2018) 440–450, https://doi.org/10.1021/acscentsci.8b00073.

[202] W.H. Ho, T.-Y. Chen, K.-I. Otake, Y.-C. Chen, Y.-S. Wang, J.-H. Li, H.-Y. Chen, C.-W. Kung, Polyoxometalate adsorbed in a metal-organic framework for electrocatalytic dopamine oxidation, Chem. Commun. 56 (2020) 11763–11766, https://doi.org/10.1039/D0CC04904B.

[203] W. Zhang, G. Jia, Z. Li, C. Yuan, Y. Bai, D. Fu, Selective electrochemical detection of dopamine on polyoxometalate-based metal-organic framework and its composite with reduced graphene oxide, Adv. Mater. Interfaces. 4 (2017) 1601241, https://doi.org/10.1002/admi.201601241.

[204] J. Li, J. Xia, F. Zhang, Z. Wang, Q. Liu, A novel electrochemical sensor based on copper-based metal-organic framework for the determination of dopamine, J. Chin. Chem. Soc. 65 (2018) 743–749, https://doi.org/10.1002/jccs.201700410.

[205] S. Chen, C. Wang, M. Zhang, W. Zhang, J. Qi, X. Sun, L. Wang, J. Li, N-doped Cu-MOFs for efficient electrochemical determination of dopamine and sulfanilamide, J. Hazard. Mater. 390 (2020) 122157, https://doi.org/10.1016/j.jhazmat.2020.122157.

[206] D.M. Fernandes, A.D. Barbosa, J. Pires, S.S. Balula, L. Cunha-Silva, C. Freire, Novel composite material Polyoxovanadate@MIL-101(Cr): a highly efficient electrocatalyst for ascorbic acid oxidation, ACS Appl. Mater. Inter. 5 (2013) 13382–13390, https://doi.org/10.1021/am4042564.

[207] S.S. Shetty, B. Moosa, L. Zhang, B. Alshankiti, W. Baslyman, V. Mani, N.M. Khashab, K.N. Salama, Polyoxometalate-cyclodextrin supramolecular entities for real-time in situ monitoring of dopamine released from neuroblastoma cells, Biosens. Bioelectron. 229 (2023) 115240, https://doi.org/10.1016/j.bios.2023.115240.

[208] S. Lu, M. Hummel, K. Chen, Y. Zhou, S. Kang, Z. Gu, Synthesis of AU@ZIF-8 nanocomposites for enhanced electrochemical detection of dopamine, Electrochem. Commun. 114 (2020) 106715, https://doi.org/10.1016/j.elecom.2020.106715.

[209] S. Karamzadeh, E. Sanchooli, A.R. Oveisi, S. Daliran, R. Luque, Visible-LED-light-driven photocatalytic synthesis of N-heterocycles mediated by a polyoxometalate-containing mesoporous zirconium metal-organic framework, Appl. Catal. B. 303 (2022) 120815, https://doi.org/10.1016/j.apcatb.2021.120815.

[210] V. Calvino-Casilda, R.M. Martín-Aranda, Ordered mesoporous molecular sieves as active catalysts for the synthesis of 1,4-dihydropyridine derivatives, Catal. Today 354 (2020) 44–50, https://doi.org/10.1016/j.cattod.2019.06.046.

[211] M. Nasr-Esfahani, S.J. Hoseini, M. Montazerozohori, R. Mehrabi, H. Nasrabadi, Magnetic Fe3O4 nanoparticles: efficient and recoverable nanocatalyst for the synthesis of polyhydroquinolines and Hantzsch 1,4-dihydropyridines under solvent-free conditions, J. Mol. Catal. A Chem. 382 (2014) 99–105, https://doi.org/10.1016/j.molcata.2013.11.010.

[212] R.H. Boecker, F.P. Guengerich, Oxidation of 4-aryl- and 4-alkyl-substituted 2,6-dimethyl-3,5-bis(alkoxycarbonyl)-1,4-dihydropyridines by human liver microsomes and immunochemical evidence for the involvement of a form of cytochrome P-450, J. Med. Chem. 29 (1986) 1596–1603, https://doi.org/10.1021/jm00159a007.

[213] F.P. Guengerich, W.R. Brian, M. Iwasaki, M.A. Sari, C. Baeaernhielm, P. Berntsson, Oxidation of dihydropyridine calcium channel blockers and analogs by human liver cytochrome P-450 IIIA4, J. Med. Chem. 34 (1991) 1838–1844, https://doi.org/10.1021/jm00110a012.

[214] M.C. Bagley, M.C. Lubinu, Microwave-assisted oxidative aromatization of hantzsch 1,4-dihydro-pyridines using manganese dioxide, Synthesis 2006 (2006) 1283–1288, https://doi.org/10.1055/s-2006-926407.

[215] J.R. Pfister, Rapid, high-yield oxidation of hantzsch-type 1,4-dihydropyridines with ceric ammonium nitrate, Synthesis 1990 (1990) 689–690, https://doi.org/10.1055/s-1990-26982.

[216] J.-J. Vanden Eynde, A. Mayence, A. Maquestiau, A novel application of the oxidizing properties of pyridinium chlorochromate: aromatization of hantzsch 1,4- dihydropyridines, Tetrahedron 48 (1992) 463–468, https://doi.org/10.1016/S0040-4020(01)89008-6.

[217] N. Nakamichi, Y. Kawashita, M. Hayashi, Oxidative aromatization of 1,3,5-trisubstituted pyrazolines and hantzsch 1,4-dihydropyridines by Pd/C in acetic acid, Org. Lett. 4 (2002) 3955–3957, https://doi.org/10.1021/ol0268135.

[218] P.P. Ghosh, P. Mukherjee, A.R. Das, Triton-X-100 catalyzed synthesis of 1,4-dihydropyridines and their aromatization to pyridines and a new one pot synthesis of pyridines using visible light in aqueous media, RSC Adv. 3 (2013) 8220–8226, https://doi.org/10.1016/j.tet.2005.12.056.

[219] H.T. Abdel-Mohsen, J. Conrad, U. Beifuss, Laccase-catalyzed oxidation of hantzsch 1,4-dihydropyridines to pyridines and a new one pot synthesis of pyridines, Green Chem. 14 (2012) 2686–2690, https://doi.org/10.1039/C2GC35950B.

[220] P. Prakash, E. Gravel, H. Li, F. Miserque, A. Habert, M. den Hertog, W.L. Ling, I.N. N. Namboothiri, E. Doris, Direct and co-catalytic oxidative aromatization of 1,4-dihydropyridines and related substrates using gold nanoparticles supported on carbon nanotubes, Catal. Sci. Technol. 6 (2016) 6476–6479, https://doi.org/10.1039/C6CY00453A.

[221] T. Toyao, N. Ueno, K. Miyahara, Y. Matsui, T.-H. Kim, Y. Horiuchi, H. Ikeda, M. Matsuoka, Visible-light, photoredox catalyzed, oxidative hydroxylation of arylboronic acids using a metal-organic framework containing tetrakis (carboxyphenyl)porphyrin groups, Chem. Commun. 51 (2015) 16103–16106, https://doi.org/10.1039/C5CC06163F.

[222] K. Epp, A.L. Semrau, M. Cokoja, R.A. Fischer, Dual site Lewis-acid metal-organic framework catalysts for CO2 fixation: counteracting effects of node connectivity, defects and linker metalation, ChemCatChem 10 (2018) 3506–3512, https://doi.org/10.1002/cctc.201800336.

[223] S. Oudi, A.R. Oveisi, S. Daliran, M. Khajeh, R. Luque, U. Sen, H. García, Straightforward synthesis of a porous chromium-based porphyrinic metal-organic framework for visible-light triggered selective aerobic oxidation of benzyl alcohol to benzaldehyde, Appl. Catal. A. 611 (2021) 117965, https://doi.org/10.1016/j.apcata.2020.117965.